ABSTRACT

Effect of Inlet Hole Geometry on Surface Film Cooling
Effectiveness from Compound Angle, Shaped Holes

Berkley W. Bonjonia, M.S.M.E.

Mentor: Lesley M. Wright, Ph.D.

The gas turbine engine operates at temperatures that far exceed the melting point of the metals from which they are made. Cooling air from the high pressure compressor must be used to cool these components in the hot sections of the turbine engines. Coolant must be used as effectively as possible in order to increase engine efficiency. The Pressure Sensitive Paint Technique (PSP) is used to evaluate the effects of both compound angles and advanced shapes on the film cooling effectiveness. Most current film cooling geometries are orientated streamwise, with the mainstream flow, and the addition of the compound angle has shown both positive and negative effects on cooling effectiveness. These changes are seen based on the type of inlet, cooling geometry, and expansion of the outlet geometry onto the surface.

Effect of Inlet Hole Geometry on Surface Film Cooling
Effectiveness from Compound Angle, Shaped Holes

by

Berkley William Bonjonia, B.S.

A Thesis

Approved by the Department of Mechanical Engineering

Kenneth W. Van Treuren, D.Phil.

Submitted to the Graduate Faculty of
Baylor University in Partial Fulfillment of the
Requirements for the Degree
of

Masters of Science of Mechanical Engineering

Approved by the Thesis Committee

Lesley M. Wright, Ph.D, Chairperson

Kenneth W. Van Treuren, D.Phil.

Carlos Manzanares, Ph.D.

Accepted by the Graduate School
May 2018

J. Larry Lyon, Ph.D., Dean

Page bearing signatures is kept on file in the Graduate School

TABLE OF CONTENTS

LIST OF FIGURES

LIST OF TABLES

NOMENCLATURE

A	Area
BR	Low Bypass ratio
CCD	Charged Coupled Device
C_c	Concentration of Oxygen in the Coolant
CFD	Computational Fluid Dynamics
C_f	Concentration of Oxygen in the Film
C_{rel}	Relative Concentration of Ammonia
C_∞	Concentration of Oxygen in the Mainstream
CMC	Carbon Matrix Composites
CYSA	Cylindrical Round, Simple Angle
D	Hole Diameter
D_h	Hydraulic Hole Diameter
DR	Density Ratio
EB-PVD	Electron Beam Physical Vapor Deposition
EDM	Electrical Discharge Machining
FDSA	Forward Diffused, Simple Angle
FOD	Foreign Object Debris
FS	Fanshape
h	Heat Transfer Coefficient
HSI	Hue, Saturation, Intensity

I	Momentum Flux Ratio
I_b	Intensity of the Black Images
I(P)	Intensity of the Calibration Plate is Total Pressure is Reduced
$I(P)_{ref}$	Intensity of the Reference Images
IR	Infrared Thermography
K	Thermal Conductivity
L	Internal Length of the Film Cooling Hole
LDCA	Laterally Diffused, Compound Angle
LDSA	Laterally Diffused, Simple Angle
LFS	Laidback Fanshape
M	Mass Flux Ratio or Blowing Ratio
M_a	Mach Number of the Crossflow at the Jet Exit
MA	Mild Adverse Pressure Gradient
MF	Mild Favorable Pressure Gradient
ONX	On Design Analysis Software of Gas Turbine Engines
OPR	Overall Pressure Ratio
p	Perimeter
P	Pitch
P_{ref}	Intensity of the Reference Pressure Images
$(Po_2)_{Air}$	Partial Pressure of Oxygen on the Surface in the Mainstream Flow
$(Po_2)_{mix}$	Partial Pressure of Oxygen on the Surface in the Coolant Flow
PIV	Partial Image Velocimetry
PSP	Pressure Sensitive Paint

Q_{Cal}	Relative Intensity From Precalibration
$\dot{Q}$	Heat Transfer Rate (Watts)
RGB	Red, Green, Blue
S	Thrust Specific Fuel Consumption
S_x	Streamwise Hole Spacing
S_y	Lateral Hole Spacing
S-PIV	Stereoscopic Partial Image Velocimetry
SF	Strong Favorable Pressure Gradient
*t*ime	Plate Thickness, Time
TBC	Thermal Barrier Coating
TIT	Turbine Inlet Temperature
TLC	Thermochromic Liquid Crystal
TSP	Temperature Sensitive Paint
T	Temperature of the Surface
$T_{ref.0}$	Temperature of the Reference
T_{aw}	Temperature of the Adiabatic Wall
$T_{Coolant}$	Temperature of the Coolant
T_{Film}	Temperature of the film
T_i	Initial Temperature
T_∞	Temperature of the Mainstream Flow
Tu	Mainstream Turbulence
T_W	Temperature of The Wall
U	Velocity of the coolant in the Streamwise Direction

U_c	Coolant Velocity
U_∞	Mainstream Velocity
V	Velocity of the coolant in the Vertical Direction
VMF	Very Mild Favorable Pressure Gradient
X	Streamwise Distance Along the Flat Plate
y	Lateral Spacing
Y	Vertical Spacing
Z	Lateral Hole Spacing
α	Bypass Ratio or Thermal Diffusivity
β	Compound Angle
ΔT	Change in Temperature
ε	Surface Emissivity
γ	Laidback Angle
η	Film Cooling Effectiveness
$\overline{\eta}$	Laterally Averaged Cooling Effectiveness
$\overline{\eta}$	Area Overall Averaged Film Cooling Effectiveness
θ	Hole Inclination Angle
π_c	Overall Compression Ratio
π_f	Fan Pressure Ratio
ρ_c	Coolant Density
ρ_∞	Mainstream Density
σ	Stefan-Boltzmann Constant

ACKNOWLEDGMENTS

The completion of this document has by no means been achieved by myself. I have been aided and supported by many different people and organizations in order to complete this thesis. It has taken 18 months and hundreds of hours to complete this complex task and generate a high quality product that reflects the need of film cooling and effects of the compound angle and advanced inlet on component cooling and engine performance.

Completing this thesis would not have been possible without the constant guidance and support of Dr. Lesley Wright. Together we remodeled the entire 107 lab and designed and built a new low speed wind tunnel with the help of Mr. Ashley Orr. We also tested a variety of film cooling geometries which have led to some interesting and surprising conclusions. Dr. Wright has helped me become a better student, person, engineer, and I will always be grateful to her for giving me the privilege to come to Baylor and earn this advanced engineering degree.

I want to thank my committee Dr. Kenneth Van Treuren and Dr. Carlos Manzanares for reading and critiquing my document. A thesis is a type of document that reflects the characteristics of the person writing it, and with their help, my thesis shows the attention to detail and quality of work that has been performed and defines this study. I would also like to give a specific thanks to Dr. Van Treuren and Dr. Wright for helping me to enter the world of turbine engineering and pursue a career path in this field.

I would like to thank Honeywell Aerospace Inc. for sponsoring this research and my education. Mr. Dan Crites and Dr. Malak Malak have provided valuable feedback on the research that has been conducted in this project and allowed me to further my interest and desire to enter the field of aerospace and mechanical engineering.

My parents have been a constant source of encouragement and support for me while I have been completing this Master's Degree. Not only did they encourage me return to school to pursue this degree, they have also been supportive of my upcoming career at Honeywell and relocation to Phoenix, Arizona, making this transition much less stressful and enjoyable!

Finally I would like to thank all of my fellow graduate students here at Baylor University. Over the past two years I have completed eight courses and an entire research project. The constant support and knowledge from my friends has keep me going through this journey. I would like to give special thanks to Kyle Vinton, Sara Seitz, Daniel Salinas, Austin Reed, Jamie McCarrell, and John-Mark Clemenson.

CHAPTER ONE

Introduction

Importance of Gas Turbine Engines

The gas turbine engine helps to drive the world's economy. With new technology being developed in many global markets, it is important that goods be delivered as quickly as possible. A gas turbine has applications in two main markets. These types of engines are excellent for transporting people or goods across a state line and around the globe. These engines can power all types of heavier than air aircraft. The gas turbine is chosen because it has the highest power to weight ratio of any combustion engine. These engines also generate electricity for the national power grid and help keep the lights on in many countries all over the world. Because gas turbines are extensively used, improvements that can be made in their efficiency and power output can positively affect the world. By becoming more fuel efficient, improvements to the gas turbine engine can reduce operating costs that can be passed all the way to the end consumer. In addition, consuming less fuel will also reduce total the total emissions produced by fossil fuels

Gas Turbine Operation Background

The gas turbine engine operates using the traditional Brayton cycle. In its most basic form, the gas turbine engine is a four-step process for energizing and moving air to create power. An example of this engine can be seen in Fig. 1.1, a Honeywell TFE731-50R Turbofan engine.

Figure 1.1: Honeywell TFE731-50R Courtesy of CD Aviation [1]

The gas turbine cycle operates in a very distinct sequence. The air enters in the engine at the inlet or diffuser, where it sees the first stage fan or compressor. This initial compression is part of the first stage of the Brayton cycle process. A basic diagram of this cycle can be seen in Fig. 1.2.

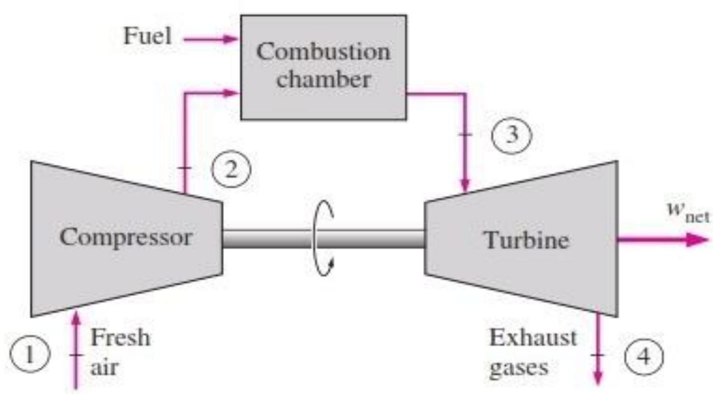

Figure 1.2: The Basic Brayton Cycle [2]

As the air moves through the compressor, the compressor rotors transfer mechanical energy to the air, and increase the internal energy of the air by raising the total pressure. The highest pressure in the engine is after the last stage of the compressor; in the largest commercial high bypass turbofans, air can leave the compressor with a pressure over 60 times higher than when it entered [3]. The high-pressure air now enters the combustor where fuel is added and burned; the air is now at its maximum temperature and total energy of the system. As the air leaves the combustor, it has been altered by the burning process and is now chemically altered air. This process changes the specific heat capacity of the air. Immediately after leaving the combustor, the air enters the turbine. This is the energy extraction phase of the process. The heated gas, which can reach temperatures of 1930°C, enters the turbine of the engine at temperatures which are significantly higher than what modern materials can withstand. Typically, the melting point of the best alloys used in turbine blades is approximately 1400°C, as seen by Bobzin et al. [4]. The temperature going into the turbine is directly controlled by the amount of fuel that is added to the combustor. Adding more fuel does increase the fuel consumption but it also leads to increases in the total efficiency by increasing the temperature in the turbine section of the engine. This means the increased power the engine produces justifies adding the extra fuel. Ideally, it is best to run the gas turbine with a turbine inlet temperature that is as high as possible; in this scenario the maximum amount of power can be extracted from the fuel that is being burned. It is certainly possible to run a gas turbine at temperatures below the melting point of the advanced materials of which they are constructed, but this would result in a reduction of both power and efficiency of the engine.

Cooling Overview and Effects

In the gas turbine engine a variety of factors are considered to improve the performance of the cycle; film cooling is one of the technologies that allows such high temperatures in the turbine. Getting these engines to become more fuel efficient and more powerful is largely a function of increased overall pressure ratio (OPR) in the compressor and an increased turbine inlet temperature (TIT) when extracting the energy. A higher turbine inlet temperature means more energy is available to be used as thrust after the required energy is extracted from the flow to drive the compressor. In order to advance turbine technology, carbon matrix composites (CMC) are under investigation in the gas turbine industry. Ohnabe et al. [5] shows how the use of CMC for turbine blades is becoming more popular. This technology offers lighter weight components with the ability to withstand the high temperatures of the turbine without film cooling. CMC technology has not yet been certified to withstand the temperatures and forces that designers want to impart on new engines. Therefore, turbine cooling is still a valuable and necessary part of any current engine design.

The high pressure TIT is increased through turbine blade cooling. This involves taking air from the high pressure compressor and directing it around the burner and into channels inside of the components in the turbine that are exposed to temperatures which would otherwise damage them. A representation of this is seen in Figures 1.3 and 1.4.

Figure 1.3 shows the location that cooling air comes from in the engine. Because the air coming from the last stage of the high pressure compressor is the highest pressure in the engine, this is the only place which has a high enough pressure to force the air through the cooling ducts in the turbine components. After the cooling air leaves the high pressure compressor, it bypasses the combustor and goes straight to the turbine through internal channels in the turbine blades and vanes, these channels are more clearly seen in Figure 1.4.

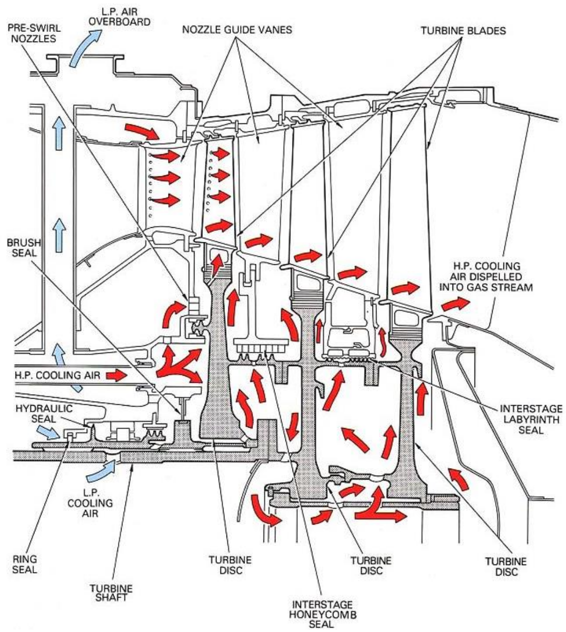

Figure: 1.3 Secondary Gas Path for Cooling Air [6]

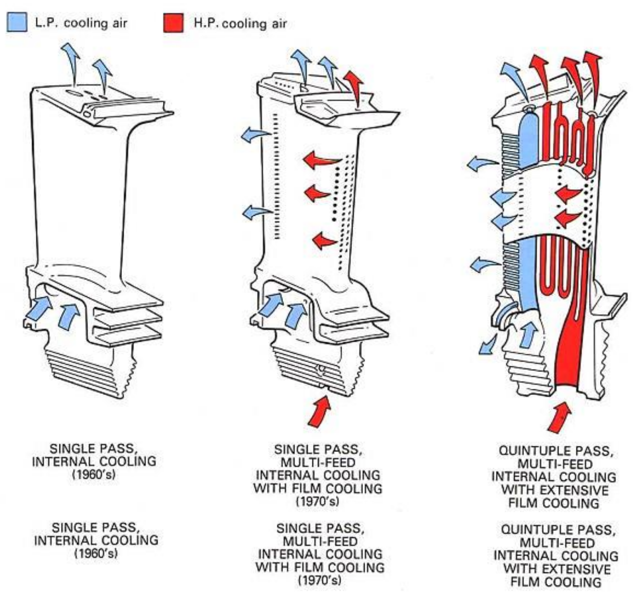

Figure 1.4: Detailed Cooling Paths through the Turbine Rotor Blades [7]

Turbine blade cooling originated with internal cooling and was the first method used to increase the TIT. Originally in the 1960's, single pass straight through internal cooling was used to cool the turbine blades, as shown by Xu et al. [8]. As cooling air was bled from the high pressure compressor, it was passed to the rotors and stators in the turbine. Simple straight channels from the root to the tip of the blade provided a path for the air through the blade, this would then convectively cool the blade from the inside and allow an increase in TIT. In Figure 1.5 TIT cooling progression can be seen.

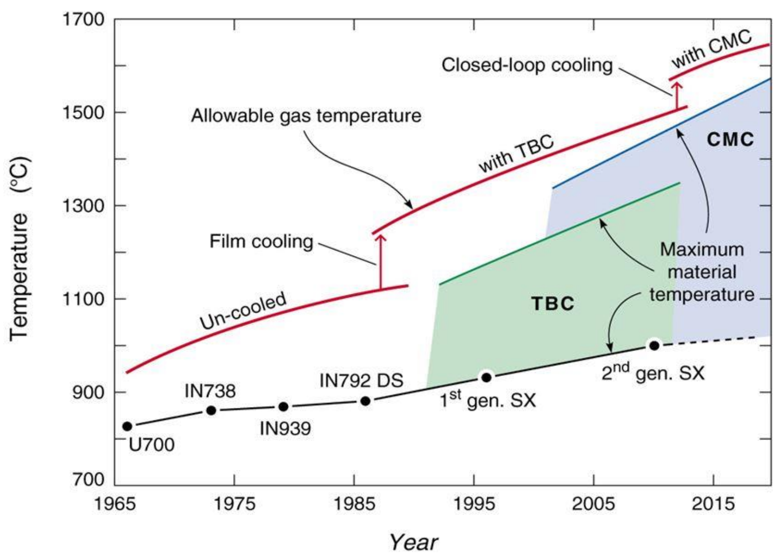

Figure 1.5: Increased Turbine Inlet Temperature with Progressive Cooling Technology [9]

From this simple straight channel, more advanced cooling methods and geometries have been introduced. Single pass cooling with oval shaped channels cast closer to the outer surface gave a slight enhancement in turbine cooling. In addition to these types of channels, jet impingement cooling was also introduced to the turbine blades. The leading edges of the rotors and stators see the highest temperatures; therefore, the most aggressive types of cooling are required in these areas. Rather than simply allowing cool air to pass through an area of high heat, jet impingement methods direct cool air directly on to the leading edge and then out of the tip of the blade.

In single pass cooling, the air is in contact with the blade for a limited amount of time. In order to prolong the time the cooling air is in contact with the turbine blade, multi-pass cooling was introduced. As seen in Figure 1.6, multi-pass cooling combined with the addition of ribs in the cooling channel, allows for much greater heat transfer inside the channels. This type of internal cooling is essentially the limit of what can be done internally to provide cooling in the turbine.

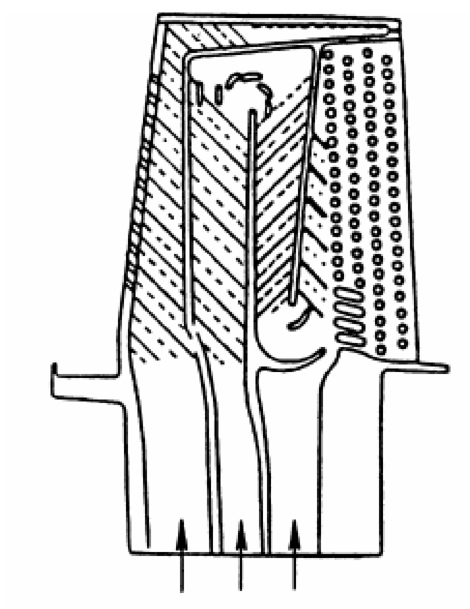

Figure 1.6 Multi-pass Internal Cooling with Rib Turbulators [10]

To further increase turbine cooling, exterior cooling methods must be used. This technique, also known as “film cooling,” requires taking air from the internal channels of the blade and venting it onto the surface of the blade. The technique is to create a layer of cooler gas between the hot mainstream gas and the physical turbine. This cooler layer helps to isolate and protect the blade from the extremely hot mainstream flow coming into the turbine. Film cooling started originally with round holes; these holes simply allowed portions of the cooling gas to be vented on the surface. This geometry is effective at cooling the blades but does have limitations. In early designs, a film hole was simply a passage from the interior of the blade to the exterior, and the coolant was not directed along the surface. Because the coolant mixes with the mainstream gas and lifts off the surface rapidly after reaching the surface, the round hole does not provide the most effective cooling. Advanced film cooling has now taken the place of the more traditional round hole in film cooling. Hole geometries such as the laidback fanshape, in Figure 1.7, are able to distribute cooling gas much more effectively.

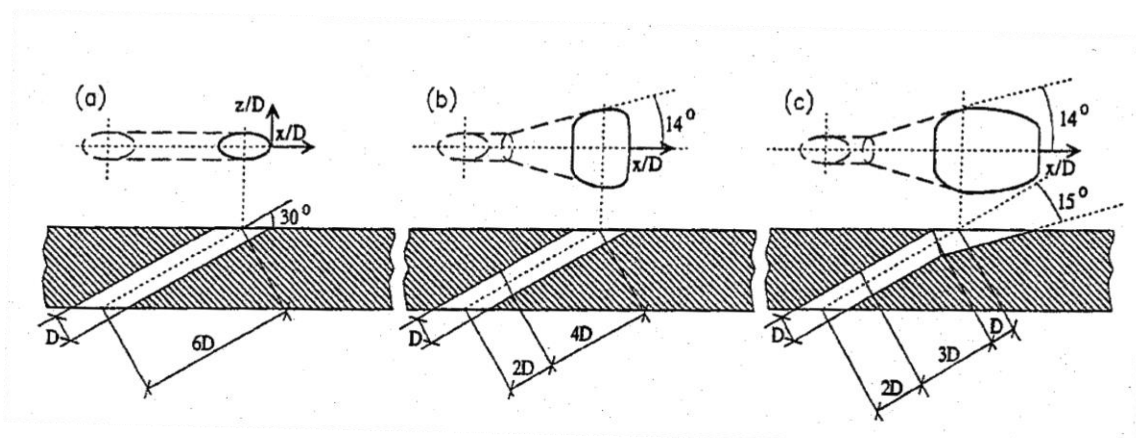

Figure 1.7: Laidback Fanshape Hole Goldstein et al. [11]

Fanshapes are able to reduce the speed of the mixing that occurs between the film and mainstream gas. Because of this, the ejected coolant is carried further down the surface of the turbine blade, and the blade is more effectively protected.

Engineers want to continually increase the TIT, one way this has been accomplished is by adding more coolant to the turbine components. However, this has led to a different concern in the engine. The turbine components have now become over cooled in order to increase the TIT and component lifespan. Bleeding cooling air from the compressor reduces the efficiency of the engine cycle, because the engine needs to compress the air, but then cannot extract as much work from it to help drive the cycle. This means as more cooling air is added, the power or thrust from the engine is reduced.

Film Cooling Effects on Cycle Performance

An understudied factor in engine design is how varying the levels of cooling in the engine actually affects the cycle performance of the jet engine. Cooling air mass flow percentage varies depending upon the company and is a guarded secret. To illustrate cooling, a brief study has been performed to illustrate these effects and show why it is important to effectively use film cooling in the turbine. It is important to clarify what is meant by "effectively film cool." This has two meanings in turbine blade design. The more obvious definition of "effective film cooling" is having a layer or "film" of cooling gas stay attached to the blade for a significant distance on the outside surface of the blade. This film creates a better cooling barrier between the blade and the hot mainstream air. The second definition of "effective cooling," is a film cooling geometry and blade design that can provide similar, or ideally increased film cooling, to previous designs, while at the same time, using a smaller percentage of cooling air from the compressor. These effects of the cooling percentage used are the focus of this study.

ONX is the cycle performance analysis software written by Jack D. Mattingly and is used for this analysis. This software allows for the custom input of the cycle type, as well as both component and polytropic performance efficiencies. The software also allows the changing of percent cooling air, bleed air, compression ratio, bypass ratio, and fan pressure ratio. Air mass flow through the engine will be set constant by the software and will be the same for every case examined in this study. Additionally, in this analysis, every case will have the same fan pressure ratio of $\pi_f = 2.4$. The fan pressure ratio has a substantial effect on the amount of power taken from the low-pressure turbine, and on the propulsive efficiency of the engine. High bypass engines create thrust by accelerating large qualities of air a small amount, creating the momentum change that generates thrust. Because of this, when this π_f ratio is altered, the amount of thrust produced and required power to drive the fan will change, altering the cycle's performance.

For the analysis a wide range of overall compression ratios (π_c) and bypass ratios (α) are considered. The data is considered for bypass ratios from α = 1.0, 2.0, 3.0, 5.0, and 7.0. The overall compression ratio is simulated for a π_c = 10 to 65 in increments of 5. The cooling air percentage will be studied in terms of percent of air mass flow taken from the exit of the high pressure compressor. This percentage is studied at percentages of 6, 10, 14, 20, and 25 percent. Information on percentage of cooling air used in a wide variety of engines is not readily available. In order to see trends in the effects of the cooling air, a wide range of percentages had to be considered. This study begins using six percent cooling air. Saravanamuttoo et al. [12] briefly studies cooling air effects, and it is suggested that for each stage in the high pressure, high temperature turbine, six percent of the air mass flow will be needed for cooling. The number of stages that need cooling will vary for each engine and depend on the application and TIT of that engine. The results of the study allow several conclusions to be made. For each combination of bypass ratio and overall compression ratio four types of data were calculated. The specific thrust, specific fuel consumption, thermal efficiency, and propulsive efficiency were all calculated and compared. Looking at the intuitive results first, Figure 1.8, shows that as the cooling air percentage increased, the specific thrust that the engine produces decreases. Specific thrust is compared because it is independent of the physical size of any engine.

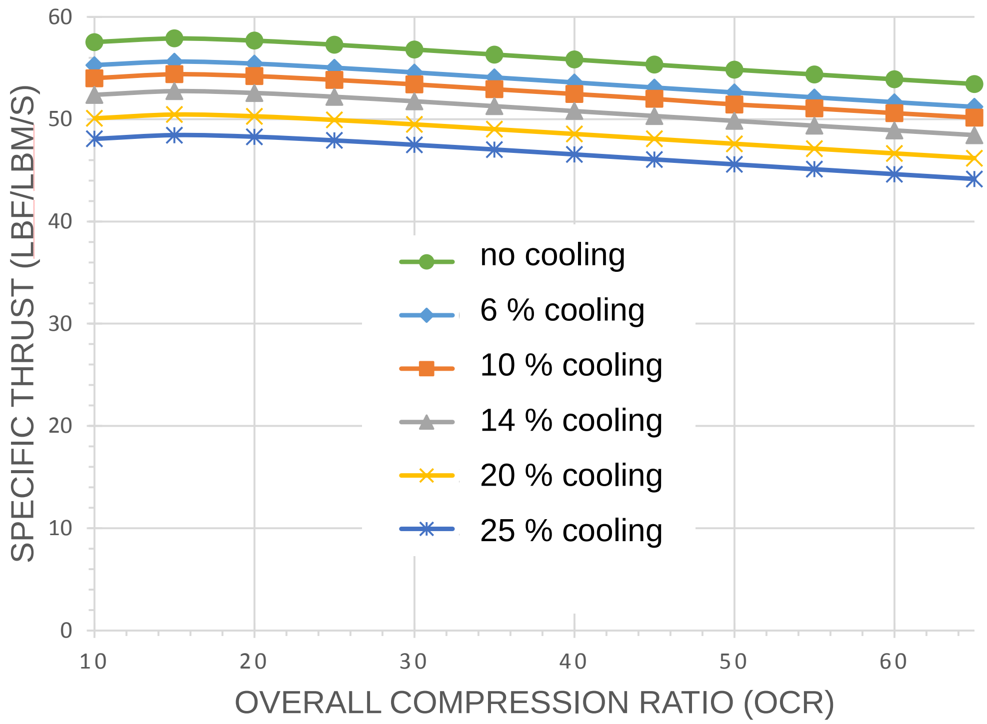

Figure 1.8: Effect of OCR and Cooling Flowrate on Engine Specific Thrust ($\alpha = 1.0$)

As shown in Figure 1.8, a plot of specific thrust versus π_c shows when cooling is used in the engine, the available specific thrust out of the core of the engine gradually decreases. In addition, as the compression ratio goes up, more work is needed to drive the system. This trend indicates if cooling air percentage increases, the overall size of the engine will also need to increase even with constant thrust requirements. This trend is the result of less energy being available in the mainstream gas. If cooling air is reduced, the available thrust will increase and the physical size of an engine will not need to increase to produce more power from the engine.

Figure 1.9 shows as film cooling in an engine increases, the thrust specific fuel consumption decreases. This plot also shows the advantage of going to a higher OCR for a given percentage of cooling air. As the overall compression ratio increases, the fuel consumption decreases even further. These results are expected; however, an exception to this is the increase in fuel consumption from 6% to 10% cooling. This increase is only seen for the bypass of one. This could be due to the cycle being near an optimum performance point under these conditions. This could also be an effect of altitude; these cycles were modeled at approximately 20,000 meters. However, in general, as the cooling air percentage increases more air is going around the burner. With this happening, less fuel needs to be added to raise the air going through the burner to the desired TIT. Unfortunately, this also comes at a cost, with less air available to burn fuel, less thrust is produced from the core of the engine. For engines that are running with a low bypass ratio, this is not a significant issue, as there is not a large fan in front of the core drawing large portions of mechanical energy produced in the cycle just to operate. In a low bypass ratio (BR) engine, the majority of the power comes from accelerating relatively smaller amounts of air. A large velocity change is required to see the significant momentum change of the air, this difference typically accelerates the air three times the velocity that into came in the engine. This velocity change is required to see the significant momentum change of the air and to produce the required thrust. These trends can be seen in Figure 1.10 and Figure 1.11.

When the BR is increased to 3.0, comparable trends to a BR of 1.0 are still seen. Just as in the specific fuel consumption for a BR of 1.0, Figure. 1.11 also shows a large change in performance. This change occurs as soon as cooling is added to the cycle. It is

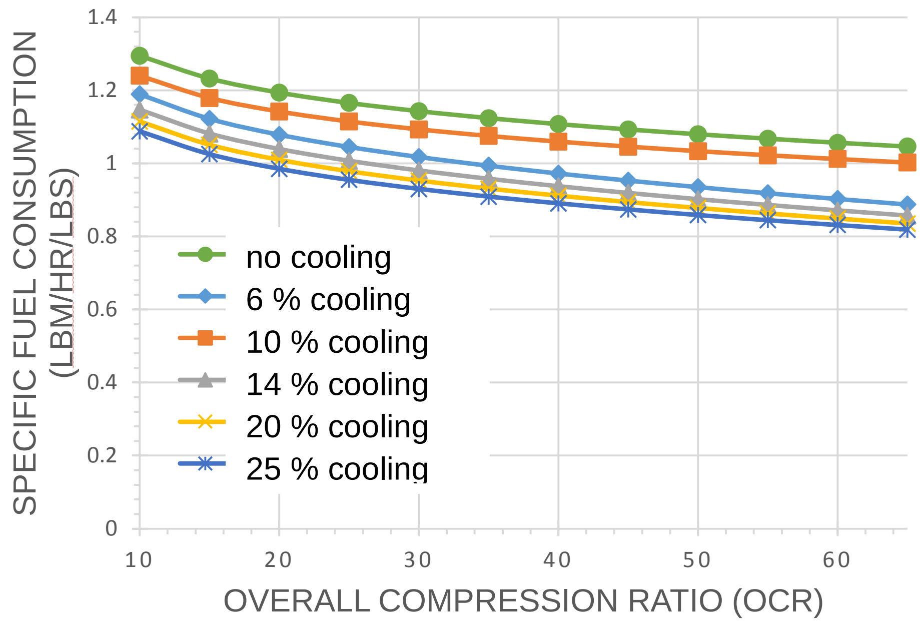

Figure 1.9: Effect of OCR and Cooling Flowrate on Engine Specific Fuel Consumption (α = 1.0)

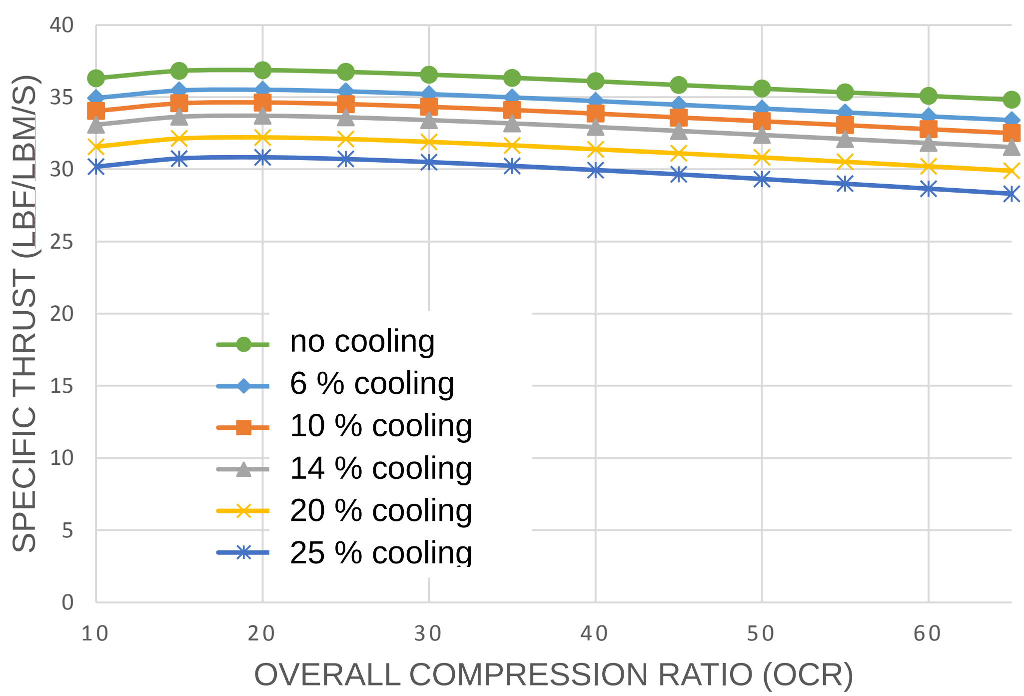

Figure 1.10: Effect of OCR and Cooling Flowrate on Engine Specific Thrust (α = 3.0)

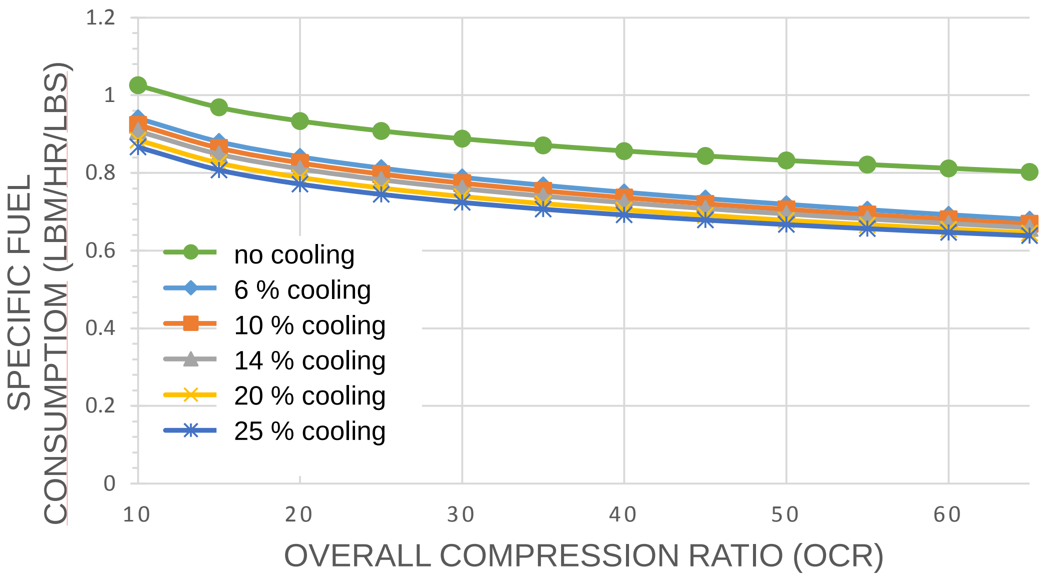

Figure 1.11: Effect of OCR and Cooling Flowrate on Engine Specific Fuel Consumption (α = 3.0)

important to remember that all the engines with cooling have smaller amounts of thrust being generated from the core versus if the engine did not have or need cooling, and a balance between the two must be achieved. Another important trend is as the amount of cooling is increased, the change in performance becomes progressively reduced each time. For the engine that has a BR of 1.0 and a varying cooling percentage of 6% to 25%, the theoretical specific thrust ranges from 43 to 54 $\frac{lbf}{\frac{lbm}{s}}$ at an OPR of 65, while the BR of 3.0 sees a specific thrust of 27 to 34 $\frac{lbf}{\frac{lbm}{s}}$ at the same OPR of 65. The performance improvements with a BR of 7.0 become less significant then were seen with lower bypass ratios. When the bypass ratio is increased further, the gradual decrease in specific thrust becomes an issue to the cycle being able to sustain itself. When the engine starts to reach into what is viewed as a "high" bypass, the configuration starts to become physically impossible. When looking at the BR of 7.0 not all of the cooling percentage cases are modeled. This is because as the cooling air was increased, the remaining energy in the flow after driving the compressor was not enough to drive the large fan in front of the core. These effects begin at the 14% cooling case that cannot exist at π_{c} = 55. Large percentages of cooling cannot be used for high bypass engines. This is seen clearly in Figure 1.12 and Figure 1.13 below.

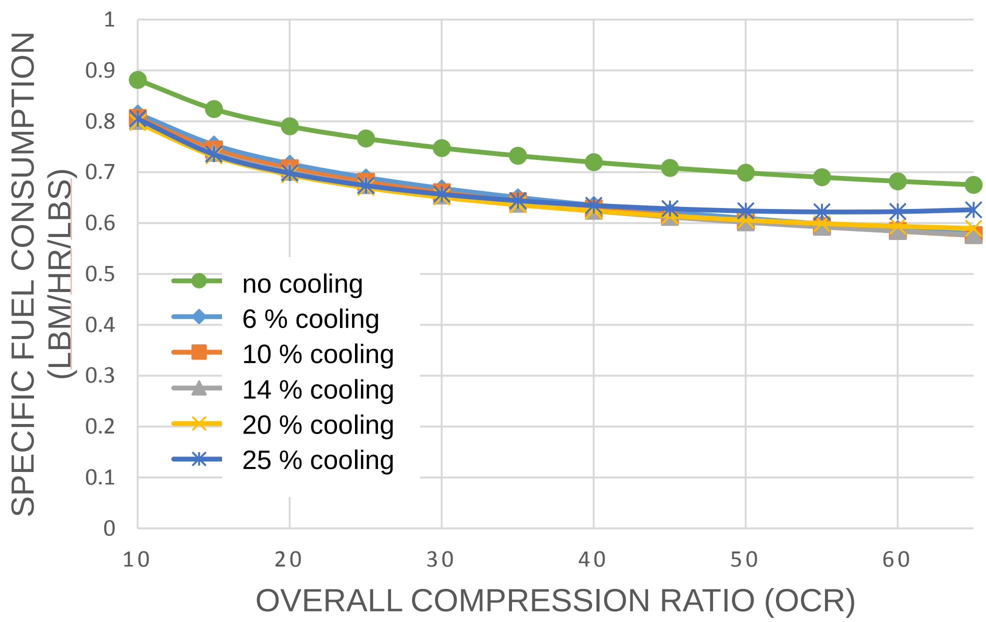

Figure 1.12: Effect of OCR and Cooling Flowrate on Engine Specific Fuel Consumption (α = 5.0)

As seen in Figure 1.12, the fuel savings for increasing cooling air percentage in a BR of 5.0 starts to become negligible, the trends show that all the cooling percentage gains are similar. Trends of a reduced thrust specific fuel consumption ‘S’ value do occur but the decrease in ‘S’ is reduced each time the cooling air percentage is increased; this occurs at the same time the amount of thrust coming from the engine is still decreasing. In Figure 1.13 the full effects of the increasing cooling air are seen. When the BR is increased to 7.0, as seen in current large commercial engines, the amount of air being used for cooling becomes critical to the cycle operation. In smaller bypass systems, the turbine always had enough power to drive the compressor and the fan, even with losses due to cooling air. With a BR of 7.0, simply not enough power is available to drive the system in the high cooling percentage cases. This is seen in Figure 1.13, as cycles with more than 14 percent of the air mass flow going to cooling, were not theoretically possible and could not be plotted. This lack of thrust can be seen more clearly in Figure 1.14; as the cooling air percentage increases, the specific thrust from the engine dramatically decreases. In future designs that have a high bypass ratio above 10, it will become even more critical that cooling air usage be reduced or ideally eliminated completely.

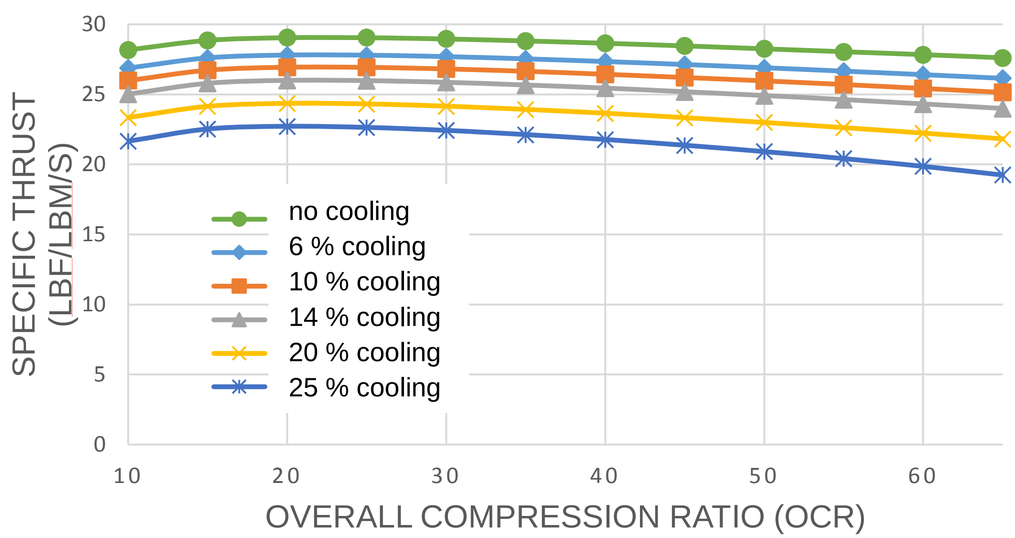

Figure 1.13: Effect of OCR and Cooling Flowrate on Engine Specific Thrust (α = 5.0)

Thermal and propulsive efficiency are directly related to the specific fuel consumption and specific thrust of an engine. Figure 1.15 shows that for a specific amount of cooling air, in this case six percent of the air mass flow, as the bypass ratio increases in the engine, thermal efficiency will decrease.

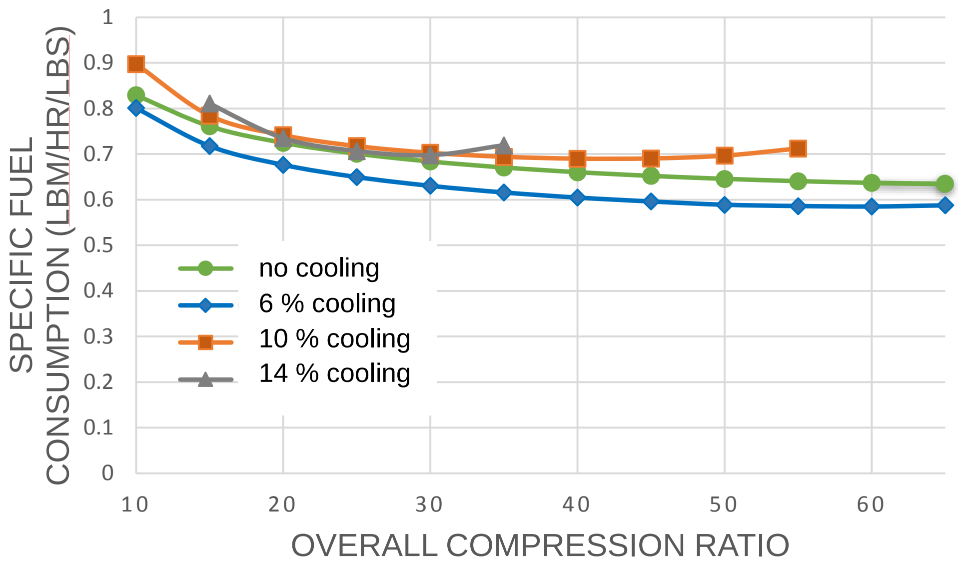

Figure 1.14: Effect of OCR and Cooling Flowrate on Engine Specific Fuel Consumption (α = 7.0)

This trend is expected; as the bypass ratio rises, it will require more energy to drive the system, this will leave less energy to be used for propulsion from the core. In Figure 1.16 propulsive efficiency is shown, the trends indicate that as the bypass ratio increases, the propulsive efficiency will also increase. Figure 1.16 shows further reason why large commercial airlines trend to using large bypass ratios. The bypass of 7.0 is almost twice as propulsively efficient as a bypass of 1.0. The case can and does exist, that thermal efficiency will be slightly sacrificed in order to gain in overall performance in the engine cycle. The optimal thermal efficiency and lowest thrust specific fuel consumption will likely occur at different OCR's. However, an engineer is more likely to choose an engine design that has the lowest specific fuel consumption, rather than choosing a design that has optimum thermal efficiency. Even a slight decrease in fuel consumption over the life of an engine is worth choosing a design that does not have the highest possible thermal efficiency. Looking at the efficiency with cooling percentage, it is seen why reducing cooling air is really a benefit to the engine cycle. Figure 1.17 and Figure 1.18, show the efficiencies with 14 percent of the total air mass flow going to cooling. These plots show that if new engine designs are able to keep cooling air at 14 percent or less, high bypass, high OCR engines are theoretically possible; this is the main concern in engine design. As the bypass ratio continues to increase, the level of cooling air will also have to increase.

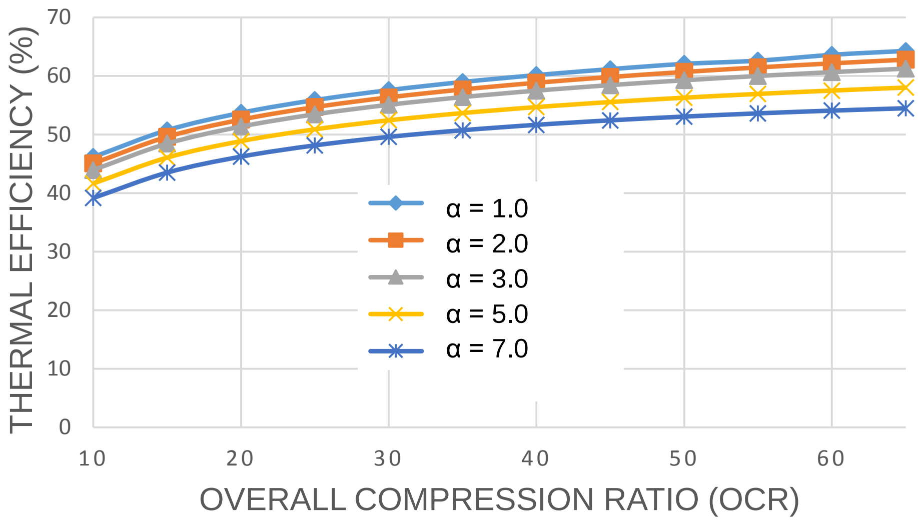

Figure 1.15: Thermal Efficiency at 6% Cooling Air

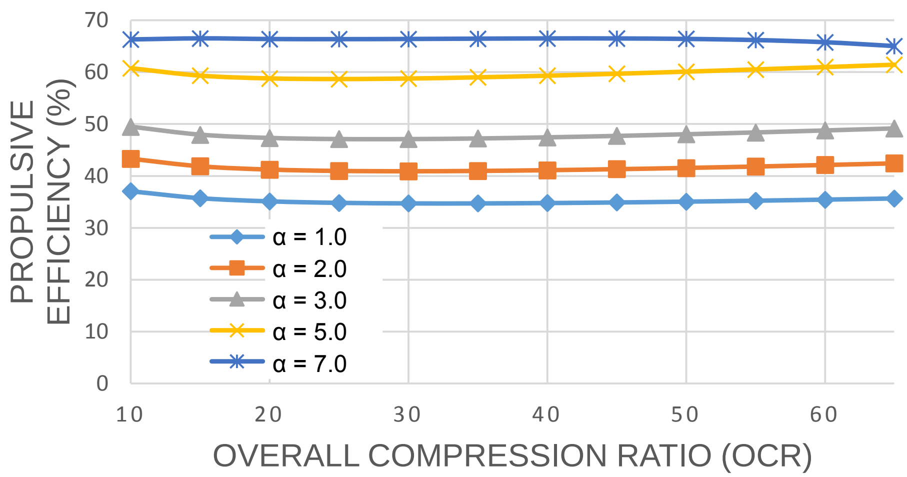

Figure 1.16: Propulsive Efficiency at 6% Cooling Air

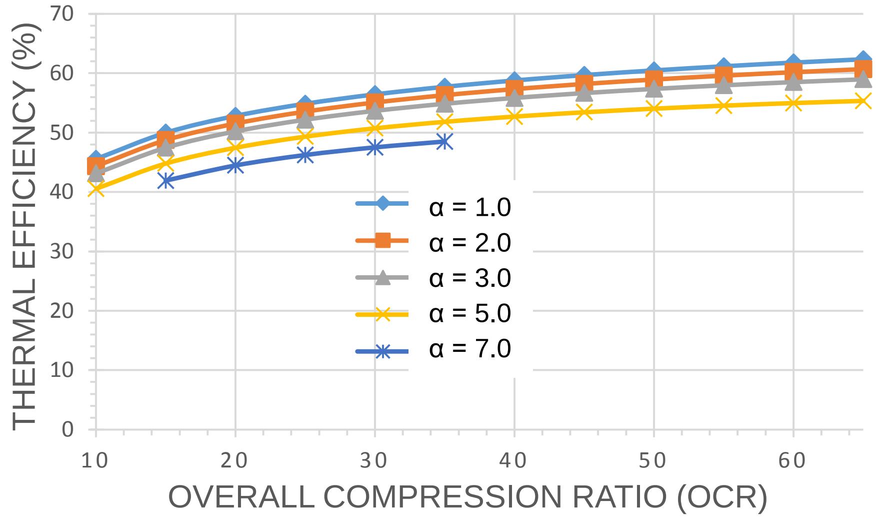

Figure 1.17: Thermal Efficiency at 14% Cooling Air

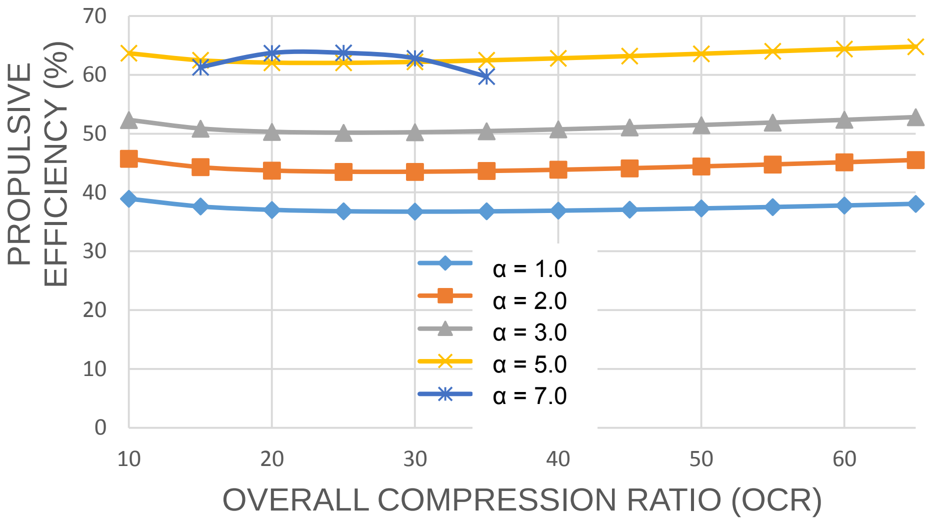

Figure 1.18: Propulsive Efficiency at 14% Cooling Air

As high bypass ratio engines start to reach a bypass of 8.0 to 10.0, the cooling air will need to be used for thrust and power production in the turbine. The main goal of this study was to show that increasing the amounts of cooling air that engines use from the high-pressure compressor will negatively affect the performance of any gas turbine engine. Using cooling air reduces the amount of air available for thrust and forces designers to build physically larger engines than would be necessary if cooling air was not as essential. This, however, comes at the cost of reducing specific thrust from engine and reducing overall efficiency. The alternative is to create engines which do not have larger outer diameters, but increased bypass ratios. These engines are more fuel efficient, but also produce less thrust. These newer types of engines and the trends they have set, can be used when the market demands a new large high thrust engine.

All of the testing done in the ONX study had a constant turbine inlet temperature of 1760°C. The final comparison of this study examines the effects when only the turbine inlet temperature is altered. The cooling percentage will be set at 10 percent, the bypass ratio is set at 3.0, and OCR is set to 30. The inlet temperatures will be tested over the range 1760-2200°C. Figures 1.19 and 1.20 show when the inlet temperature is increased, the specific thrust will also increase. Additionally, the fuel consumption has also increased.

These results show why improving film cooling effectiveness is so important. If designers can increase the turbine inlet temperature, more power can be extracted from the air mass flow through the engine. The fuel consumption will increase when the turbine temperature is increased because it will take more fuel to raise the air to the desired TIT. Designers still want to achieve higher temperatures, so engineers can use physically smaller engines, which can still provide comparable amounts of thrust or power. Additionally, for fighter jet engines, a more powerful engine that has not grown in physical size will be advantageous in increasing aircraft fighting performance. When comparing thrust specific fuel consumption and specific thrust, the size differences of the engines is no longer a factor, and designers look at and compare the true normalized performance of different engines. The significance of the difference in specific

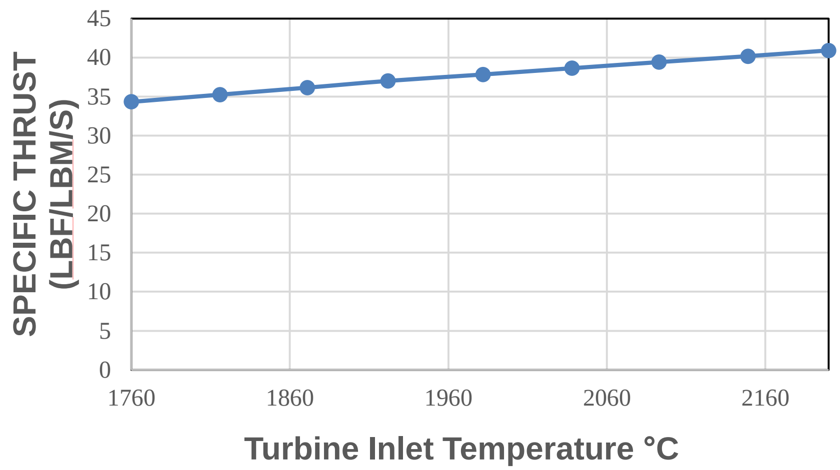

Figure 1.19: Specific Thrust with TIT from 1760 to 2200°C

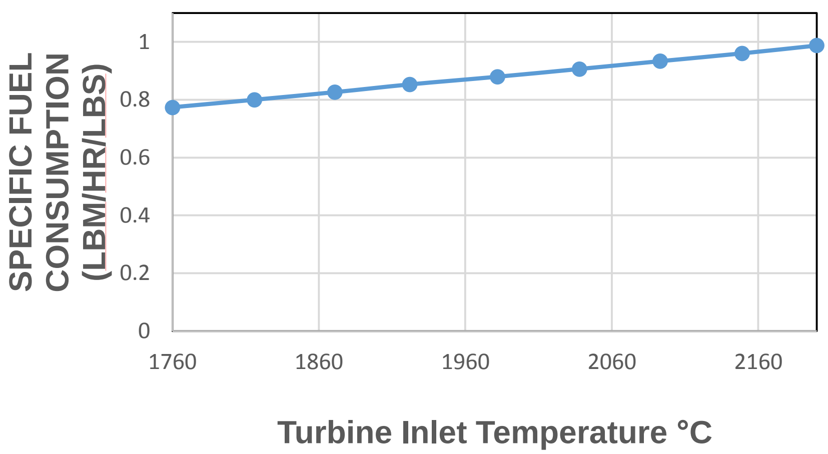

Figure 1.20: Specific Fuel Consumption with TIT from 1760 to 2200°C

thrust is important to the engine designers. If an engine can use little or no cooling air, the entire physical engine could be smaller. This means both a reduction in weight and production cost for each engine.

In order to facilitate the introduction of new larger, high bypass engines, the air that is used to cool the high temperature, high pressure sections of the engine will need to be reduced and the existing cooling air will need to be used as efficiently as possible. This means that new more efficient hole geometries for distributive film cooling need to be tested and proven. In conjunction, new coatings and materials for high temperature applications, like ceramic matrix composites, need to be perfected. These technologies can help reduce or eliminate the need for cooling air in the high temperature turbine section of the gas turbine engine. Achieving this goal becomes even more important as the OCR is pushed higher even exceeding seventy in new engine designs. When the pressure ratio is increased in the engine, more work must be done on the air, which will result in the increased temperature on the air as it leaves the compressor. This means that the cooling air meant for film cooling will also be at a higher temperature. This will reduce the difference in temperature between the coolant and the mainstream, but it also means that the temperature of the blade will increase even with effective cooling measures. The easiest way to reduce these effects is to reduce the usage of cooling air in the engine.

Study Objectives

Improving film cooling will allow engine designers to also more efficiently cool turbine engines. This means using less cooling air from the compressor which has been previously shown to decrease the performance of the engine and increase fuel consumption. The ultimate goal of this study, and most research on turbine engines, is to improve several key performance areas. Engines are designed to continually decrease fuel consumption, which will then lead to reduced flight cost and environmental impact. Designers want to also keep increasing the TIT, or reduce cooling air, which will mean the engine can run more efficiently and produce more thrust. The temperature increase in the turbine must be balanced by the longevity and reliability of the engine and its sensitive components. Improving film cooling will allow the temperatures in the turbine to be safely increased. By studying advanced shapes and different orientations for cooling geometries, the ultimate goal of this study is to increase cooling efficiency and effectiveness in the turbine, or hot section, of the engine.

CHAPTER TWO

Film Cooling Review

Flow Condition Effects on Cooling Effectiveness

The turbine inlet temperature, which affects the performance of a gas turbine engine, has been outlined in the previous chapter. The turbine inlet temperature also has an effect on the required level of cooling of the components in the turbine section of the engine. As the mainstream gas temperature increases beyond the melting temperature of the turbine blades, internal and external cooling is used to insulate and cool the turbine blades and other components. The effectiveness of external, film cooling is dependent on several factors. The mass flux ratio (M), momentum flux ratio (*I*), hole geometry, density ratio (DR), and mainstream turbulence (*Tu*) are shown by Oates [13] to significantly alter the film cooling effectiveness. The film cooling effectiveness, η, is the parameter used to define how well a film cooling geometry is protecting a turbine blade from the mainstream flow. In addition to these, hole inclination angle, θ, and surface curvature are also important factors for film cooling effectiveness. Han et al. [14] has outlined the effect each of these components has on film cooling jets.

To further understand how the previously mentioned factors will effect the film cooling effectiveness, a round hole geometry will be examined. A previous study by Bell et al. [15], examined the film cooling performance of a round hole at an inclination angle of $\theta = 35°$, oriented in the streamwise direction, and at a density ratio of DR = 1.0. When comparing the laterally averaged cooling effectiveness, against an increasing blowing ratio, a gradual decrease in the effectiveness was observed. The blowing ratio (M), is defined as the ratio of the coolant mass flow to that of the mainstream, as seen in Equation 2.1.

$$M = \frac{U_C \rho_C}{U_\infty \rho_\infty} \tag{2.1}$$

For a simple round hole at higher blowing ratios, the coolant lifts off the surface of the blade. When the cooling jet "lifts off" the surface, the effectiveness is reduced. After the jet lifts off there is flow reattachment to the surface, and this reattachment is unable to provide an equivalent amount of coverage as before the flow detached from the surface Han et al [14]. The increase and decrease of cooling effectiveness only covers half of the effects that are present at the surface. As the flow detaches from the surface, vortices form between the jet and the surface. This vorticity pulls mainstream air to the surface, which decreases the cooling effectiveness and increases the heat transfer coefficient for that region. When the heat transfer coefficient is increased, the blade temperature will increase and potentially cause part failure. The film cooling techniques are meant to isolate the surface from the mainstream, protect it from the extreme temperatures, and minimize an increases of the heat transfer coefficient. With round holes at higher blowing ratios of M > 0.8, the opposite effect is occurring: the cooling gas is wasted and blown off the surface, while cooling effectiveness is also reduced.

Pederson et al. [16] showed that the film cooling effectiveness was largely dependent on the density ratio between the coolant flow and the mainstream gas. In addition to the cooling effectiveness, the heat transfer coefficient is also greatly affected by the density ratio, as shown by Ammari et al. [17]. The density ratio is defined as the density of the cooling gas to the density of the mainstream flow as seen in Equation 2.2.

In a gas turbine engine, operating conditions can see density ratios range between DR = 2.0 to 4.0. Because of the difference in temperatures between the cooling air from the compressor and the core air traveling through the turbine, a significant difference in fluid density exists. It is important to test cooling geometries with these varying density ratios in order to better understand the cooling effects at more realistic operating conditions.

$$DR = \frac{\rho_C}{\rho_\infty} \tag{2.2}$$

To investigate this effect, Johnson et al. [18] used the PSP and PIV techniques to investigate the effects of different density ratios on film cooling. Using round holes at an inclination angle of θ = 30°, the density ratio was varied from DR = 1.0 to 1.53 with the blowing ratio from M = 0.85 to 1.7. Seen below in Figure 2.1, a sample of the results shows how a small difference in density ratio can make a large difference in flow velocity and surface flow attachment.

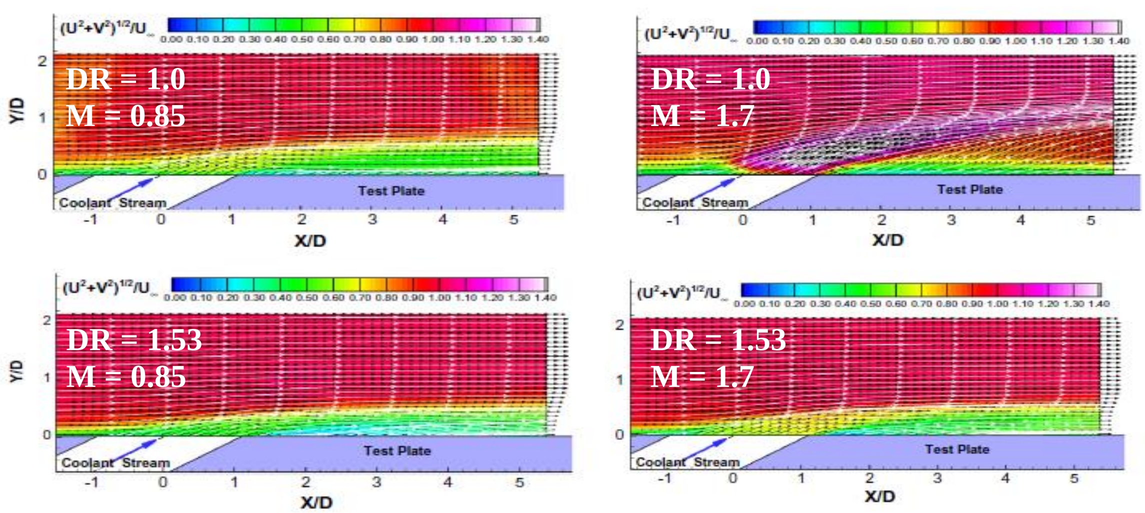

Figure 2.1: A Direct Comparison of the Coolant Velocity at a Blowing Ratio of M = 0.85 and 1.7 with a Density Ratio of DR = 1.00 and 1.53 (Johnson et al. [18])

This increase in density ratio has enhanced the flow attachment to the surface and improved film cooling characteristics. A second result shows that at lower blowing ratios, the flow will stay attached regardless of the density ratio and that the change in density ratio has a less significant effect. For lower blowing ratios the coolant flow has less momentum, and only has minimal detachment from the plate. This is the case whether the density ratio is 1.0 or even 4.0. As the blowing ratio is increased, the flow has more velocity and momentum, which means lift-off is more likely. However, while operating at a high density and high blowing ratio, the flow will still remains attached to the surface. The more dense coolant will remain close to the surface and be more resistant to mainstream mixing. At high density ratios, the vortices that form when the jet detaches from the plate also are diminished, thus coolant to mainstream mixing near the film cooling injection site can be even further reduced. Additional studies by Eberly and Thole [19] and Sinha et al. [20] have shown similar results to those of Johnson et al. [18].

Freestream turbulence also is shown to have an addition effect on jet separation and film cooling effectiveness. Wright et al. [21] showed that at high blowing ratios ($M \geq 1.0$) the surface cooling effectiveness was not greatly affected by freestream turbulence; at these high blowing ratios the jet had lifted of the surface and already had a diminished cooling effectiveness. In the cases with higher freestream turbulence the horseshoe and counter rotating vortices seen in Figure 2.2 that form around and in the jet are strengthened. These secondary flows cause decreased cooling effectiveness downstream of the film cooling hole.

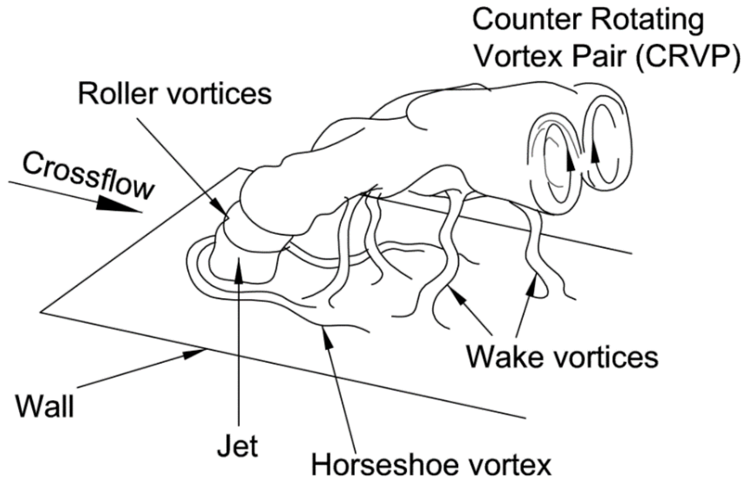

Figure 2.2: A Representation of the Three Vortices That are Generated by a Round Hole in Crossflow (Sarkar and Babu [22])

The previous results are supported by a study by Bons et al. [23] who studied round holes at an inclination of $\theta = 35°$. Two blowing ratios of M = 0.75 and 1.2 were used to show the different effects. These results are seen in Figure 2.3. This study covered a freestream turbulence percentage at *Tu* = 0.9, 6.5, 11.5, and 17.

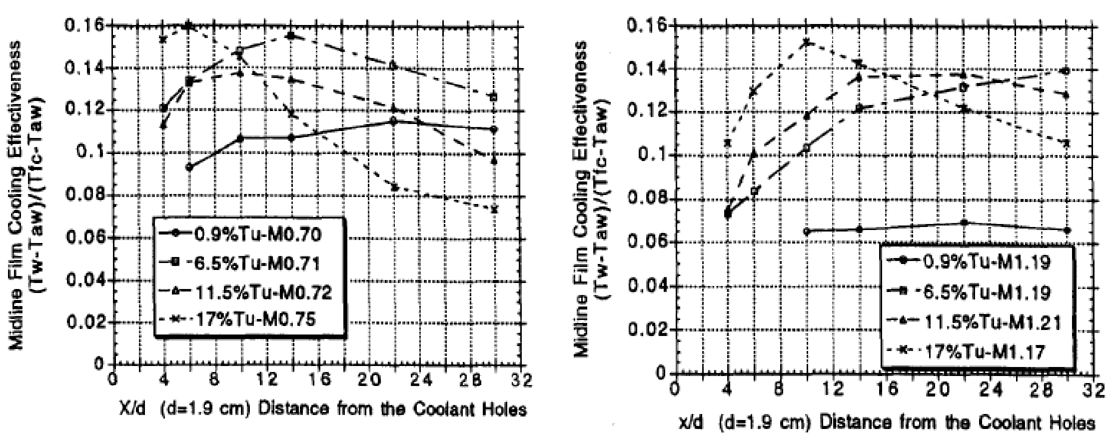

Figure 2.3: Cooling Effectiveness vs. X/D With Varying Freestream Turbulence Intensity at a M = 0.75 and M = 1.2 (Bons et al. [23])

When the mainstream turbulence is increased at a constant blowing ratio, cooling effectiveness is decreased at higher blowing ratios. As the jet detaches from the surface, the increased turbulence causes more eddies and more mixing of the cooling flow with the mainstream flow. These effects combine to bring more mainstream gas to the surface and reduce the cooling effectiveness. Saumweber et al. [24] conducted tests with round holes at an inclination angle of θ = 35° and freestream turbulence ranging from $Tu = 3.6\%$ to 11%. The results similarly show that freestream turbulence does have a significant effect on cooling effectiveness at low blowing ratios below M = 1.0. They also found at higher blowing ratios when the jet begins to lift off of the surface the local cooling effectiveness can be reduced up to 40%. A similar study by Mayhew et al. [25] used transient liquid crystal (TLC) and round cooling holes at an inclination angle of $\theta = 30°$. Once again, the blowing ratios at medium to high blowing ratios (M ≥ 1.0) were found to be affected by the increasing freestream turbulence. A separate parameter called the momentum flux ratio (I), is a representation of the blowing and density ratios and is seen in Equation 2.3.

$$I = \frac{\rho_C U_C^2}{\rho_\infty U_\infty^2} \tag{2.3}$$

Because the momentum flux ratio is derived from the density and blowing ratios it is also affected by the same flow characteristics. Starting from zero cooling flow, the momentum initially begins to increase, but it does not have enough inertia to push past the mainstream flow. As the momentum flux is increased, the coolant can then begin to enter the boundary layer and protect the surface. Film cooling blows air onto the surface of the blade, while also disturbing the boundary layer. This leads to boundary layer mixing and an increase in the heat transfer coefficient. Increasing heat transfer to the turbine blade is contrary to the idea of cooling and protecting the blades; however, because film cooling isolates the turbine blade from the mainstream flow, the gains in cooling more than offset the increased heat transfer coefficient.

As the momentum flux ratio increases, the results are similar to when the blowing ratio was increased. The cooling effectiveness reaches a maximum point at lower momentum ratios and begins to decline; when the momentum flux continues to increase, the flow begins detaching from the surface. The higher momentum carries the coolant off the surface, which then begins to form vortices that mix mainstream gas with the coolant flow reducing cooling effectiveness. These effects are again seen clearly in Figure 2.4. As the density ratio is increased the coolant then begins to stay attached, even at higher blowing ratios.

The three plots in Figure 2.4 are at an X/D = 6, 10, and 22. At X/D of 6.0, the three tested density ratios show minimal variation; however, at locations further downstream from the injection site, the higher density ratios start to provide significantly enhanced cooling. These higher densities negate the effects of increasing the momentum flux ratio and keep the flow attached to the surface for much longer. As the density ratio is increased, the same shape of the curves is on all three plots. In extreme cooling cases, in the regions that do not have large curvatures, multi-row effusion cooling is used to protect turbine blades. Effusion cooling involves using several rows of film cooling holes to completely cover a surface and can be seen in Figure 2.5. This type of cooling is used when the mainstream flow is at an extremely high Reynolds number, is too hot, and is flowing at an extremely high turbulence. A study conducted by Wang et al. [26] involved using round holes at an incidence angle of $\theta = 20°$, with varying blowing ratios used to identify the optimal operating conditions for effusion cooling. A density ratio of

DR = 1.5 was used to more effectively keep the flow attached to the surface. It was found that a blowing ratio of M = 0.8 showed the highest cooling effectiveness as seen in Figure 2.6.

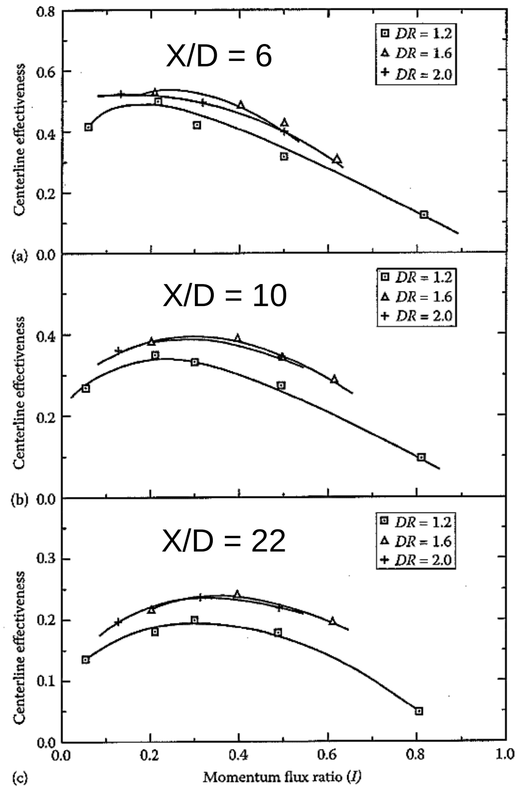

Figure 2.4: Centerline Cooling Effectiveness versus Momentum Flux Ratio (Han et al. [14])

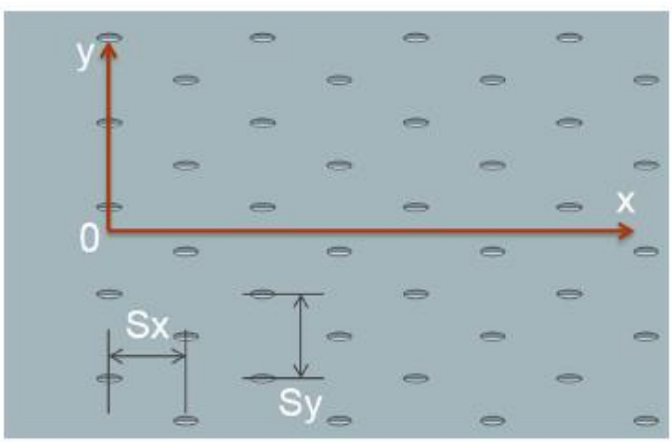

Figure 2.5: Effusion Cooling Hole Pattern (Wang et al. [26])

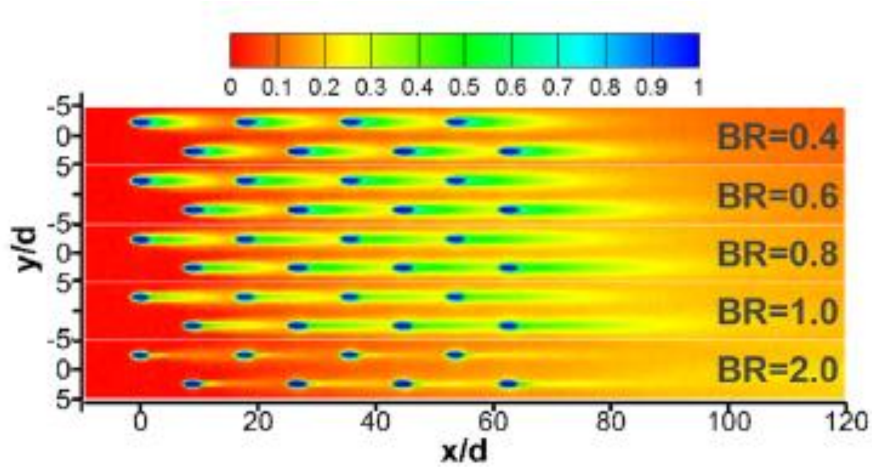

Figure 2.6: Effusion Cooling Results (Wang et al. [26])

In order to protect the blades as effectively as possible it is important to understand all of the effects occurring in the turbine section of the engine. Turbine blades work under the same aerodynamic principles as the wings of an aircraft: there is a pressure side and a suction side of each blade. It is important to realize film cooling will react differently to the pressure on either side of the blade; it then becomes important to understand and characterize these effects. These effects were seen by Teekaram et al. [27] while examining four different pressure gradient scenarios seen in Figure 2.7. The results showed that with a favorable pressure gradient, the cooling effectiveness would actually increase over a surface, while the opposite effect is seen on the adverse or pressure side of the blade.

Compound Angle Effects on Film Cooling

All the previously studied cases have one common attribute, namely the film cooling holes are in-line with the mainstream flow and directing the coolant streamwise with the mainstream. To further increasing cooling effectiveness a second compound angle ‘β’ can be added to the cooling holes as seen in Figure 2.8.

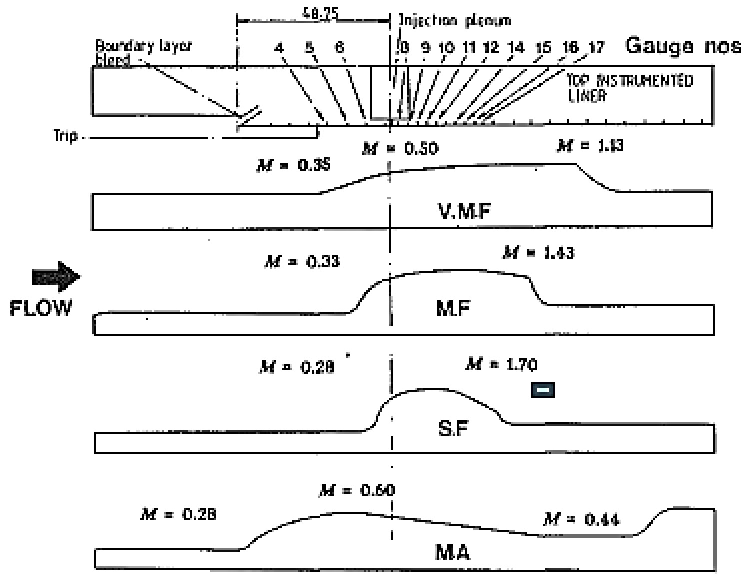

Figure 2.7: Flow Pressure Gradients Used by (Teekaram et al. [27])

The study by Ekkad et al. [28] examines the simple round hole and the cooling effects of rotating the exit hole by a compound angle of β = 0, 45, and 90 degrees. Rotating the hole by a second, compound angle, allows some distinct advantages over a completely streamwise facing hole. While experimenting with blowing ratios at M = 0.5, 1.0, and 2.0, it was determined that adding a compounding angle does increase cooling effectiveness over a surface. Both the β = 45° and 90° cases yielded a higher cooling effectiveness at all three blowing ratios. The blowing ratio of M = 1.0 had a higher cooling effectiveness than at M = 2.0, which agrees with all the previously reviewed studies of round holes, due to coolant lifting off the surface past blowing ratios of approximately M = 1.5. These tests also included operating the same conditions at a higher density ratio greater than DR = 1.0. While running at the density ratio of DR = 1.46, varying effects were observed. All tests that included a streamwise facing

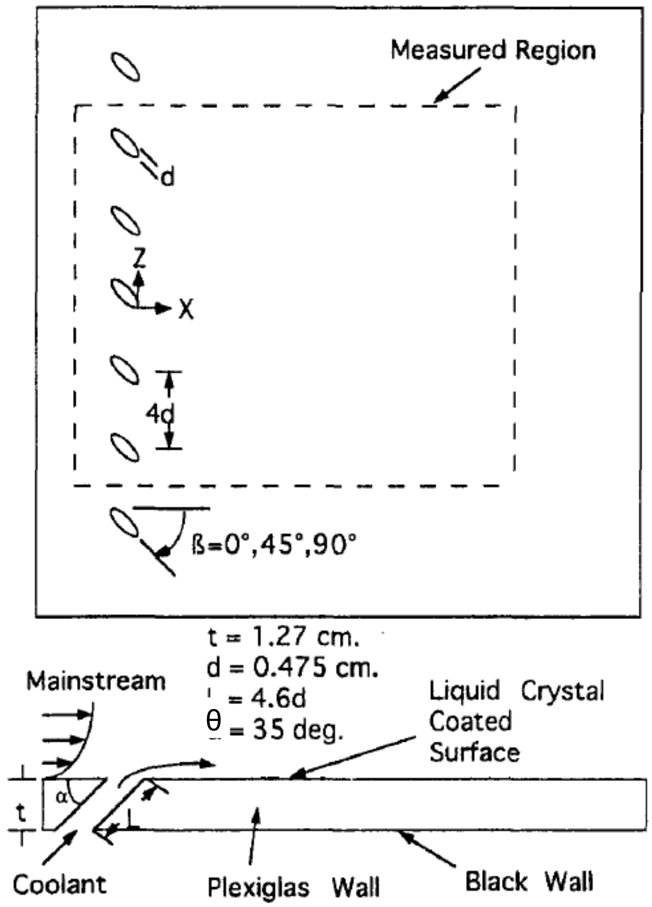

Figure 2.8: Compound Injection Angle From the Study by (Ekkad et al. [28])

hole had a higher cooling effectiveness at every blowing ratio. When looking at the compound angle hole, higher density ratio tests showed an improved cooling effectiveness at the lower blowing ratios but reduced effectiveness at the higher blowing ratio of M = 2.0.

The effects of a compound angle have been examined by both Ligrani et al. [29] and Schmidt et al. [30.] Both looked at round holes with a compound angle between $\beta = 50°$ and 60°. At this lateral hole spacing, there is minimal flow interaction between the holes. This prevents the coolant from building up in the boundary layer, as is seen in effusion cooling. Both studies show an initial increase in cooling with the compound angle; however, past the lateral distance of approximately X/D = 10.0, the compound angle no longer gives an increase in cooling over the plate.

In order to increase the cooling effectiveness further down the surface of the plate, it is possible to decrease the lateral hole spacing of the round holes. Schmidt et al. [30] and Sen et al. [31] used round holes of a similar size with a 3-D hole spacing; with this design, the cooling effects are now improved over the 6D case. The holes are now close enough together that coolant from one hole blows into the coolant of another, allowing the coolant to build up over the surface. The cooling effectiveness values are shown to be approximately twice as high as the round hole for the measured distance of X/D = 3.0 to 15.0. The differences are seen in Figure 2.9. In this configuration, the round hole is able to provide more effective cooling over a surface than any other non-effusion, round hole configurations in this study.

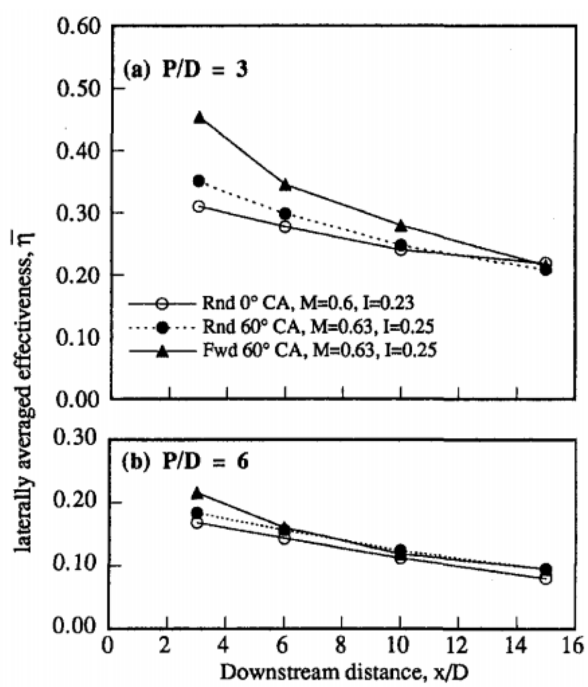

Figure 2.9: Lateral Round Hole Spacing Comparison (Schmidt et al. [30])

An additional factor which must be considered, is that most film cooling tests are performed using a plenum as the coolant supply source. Using a plenum ensures proper mixing of the coolant and an even distribution of cooling air to all the holes. In effect, the plenum acts as a chamber relatively full of static air for each test. This is not the reality in actual turbine cooling. The cooling air is flowing past the film cooling holes and will have significant pressure drops as it makes its way to the surface of the blade. Additionally, the momentum of the air moving past the hole will cause other entrance effects and push more of the coolant to one side of the cooling hole as it rushes past the hole on the inside of the blade. A demonstration of this effect is seen in Figure 2.10. Thole et al. [32] studied additional cases on the effects of entrance crossflows. For the blowing ratio of $M = 0.5$, there was minimal effect on the cooling effectiveness.

Film cooling hole entrance design should be understood and optimized to prevent these crossflow influences. Looking at a round hole, when there is very little crossflow, there is a resulting flow separation on the downstream side of the hole and the jet will tend to exit on the upstream portion of the hole. The opposite occurs when there is a high crossflow at the entrance. The flow will separate on the upstream side of the hole and the flow will tend to exit on the downstream edge of the hole. In both of these cases the flow is exiting asymmetrically, which then causes increased turbulence along the surface. That turbulence increases mixing between the coolant and mainstream, which leads to a reduction in cooling effectiveness.

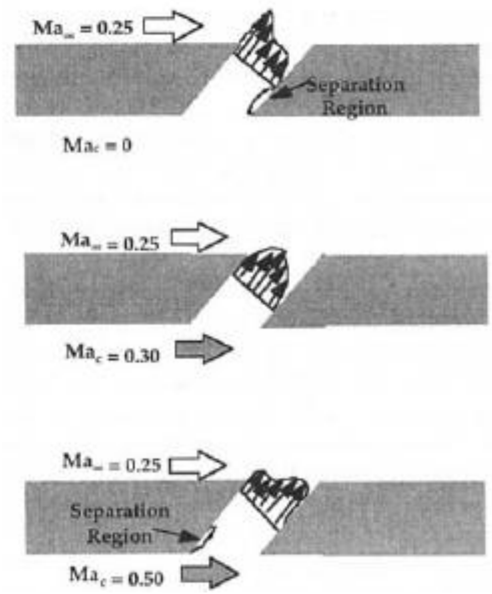

Figure 2.10: Variable Flow Velocity Profile Through a Cooling Hole from Thole et al. [32]

Film Cooling With Advanced Shaped Holes

With the advent of more advanced manufacturing techniques, including finish processing laser drilling and electro metal discharge (EDM), it is possible to design, build, and test other cooling geometries besides a round hole. Gritsch et al. [33] examined the cooling effectiveness between the standard round hole and more complex cooling geometries. Figure 2.11 shows which cooling geometries were tested. There are two ways to expand the film cooling holes to make them more efficient at cooling. The first is to expand the exit laterally from the center, while still at the same incidence angle, this in known as a fanshaped (FS) hole. The second way is to add a secondary angle in the middle of the hole, this is called a laidback fanshaped (LFS) hole. The laidback angle can add 10 to 20 degrees to the angle of the hole.

The results from this study indicated that the FS and LFS both provide improved cooling effectiveness over the standard round hole. This is done by improving the lateral spread of the coolant over the surface. As it was seen in previous studies, this reduces the effectiveness at X/D locations further downstream but the large increase in lateral effectiveness offsets this loss. However, while at the blowing ratio of M = 1.0, both the round and FS holes show a decrease in cooling effectiveness, while the LFS was not significantly affected until a blowing ratio of M = 1.5 was tested. The LFS holes give more efficient cooling over the surface at a wider variety of operating conditions. The results also show that the LFS holes have reduced the momentum in the flow, allowing it to stay attached to the surface. This means the advanced shaped holes become more resistant to entrance flow effects which can also reduce cooling effectiveness. They are also more resistant to the mainstream flow conditions reducing effectiveness, and actually are able to become more effective with blowing ratio increases.

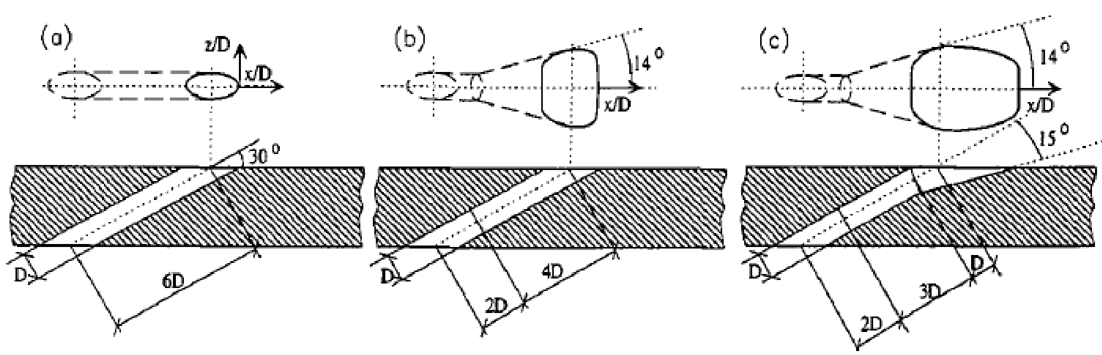

Figure 2.11: Round Fanshaped, and Laidback Fanshaped Cooling Geometries Tested by Gritsch et al. [33]

Compound Angle Effects on Advanced Shaped Holes

Advanced shaped holes are good at keeping the cooling flow attached to the surface. Looking especially at holes that are either fanshaped or laidback fanshaped, these types of holes are able to slow down the flow before it exits onto the surface. This results in a reduction of the cooling flow momentum just before it reaches the surface. In addition, because the fanshape opens at a low angle (≤15°), the flow can stay attached to the surface of the advanced shape longer, thus, lateral spreading of the coolant is also increased. Bell et al. [34] has looked at combining advanced shaped holes with compound angle cooling technology, to take these advanced hole geometries further. It has been shown that orientating film cooling holes with a compound angle will help to further increase lateral spreading of the cooling jet. This was indeed the case for these results. Figure 2.12 shows the geometries tested, with the hole labeled LDCA showing the highest effectiveness over all testing conditions. An additional study by Brittingham and Leylek [35] shows comparable results while looking at a laidback round hole and laidback fanshaped hole similar to the one tested by Bell et al. [34].

Shaped film cooling hole geometries are able to increase cooling effectiveness partly because of their anti-vortex properties. By spreading out the flow laterally and reducing the flow velocity just before it reaches the surface, the vortices that are generated are greatly reduced. This property is important to how well these cooling holes perform. Vortices increase the film mixing by pulling the hot mainstream gas down to the surface of the blade. This leads to the reduction in cooling effectiveness downstream of the blade.

Due to these effects, it is important to reduce these vortices and continue testing with advanced shapes to keep increasing cooling effectiveness. Additional studies have also been performed with consistent findings. Lee et al. [36] used the steady state liquid crystal method with a wide band TLC paint to measure the adiabatic film cooling measurements. Looking at round holes with an inclination of θ = 30° and an additional laidback angle of γ = 15°. Three compound angles were tested in this experiment, a β of 0°, 30°, and 60°, as seen in Figure 2.13. For these experiments the three blowing ratios of M = 0.5, 1.0, and 2.0 were used for comparison.

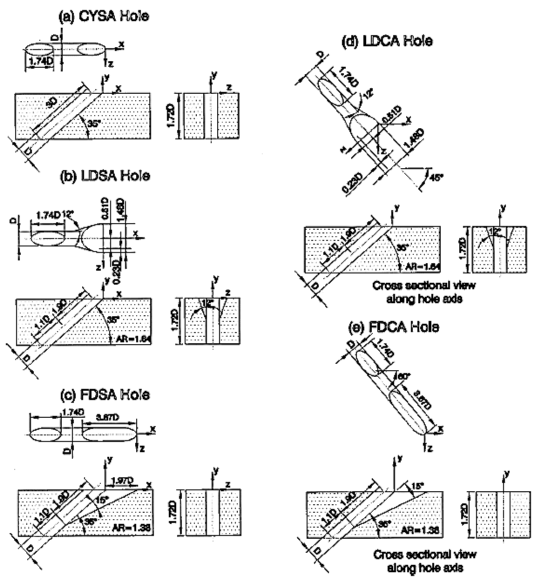

Figure 2.12: Compound Angle Advanced Cooling Geometries Bell et al. [34]

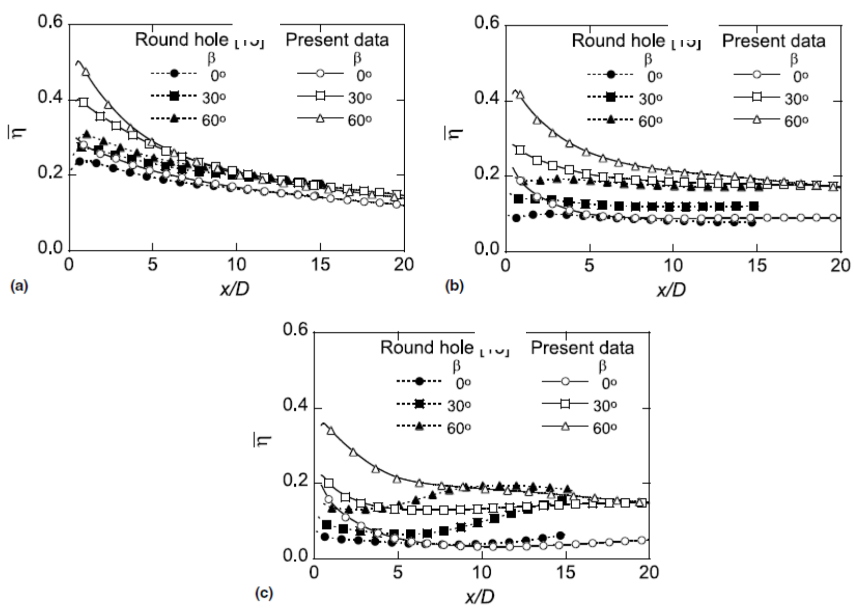

Figure 2.13: Round Hole Versus Laidback Hole at Different Compound Angles, Tested with Blowing Ratios of M = 0.5, 1.0, and 2.0 (Lee et al. [36])

To compare these results, the basic round hole with no laidback angle was used producing two significant results. Unlike with the basic round hole geometry, the addition of the laidback angle provides additional lateral spreading around the injection site of the hole. These effects are seen even at the higher blowing ratio of $M = 2.0$. The results show that with the addition of the compound angle of either $\beta = 30°$ or $60°$, the cooling effectiveness was markedly improved over the comparable laidback round hole with no compound angle or a $\beta = 0°$. These results show strong promise that the effectiveness can be further improved with advanced geometries at additional compound angles on the turbine blade.

Other advanced geometries, besides the laidback fanshaped hole, have been evaluated to help improve the cooling effectiveness. Ramesh et al. [37] shows a new type of film cooling design using a “tripod” approach. Out of each entrance three different exits are used to distribute coolant. These different geometries are seen in Figure 2.14. The six geometries are different forms of the same two hole types. A round hole and a laidback fanshape hole are put together in three different ways to create the most efficient film cooling hole possible. The third and fourth hole geometries are a version of the straight holes being combined together with no transitions. These two types of holes have hard angles for the flow to follow. The fifth and sixth holes have fillets at the entrance of the hole and at the transitions to each of the branches. These fillets make it easier for the flow to stay attached to the walls of the cooling geometry. This also decreases the coolant turbulence coming from of the hole which in turn increases cooling effectiveness. The final results have shown that the filleted tripod shaped holes can outperform the basic round hole while using approximately half the mass flow of coolant as the round holes

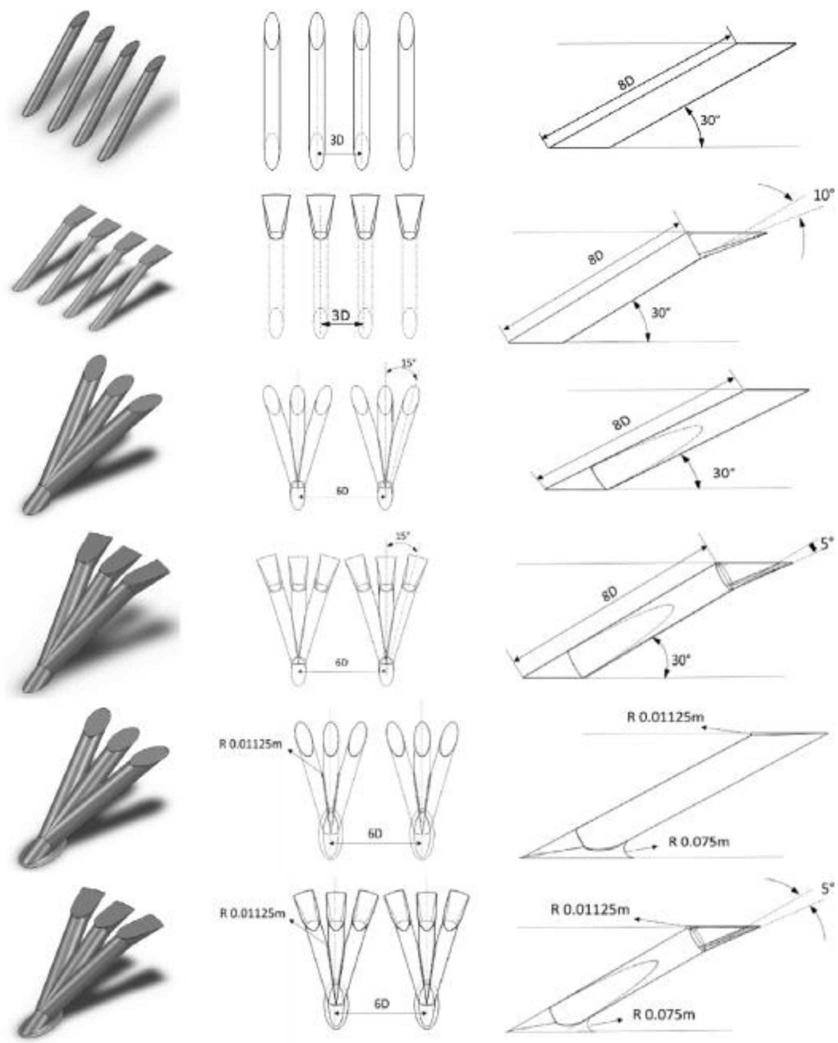

Figure 2.14: Experimental Tripod Geometries (Ramesh et al. [37])

consume. This is possible because the tripod holes more effectively distribute the coolant laterally across the surface. This shape of hole is also designed to be an anti-vortex hole and reduce the lift off vortices that increase mixing of the mainstream and coolant flows.

Film cooling is not the only method used to isolate the turbine blades from the mainstream gas, the external shielding methods have also been introduced to help isolate the turbine components. Thermal Barrier Coatings (TBC) have been used for over 50 years to help decrease the severity of oxidation and improve cracking resistance from high heat in combustors and thrust augmenters Meier and Gupta [38]. Until recently zirconium dioxide (ZrO_2) was used to coat components in the turbine, but its high heat transfer coefficient and tendency to allow creep means that it has been phased out (Cao et al. [39].) These techniques have been replaced with other new plasma or electron beam physical vapor deposition (EB-PVD) methods that will help components resist the high heat in the turbine and extend engine life.

Film cooling has been shown to be able to shield turbine blades from extreme heat while also keeping the turbine blades at temperatures low enough below their critical temperature that the blades do not fail. Through the continued study of film cooling, more advanced and efficient film cooling designs can and will be created. The study and application of these designs will lead to engines that require less cooling air and will in turn become more powerful and efficient.

This literature review has revealed several factors which effect the performance of film cooling geometries. Whether looking at the effects of flow conditions or outlet geometries it is easy to see the how many different factors affect cooling performance. While many studies have been performed with the round hole and compound angle, there are few that show these effects for more advanced laidback fanshape geometries. This research will help fill the gap of data that exists in this area of film cooling. If it is true that improved cooling performance can be achieved by simply adding a compounding angle to the advanced hole geometries; it is very important to know what the true effects would actually be.

CHAPTER THREE

Pressure Sensitive Paint Measurements Used For Film Cooling Effectiveness Measurements

Previous Film Cooling Measurement Methods

The film cooling effectiveness (η) is used to quantitatively compare different film cooling hole designs. It was seen previously that CFD codes have been used to perform this task; however, it is still necessary to obtain the cooling effectiveness distributions experimentally. To define η, three temperatures are required, with the cooling effectiveness being defined in Equation 3.1.

$$\eta = \frac{T_{Film} - T_{\infty}}{T_{Coolant} - T_{\infty}} \tag{3.1}$$

The temperature of the mainstream gas (T_{∞}) must be known; in a laboratory setting, it is straightforward to determine this with a thermocouple inserted into the flow. This is also a suitable method because it is safe to assume that the temperature of the mainstream gas is homogeneous. The coolant temperature ($T_{Coolant}$) must be known to give an accurate reduction in temperature over the surface. It is also necessary to obtain the temperature of the surface and the temperature of the film over the surface. It would be difficult to use thermocouples to obtain the temperature of the film (T_{Film}) as the thermocouple itself could alter the flow characteristics of the film and the effectiveness results. The film also has a temperature gradient within the boundary layer and attempting to represent this with thermocouples would yield inaccurate results. The surface temperature could also be represented with thermocouples. This however causes some issues. If the film cooling effectiveness was determined using a steady state heat transfer technique, the heat loss of the experiment would need to be calculated. Also, the heat transfer through the wall would need to be taken into account. The heat transfer test could be run in a transient form; however, it still requires a short time limit on the transient test which can cause some issues. Optical based, non-intrusive, mass transfer techniques, should instead be used to show the cooling effectiveness. Optical based measurements are preferred for these types of tests over thermocouples because of the detailed distributions that can be achieved. Each pixel for an optical based method is used as a measurement point giving detailed information on the flow field. Several types of methods use cameras to capture results. Some of these methods do depend on the adiabatic wall condition while other methods can obtain results independent of the heat transfer conditions through the wall.

Camera Based Measurements Systems For Film Cooling Effectiveness

Many of the previous studies reviewed in Chapter Two used the Thermochromic Liquid Crystal Technique (TLC). The TLC techniques are based on the paint reflecting various colors while it goes through a phase change. This phase change is triggered by the heating of either the wall to which the paint is applied, or the mainstream air. As the paint is warmed, it transitions from a solid to a liquid. The paint starts clear and transitions through the entire color spectrum and then back to clear when it is fully a liquid. A typical color transition is seen in Figure 3.1. The ratio of liquid to solid paint determines the color that is reflected after being illuminated by a white light source. Because a digital CCD camera is used to measure the intensity of the incoming light protons. This means that each pixel is considered to be a sensor. With thousands of pixels in the camera, it is possible view the detailed temperature distribution over a surface.

The camera sees the paint in red, green, and blue (RGB) colors. The recoded images are then usually converted to hue, saturation, and intensity (HSI) to be processed. By making this conversion, the test becomes more accurate with fewer modifiable variables.

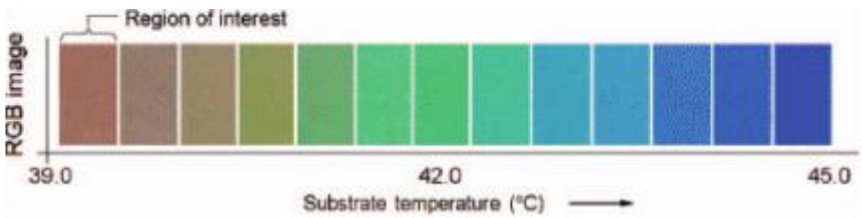

Figure 3.1: Wide Band TLC Light Transition Scale (Sikarwar et al. [40])

Intensity is controlled during the testing procedure by maintaining consistent and constant lighting. The saturation is controlled by a computer and is set to a constant, preventing saturation from effecting results between tests. The hue is the only variable which can change and is directly related to the color seen by the eye during the test. A TLC test requires there be a previously established calibration between the emitted hue of the TLC and the temperature to which it corresponds.

This technique can either be performed as a steady state or transient technique; Critoph et al. [41] directly compared the two methods when finding the heat transfer coefficient over pin fins. When running as a steady state test, generally a wide band TLC paint is used with a temperature range of 5 to 20°C. This is a less sensitive type of paint, as the change in color has to correspond to a larger temperature range. A second issue with this method is that the heat loss must also be approximated and considered in the calculations. These two issues can be avoided when using TLC in the transient test form. The colors emitted only need to span for a few degrees of temperature change, improving accuracy. With a more narrow temperature band and the time it takes to reach each color, the heat transfer coefficient can be approximated. It is possible to determine the heat transfer coefficient in internal flows with only one range of TLC. Baughn et al. [42] showed while studying internal cooling with pin fins, only one set of data was collected, this type of testing then only required one equation and one unknown. The film cooling effectiveness can be solved for by substituting equation 3.1 into equations 3.2 and 3.3. The two equations are iteratively solved for. The results yield both the film cooling effectiveness and heat transfer coefficient being solved for at the same time.

$$\frac{T_{w1}-T_i}{T_f-T_i}=1-\exp\left(\frac{h^2\alpha t_1}{k^2}\right)erfc\left(\frac{h\sqrt{\alpha t_1}}{k}\right) \tag{3.2}$$

$$\frac{T_{w2}-T_i}{T_f-T_i}=1-\exp\left(\frac{h^2\alpha t_2}{k^2}\right)erfc\left(\frac{h\sqrt{\alpha t_2}}{k}\right) \tag{3.3}$$

Other optical based sensing methods have been used in film cooling studies. Temperature Sensitive paint (TSP) has been used by Kunze et al. [43] to show cooling effectiveness results of a single row of holes on the end wall of a turbine blade. The TSP method also uses each pixel of a digital camera as a thermocouple. Similarly to the TLC technique, this is also a non-intrusive method to determine the heat transfer coefficient or the cooling effectiveness over a surface. The paint is excited by a 460nm light source, which causes the paint to fluoresce. This type of paint is “temperature quenched.” As the temperature of the paint increases, the fluorescence of the paint will begin to diminish. This change in fluorescence is related to a temperature much in the same way TLC equates the color spectrum to a temperature. The TSP method also requires establishing a calibration curve to relate the brightness of the fluorescence paint to the temperature at the surface. The full testing procedure and applications are shown by Lorenz et al. [44] with a completed TSP setup and calibration plot shown in Figure 3.2. As well as with TLC, the TSP technique can also be performed as a steady state, shown by Fey et al. [45], or a transient technique.

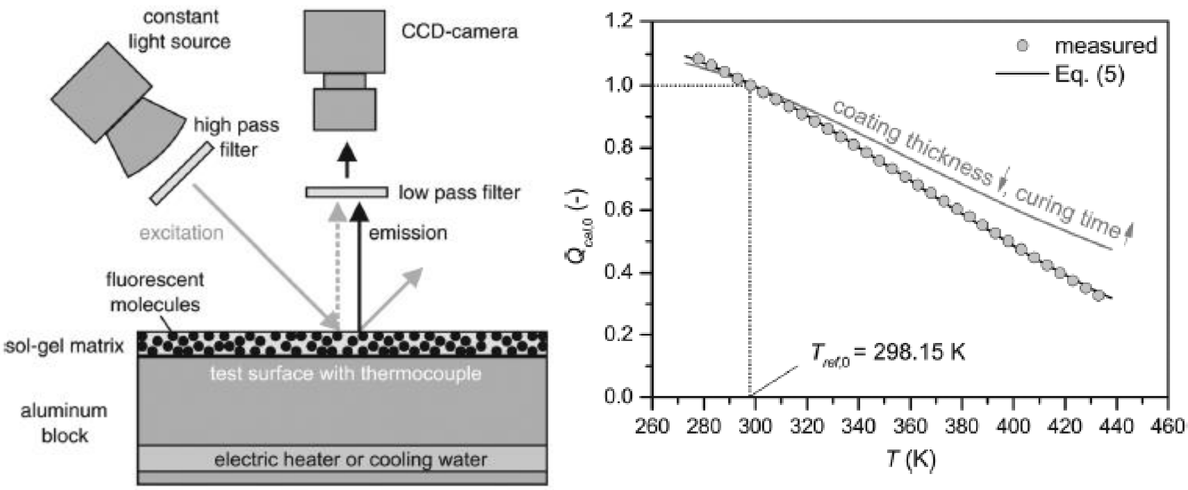

Figure 3.2: TSP Setup and Calibration Plot (Lorenz et al. [44])

A third method, called Infrared Thermography (IR), can also be used to measure the heat transfer or cooling effectiveness coefficients over a surface. This is also a non-intrusive technique; however, it does not require the surface to be covered with any reacting paint. Instead, the best results for this method are achieved when the surface is painted matte black. IR detectors measure the radiation from the surface to determine the temperature distribution. The best results are shown when the surface emissivity (ε) is close to one, like a surface with a matte black finish. Equation 3.4 is the governing equation in this method. This equation describes the heat transfer rate of thermal energy between the experimental surface and the camera in terms of radiation and is based of the difference in temperature between the two objects. This difference being defined by ΔT.

$$\dot{Q} = \sigma\varepsilon A \Delta T_w^4 \tag{3.4}$$

The heat transfer rate can then be used to determine the heat transfer coefficient over the surface. Because the infrared method directly records the temperature of the surface the film cooling effectiveness can also be determined. Schulz [46] shows how this technique can be especially useful in finding the cooling effectiveness coefficient. This can also be conducted as either a steady state or transient technique.

Determining the Film Cooling Effectiveness with Mass Transfer Techniques

Each of the three previous methods can be, and are, used for measuring heat transfer coefficients. All of these methods are affected by the amount of heat in the test section, and, to use a traditional heat transfer experiment, a temperature difference must be created between the surface and the mainstream or coolant flow. These types of tests can have two important weaknesses: they rely on the assumption of no heat transfer through the wall while running in a steady state or they rely on the measurement of time during a transient test. To avoid these concerns, it is possible to use mass transfer techniques to quantify the film cooling effectiveness. Mass transfer techniques work well for film cooling studies because mass cannot pass through a solid wall, compared to heat conduction through the wall in a heat transfer test. This means no adiabatic wall assumption is required. Mass transfer techniques rely on the mixing of two separate gases, this mixing problem is seen in Equation 3.5.

$$\eta = \frac{C_{Film} - C_\infty}{C_{Coolant} - C_\infty} \tag{3.5}$$

When the ratio of each gas is approximated, it is possible to understand and calculate the cooling effectiveness. This method has one caveat, the concentration of the gases at the wall must be measured without compromising or disturbing the flow in the boundary layer. Various techniques have been developed which follow this system. The most basic is the foreign gas sampling technique, seen in Figure 3.3. This method works by having sampling ports in the surface downstream of the film cooling holes as seen in Figure 3.3.

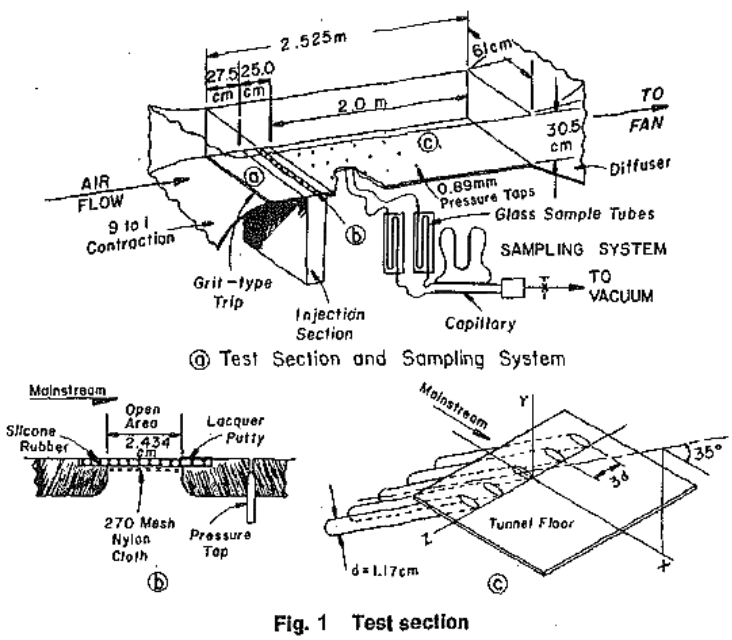

Figure 3.3: Foreign Gas Sampling Setup (Pederson et al. [47])

The concept behind this method is very simple. Downstream of the film cooling holes, the gases will mix together in the boundary layer. Close to the film cooling hole, the concentration of the coolant gas will dominate, while downstream of the hole the mainstream gas will dominate the mixture. Foreign gas sampling takes a small sample of the gas at each port in the surface to measure the different concentrations of each gas at different X/D locations downstream of the cooling holes. These holes in the surface must be small enough so that they do not interfere with the boundary layer, while still allowing it to sample the gas in the test. This method has the drawback of only being able to take samples at the discrete points of the hole locations. Shown by Ito et al. [48], this method at best can then only give a local cooling effectiveness along the surface and is not sensitive enough to see the rapid change in cooling effectiveness at low X/D distances.

A separate mass transfer technique called the ammonia-diazo technique can be utilized for more detailed flow visualization and measurement of the film cooling effectiveness. This technique is based on the reaction of water and ammonia with the diazo coated surface. This surface is usually paper which has been covered in the diazo mixture. When the water and ammonia mixture comes into contact with the surface, the water is absorbed into the paper and the ammonia reacts with the diazo. This creates darker portions in the areas of higher concentrations of the water and ammonia mixture. The coolant is seeded with the mixture and the mainstream flow is left with no seeding at all. Before the two flows meet, this means that the coolant flow has an ammonia water concentration of 100% and the mainstream flow has a concentration of 0%. Friedrichs et al. [49] and Goldstein and Stone [50] used a cascade style wind tunnel and the ammonia diazo technique in order to determine detailed plots of film cooling effectiveness. The cooling effectiveness results and concentration scale are seen in Figures 3.4 and 3.5. These plots of concentration of the ammonia and water mixture on the surface, this determines the color change on the surface. These different shades are what is used to determine the film cooling effectiveness.

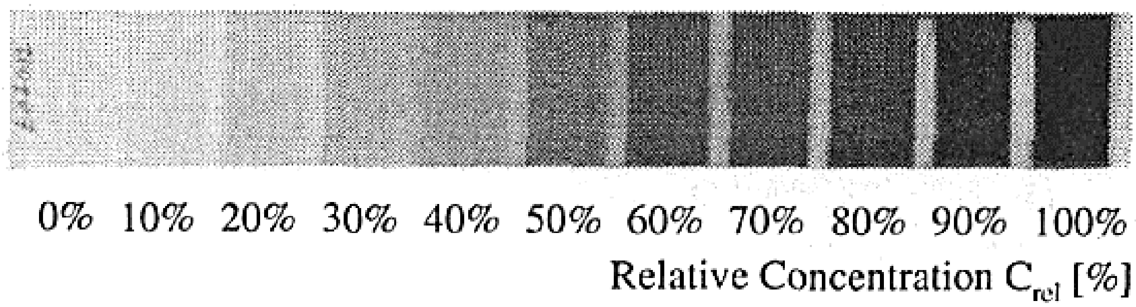

Figure 3.4: Ammonia Diazo Scale (Friedrichs et al. [49])

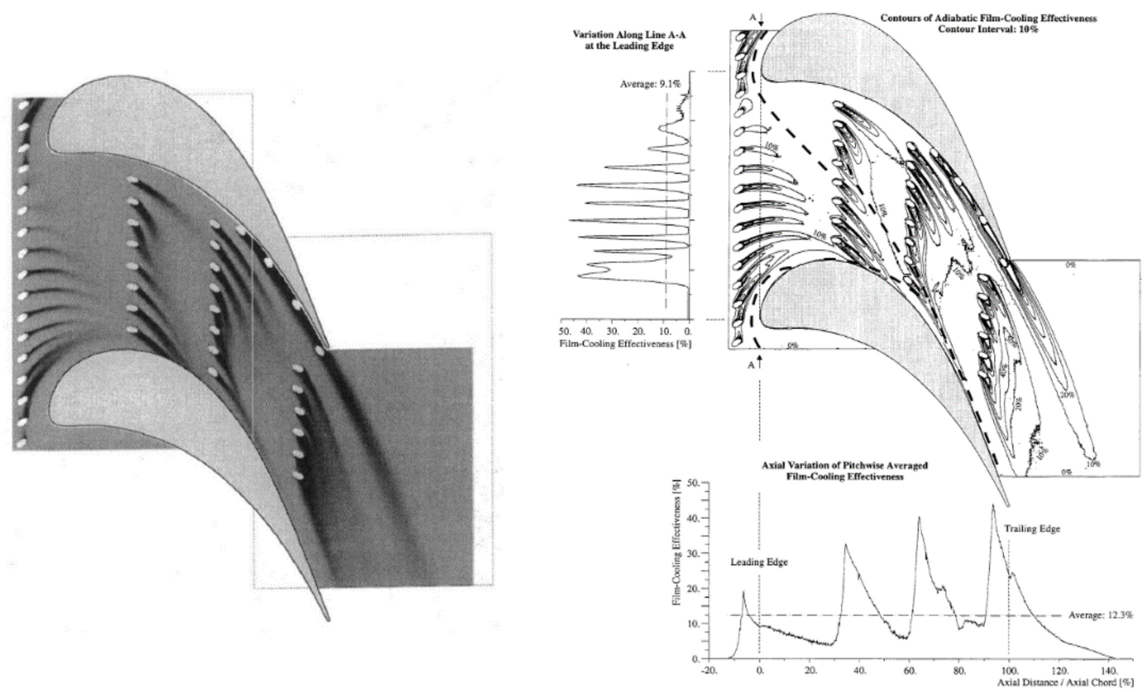

Figure 3.5: Sample Ammonia Diazo Film Cooling Effectiveness Results (Friedrichs et al.[49])

Operational Theory of PSP

The first idea of correlating luminescent molecules with varying pressure levels came from Hans Kautsky in 1935; this is also when the concept of oxygen quenching was observed [51]. The luminescent paint and mass transfer technique was not adapted for film cooling until the 1980's and 1990's, as seen by Morris et al. [52]. Pressure Sensitive Paint (PSP) is comprised of two parts, an oxygen sensitive fluorescent molecule and an oxygen permeable binder ISSI [53]. When the paint is illuminated by an energy source such as an LED light in a wavelength range of 380nm to 520nm [53], the fluorescing molecules reach an excited level and begin to fluoresce. These particular fluorescing molecules are affected by the amount of oxygen in the air contacting the paint. This is known as being oxygen quenched and is shown in Figure 3.6. As the paint is energized by the light, the molecules want to return to an unexcited state. The actual recorded images are of the emission of energy by the molecules when they return to ground state.

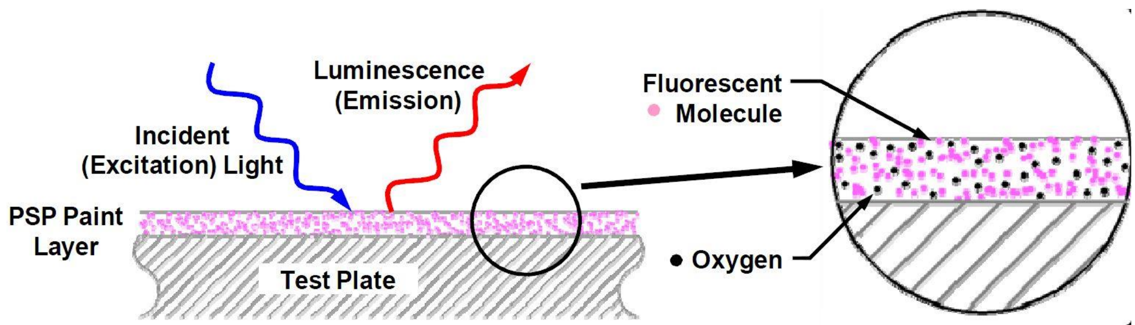

Figure 3.6: Basic PSP Theory [54]

The film cooling effectiveness can be defined in terms temperatures of the film and mainstream flow. The cooling effectiveness can also be defined in terms of the concentrations of gases in the flow instead of temperatures. PSP is oxygen quenched method, which means that for this technique, the concentration in the film and mainstream flow should be considered with the introduction of a foreign gas as the coolant, the concentration of oxygen at the surface is considered to be 0% inside the film cooling holes and gradually increases at further X/D locations from the trailing edge of the hole. This assumption is made because there is no oxygen in the gas used as coolant flow. As it has been stated, the intensity of the fluorescence of the paint is determined by the local partial pressure of oxygen on the surface at that point. The pressure of the oxygen is related to the temperatures of the film and mainstream according to Equation 3.6. This is then used to determine the cooling effectiveness.

$$\eta = \frac{(T_\infty - T_{Film})}{(T_\infty - T_{Coolant})} = \frac{(C_\infty - C_f)}{(C_\infty - C_C)} = \frac{(P_{o_2})_{Air} - (P_{o_2})_{Mix}}{(P_{o_2})_{Air}} \tag{3.6}$$

The film cooling effectiveness can now be redefined from what has been seen in Chapter One. C_∞ is the concentration of oxygen in the mainstream flow. C_C is defined by the concentration of oxygen in the coolant flow before it has entered onto the surface, and C_f is the concentration of oxygen in the film along the surface. It is safe to assume that the concentration of oxygen in the coolant flow before the surface is always zero percent. That leads to the furthest simplification of Equation 3.6. The value for $(P_{O_2})_{Air}$ represents the partial pressure of oxygen in the mainstream flow, while $(P_{O_2})_{Mix}$ represents oxygen partial pressure in the film on the surface. The 'Air' defined as the partial pressure of oxygen on the surface in the mainstream flow with air acting as the coolant and mainstream gas. While the 'Mix' is defined as the pressure oxygen on the surface within the area which is affect by the film from the cooling holes.

Film Cooling and Pressure Sensitive Paint Review

Before the PSP method was widely accepted and used as it is today, the method first had to be validated. This was done by comparing the technique to methods which where previously reviewed in this chapter. This has been done is several studies; Caciolli et al. [55] used PSP and TLC to measure the effectiveness of multi-perforated plates used in combustor cooling. The findings show that PSP and TLC were both able to produce similar results with PSP being advantageous because it did not have to be performed as a transient test. Navarra [56] performed a direct comparison of the PSP and TSP methods and found minimal difference in the results just as Caciolli [55] did. Wright et al. [57] has performed a comparison of the PSP, TSP, and IR methods for finding the cooling effectiveness over a flat plate. It was show that the three methods had minimal differences in results. Now as the PSP method has been validated and accepted, it is one of the standard methods in evaluating cooling effectiveness for film cooling on turbine blades. Gao and Han [58] have used PSP to investigate leading edge showerhead film cooling. Suryanarayanan et al. [59] has examined the effects of rotation on different film cooling geometries, this type of testing is more symbolic of the conditions that are seen in an engine. Then on the trailing edge of the surface, Taslim et al. [60] shows the effects of different configurations on the cooling effectiveness. As well as the different regions of the turbine blade from the leading edge to the trailing edge, also on the pressure and suction sides, PSP is used to determine the cooling effectiveness for every type of the turbine blade. This specialized pressure measurement technique has found a very specific niche in the film cooling turbine industry and it will continue to be at the forefront of testing and validating new hole geometries for the foreseeable future.

Performing Film Cooling Tests With PSP

PSP relates oxygen partial pressure over a surface to a level of cooling effectiveness. Obtaining a detailed distribution of pressure measurements on the surface with more traditional methods is very difficult if not impossible. So instead this is done by relating the intensity of the fluorescence of the paint to the pressure of oxygen that is actually on the paint. In order to accomplish this, a reference calibration must be established.

This calibration starts at local atmospheric pressure. The total atmospheric pressure is measured with a barometer and entered in as the total pressure of the atmosphere. A standard value for this cannot be used as atmospheric pressure constantly changes. A calibration plate that has been painted with PSP at the same time as the testing surface is used in a vacuum chamber where the ambient pressure can be controlled and measured with a pump and gauge. By using this chamber, the same CCD camera, and a 400nm light source, a correlation is created. The pressure is gradually decreased in the chamber while the plate is illuminated. The camera then records the intensity of the fluorescence from the calibration piece. Three types of images have to been taken for the calibration. A black set of images are taken to prevent optical noise from the camera affecting the calibration curve. These black images are taken with the LED light off and with atmospheric pressure on the calibration plate. A reference set of images is also recorded, with the LED light on and still with atmospheric pressure on the plate. This set of images is the reference to the ambient atmospheric pressure fluorescent intensity when the pressure is reduced in the vacuum chamber. To complete the calibration, sets of images are recoded in increments of four inches of mercury from full atmospheric pressure to a near complete vacuum at -28mmHg.

A sample size of 250 images is taken and averaged on a pixel by pixel basis to determine the distribution to be used for analysis. This analysis is done with Equation 3.7.

$$\frac{I(P)_{ref} - I_b}{I(P) - I_b} = f(P, P_{ref}) \tag{3.7}$$

In equation 3.7, $I(P)_{ref}$ represents the recorded intensity of the reference images taken in of the calibration piece. I(P) is the intensity of the plate as the pressure is gradually decreased in the vacuum chamber, and I_b is the measured intensity recorded with no light source to eliminate camera noise. A diagram of the calibration vacuum chamber is seen below in Figure 3.7.

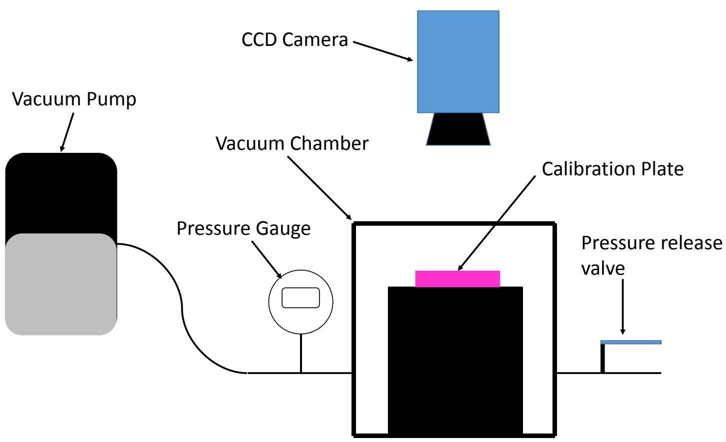

Figure 3.7: Vacuum Chamber Setup for PSP Calibration

Once the images have been taken from the calibration piece, the calibration curve can then be determined. The intensity of the black, reference, and the reduced pressure images are input into equation 3.7 to determine a value for the intensity ratio. A sample calibration curve is seen in Figure 3.8.

The PSP calibration has now been established, so the experiment can be conducted and post processed. For the actual experiment, four types of images are required. A black, reference, air, and mix set of 250 images each must be taken. The black images are taken with no light and no air passing through the tunnel; this again is done to eliminate camera noise from effecting results. The reference images are taken to

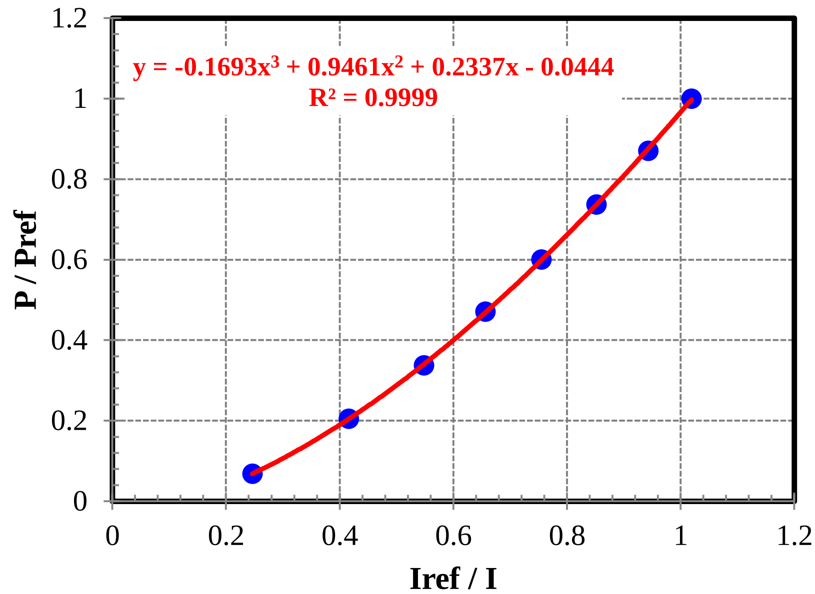

Figure 3.8: Sample PSP Calibration Curve

establish the ambient air pressure conditions is the tunnel. These images are taken with no mainstream or coolant flow through the tunnel; in this case the LED light is illuminating the plate. Air images are also taken in each experiment. These images are taken with the light source on, the mainstream flow on, and the coolant flow on with regular air as the coolant. In equation 3.6 the partial pressure of oxygen on the surface in the mainstream air, without any foreign coolant, must be known. The air images are taken at the same flow rates as the mixed gas images allows this calculation to be completed and used to find the cooling effectiveness. In addition, these images help to ensure a proper calibration for each test. Finally, the mix images are taken. The mix images are taken when the foreign gas is introduced as the coolant to displace the oxygen and thus reduce the oxygen partial pressure on the surface of the PSP. This allows for the illumination of the paint and the fluorescence to be recorded.

Uncertainty in the PSP Experiment

The experimental uncertainty of the PSP must be addressed. While experimenting with PSP, the CCD camera is one of the largest contributing factors of error in this method. Mendoza [61] shows these effects introduce camera noise that must be taken into account with black images and pixel-to-pixel variability that cannot be avoided that is different for each camera. The camera itself comes from the factory with pixel uniformity brightness of 2%. At dark conditions the camera has a uniformity darkness of less than 20 e^- rms. So at most there is a five percent difference in the darkness recorded by all of the camera pixels. Only one test is taken under these conditions during the experiment and with the average of many images, this becomes less significant. With the noise in the system, it becomes even more important to keep the camera from moving and introducing additional errors. Natsui et al. [62] and Liu [63] have outlined all sources of possible error while conducting PSP experiments. It was shown specifically by Natsui et al. [62] that the ambient room temperature for the testing and calibration must remain constant because the luminescent intensity of the paint will vary with different temperatures. All sources of error can be taken into account and approximated using equations described by Kline and McClintock [64]. Equation 3.8 is the final equation uncertainty calculation. It is necessary to take the partial derivative of each variable in the equation. The error of each variable, the intensity of the reference images for example, will then be multiplied by the derivative equation result. The partial derivative isolates the effect of each variable on the equation and the calculated error of the intensity values, factors in variations and differences in the recorded images. These terms will all be squared and then summed with every variable in the equation. The square root of this sum is the uncertainty of the results.

$$W_R = \sqrt{(dI_{mix} * error_{mix})^2 + (dI_{air} * error_{air})^2 + (dI_{black} error_{black})^2 + (dI_{ref} error_{ref})^2} \quad (3.8)$$

In these experiments the measured uncertainty was performed for effectiveness values of η = 0.99 and 0.35. As expected there is a difference in the results. Overall the uncertainty in the camera dominates the uncertainty that comes from the calibration. This means that only the uncertainly of the recorded test images is taken into account. For the higher effectiveness an uncertainty of 2.0 percent was calculated while the lower effectiveness had an uncertainty of 7.9 percent. The measured uncertainty increases with decreasing effectiveness because the reference and coolant images start to have similar intensities with low cooling effectiveness values. This leads to increased uncertainty in the coolant flows further downstream of the film cooling geometries on the plate. Overall these uncertainties are within the expected values. The best way to reduce errors and uncertainty from the results is to ensure the best possible calibration, use consistent ambient room conditions, and use a calibration piece and test section painted at the same to mitigate the effects of light degradation on the paint. It is also extremely important to prevent the camera from moving and stop the wind tunnel from vibrating as this movement will throw off the calibration and reference images. To ensure the validity of the results, testing is done as precisely as possible and tests are repeated to ensure accurate repeatable results.

CHAPTER FOUR

Experimental Setup for PSP Testing

Wind Tunnel Setup

These experiments were conducted with a newly fabricated, open loop wind tunnel. A 3-D rending of the wind tunnel can be seen below in Figure 4.1. The inlet of the wind tunnel is 61cm x 61cm with an area of 3,716 cm^2. There is a 4:1 area reduction from the inlet to the test section. The test section has a width and height of 30.5cm, giving an area of 929 cm^2.

The overall length of the wind tunnel is approximately 305 cm, with the test section having a length of 121 cm. This tunnel has been specifically designed to accommodate experimentation that incorporates flow over a flat plate or flow around a cylinder. The frame around the wind tunnel has also been created to allow the greatest access to the tunnel, while also supporting the required equipment for PSP testing. Located on the top wall of the test section are two 30.5 cm long and 1.27 cm wide slots that will allow a pitot static probe or other flow measuring devices, to be inserted into the wind tunnel and measure the freestream velocity. These slots are covered with brush door seals; these allow the probe to be located anywhere within the slot, while also prohibiting flow into or out of the wind tunnel. The bottom of the wind tunnel is in three pieces. This allows for only a part of the floor of the wind tunnel to be removed and used to mount the experimental test section. A Soler & Palau, Model DA-20 fan, is attached to the diffuser of the wind tunnel, this fan is controlled by a variable speed controller to allow precise

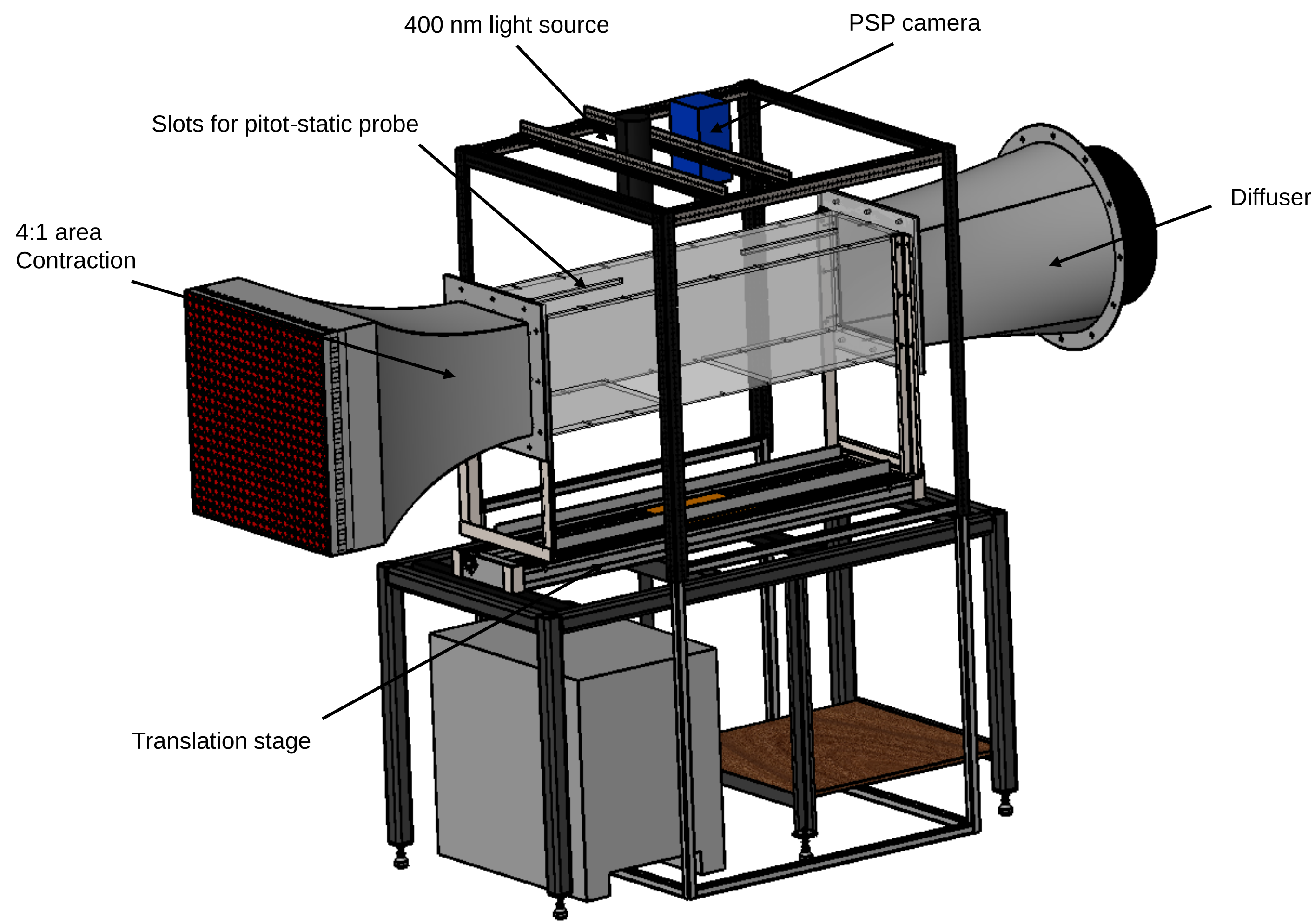

Figure 4.1: Full Wind Tunnel

control of the flow velocity. Inside the inlet of the wind tunnel is a 5 cm thick insert of honeycomb that has 0.635 cm holes to straighten the flow before it enters the contraction into the test section. Inserted between these two honeycombs is a standard 61 cm x 61 cm air filter to further reduce turbulence going into the test section.

Special Wind Tunnel Features

Previous work done by Vinton [65] utilized a 15 cm x 10 cm rectangular wind tunnel. The wind tunnel used in those experiments was symmetric across the x-axis and y-axis, but because it was rectangular in shape, it would not have had the same profile if it had been rotated and placed on the test stand. This new tunnel has been specifically designed to be square symmetric or round symmetric along the entire length of the tunnel. Rotating the tunnel test section, allows a change in the view orientation, without actually moving the sensitive camera equipment. This is advantageous in both PSP and stereoscopic particle image velocimetry (S-PIV) testing, as the results of those tests are extremely sensitive to the movement of the physical hardware around the test section.

The entire wind tunnel and support frame is sitting on a horizontal traverse with a movement range of up to 101 cm. With this linear movement capability, it is easy to run S-PIV experiments at different locations along the flat plate or at different locations on the cylinder. Just like with rotating the tunnel, it will be possible to do this without moving any optics or lights. This is an advantage, because when the equipment is not moved between tests, it is easier to repeat results. The wind tunnel system has been constructed so that all necessary controllers and valves are as close together as possible. Allowing the operator easy use and access to the tunnel components was a top priority.

This wind tunnel assembly is also only 92 cm wide, allowing to fit more easily into the limited lab space.

Experimental Plate Creation and Attachment

Flat plate film cooling experiments were conducted in this wind tunnel. For these experiments a center floor insert was created. The film cooling plates used to test different film cooling geometries, 3-D printed and scaled up. The 3-D printer used to create these plates does not have a large enough print area to cover the entire test section of the wind tunnel. Thus, an insert was created to allow the smaller test sections to sit properly and flush on the floor of the wind tunnel and not disturb the boundary layer that is developing on the walls of the wind tunnel. A plenum is mounted to the bottom of the wind tunnel insert. This plenum allows for even mixing and distribution of the gases used in film cooling experimentation. To help create this even mixing, the plenum is fitted with an insert perforated with small holes to ensure the gases in the flow are evenly mixed. Various gases are needed to achieve the different density ratios that effect film cooling effectiveness. The four gases used in the cooling flow are compressed air, Nitrogen (N_2), Argon (Ar), and Sulfur Hexafluoride (SF_6). Using these four gases, the density ratio was varied from one through four.

Experimental Hole Geometries

For this experiment seven different hole geometries were tested. Five of these holes geometries were derived from pervious work done by Vinton [65.] For the remaining two geometries, Honeywell International provided the designs of two advanced shaped holes. The difference between this work and the work done by Vinton [65] is that the new cooling experiments all have the cooling geometries at an additional compound angle of $\beta = 45°$ from the streamwise direction. At the inlet of each hole, the angle of inclination was $\theta = 30°$. With six of the holes having an additional laidback angle to help increase flow attachment and lateral spreading of the cooling gases on the surface. Important steps were taken to place the origin for the measurements. Starting at the center of the inlet on the bottom of the cooling plate, a line was drawn at the same 30° inclination angle as the inlet until it intersected the top surface. At that point on the top surface, the origin was set. This orientation has the positive x-axis facing in the streamwise direction and the y-axis facing in the lateral direction across the plate. The basic round hole is the baseline for these experiments. For this test the lateral spacing was set at five times the diameter of the hole, the same as was seen in the previous work. Figure 4.2 shows the round hole test section.

Laidback Fanshaped Hole Geometries

Two traditional laidback fanshaped holes have been tested in this experiment. Seen in Figures 4.3 and 4.4, the key difference between the two holes is at the inlet for the coolant. The laidback fanshaped round has a round opening at the start of the hole. This is in contrast to the laidback fanshaped racetrack inlet, which resembles a running track, being twice as long as it is tall. Both of the two inlet geometries have the same hydraulic diameter to allow for an even comparison, with similar coolant mass flow rates and Reynolds numbers. To calculate the hydraulic diameter, Equation 4.1 was utilized. In this equation “A” represents the total area of the hole while “p” is the perimeter of the geometry.

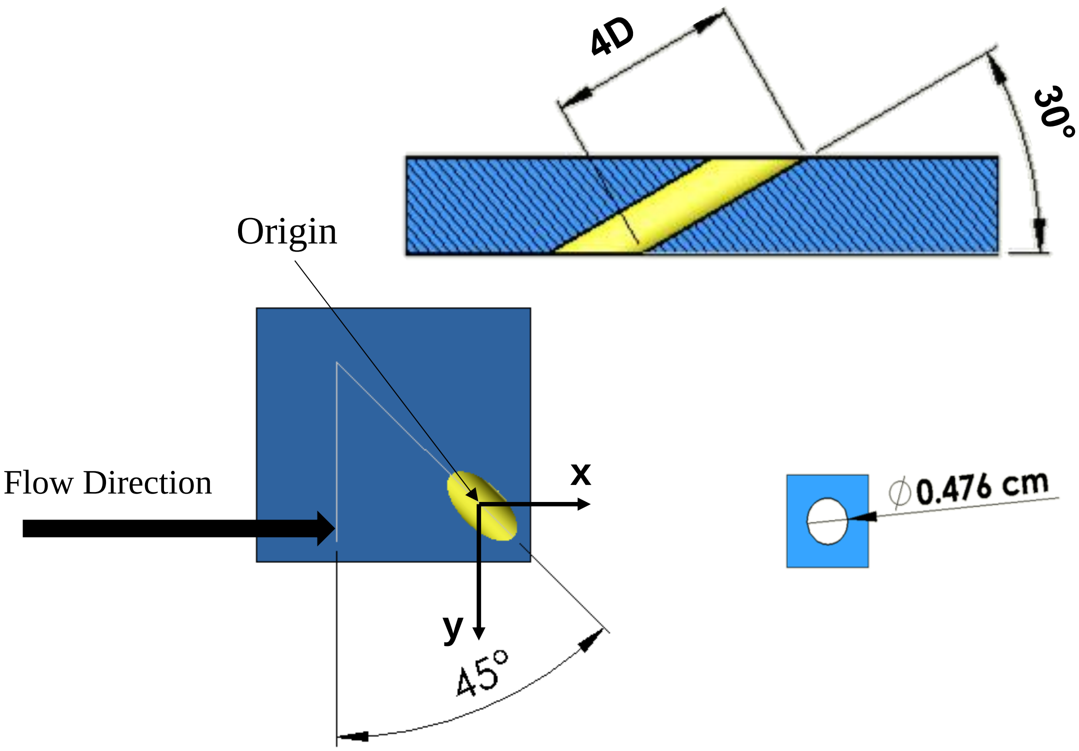

Figure 4.2: Round Hole Geomery

$$D_h = \frac{4A}{p} \tag{4.1}$$

DuckFoot Geometries

Honeywell has created two alternative advanced cooling designs that have also been tested in this experiment. The duckfoot geometries have also been paired with the round and racetrack inlets. A third dumbbell has also been investigated. These duckfoot cooling geometries have been generated from the appearance of a webbed foot similar to

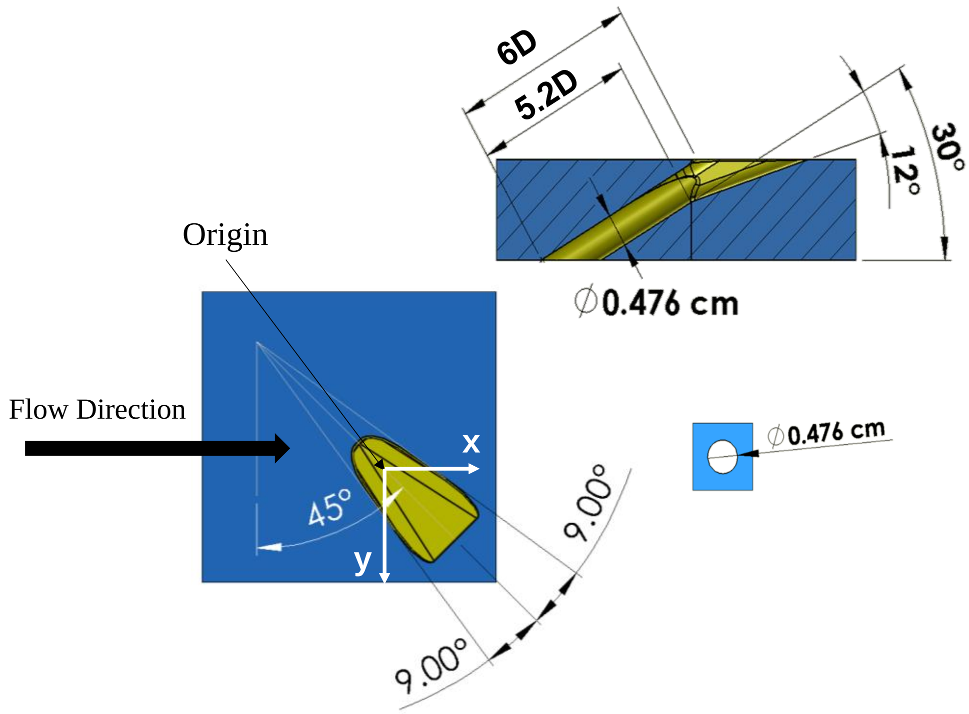

Figure 4.3: Laidback Fanshaped Outlet with a Round Inlet

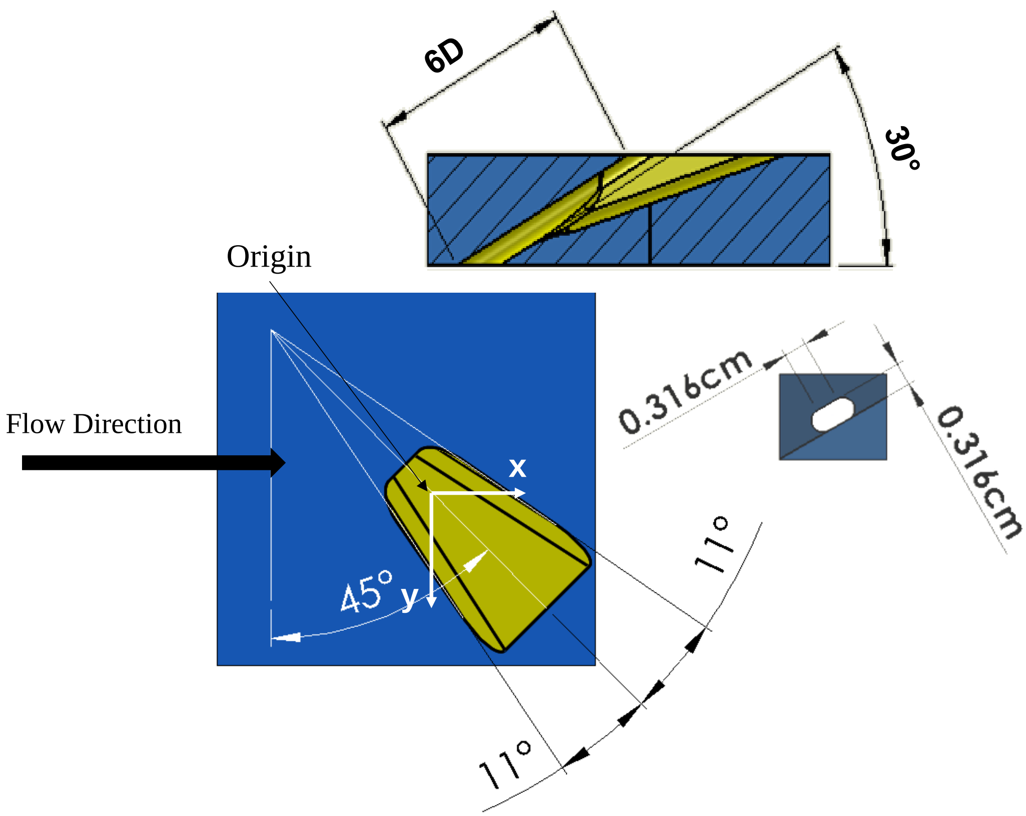

Figure 4.4: Laidback Fanshaped Outlet with a Racetrack Inlet

a duck's foot. The pattern of the hole resembles the "toes" of a duckfoot and provides promising results in film cooling. Two types of duckfoot shapes have been tested, but only one duckfoot has been tested with the three different inlet hole geometries. For the first duckfoot, the round and racetrack inlets have been used and these versions are seen in Figures 4.5 and 4.6. One of the key features of this type of cooling geometry is the size and complexity of the cooling hole. The portion that is open to the surface for the duckfoot outlet is much wider and longer then what was seen for the round and even Honeywell shaped holes.

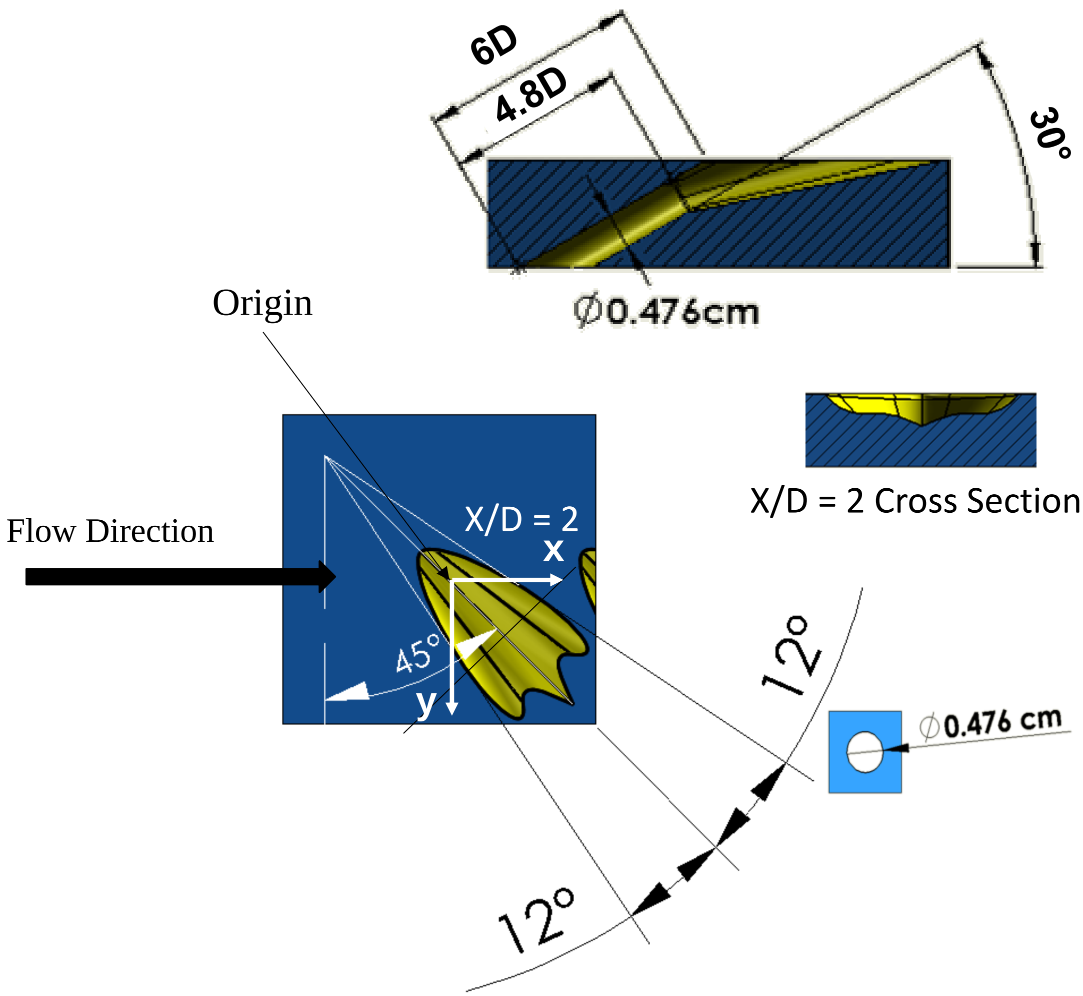

Figure 4.5: Duckfoot Outlet with a Round Inlet

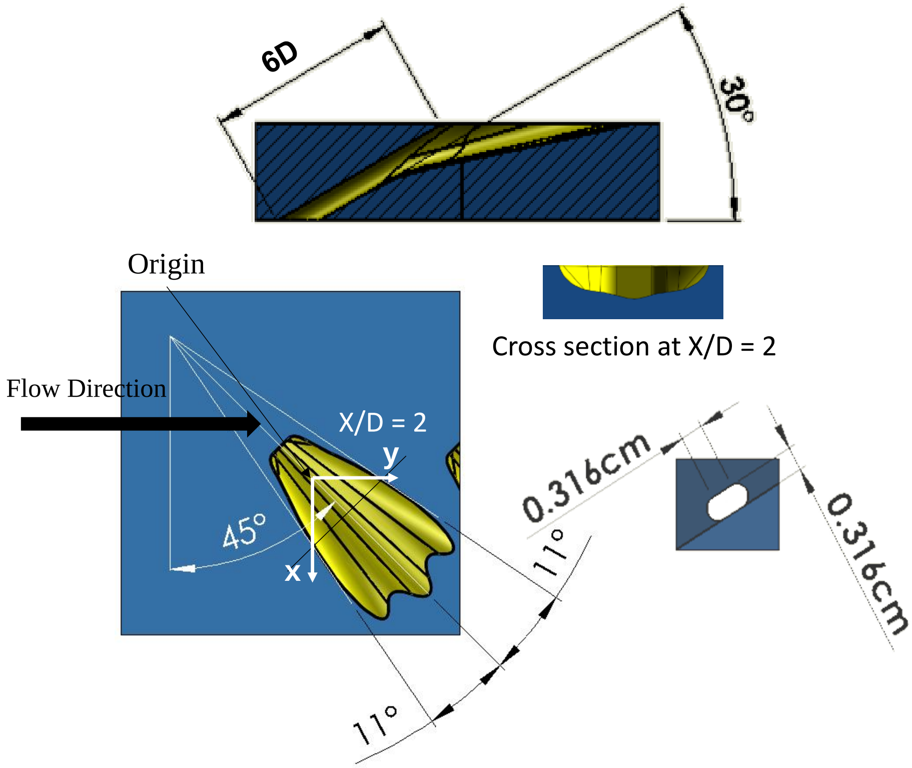

Figure 4.6: Duckfoot Outlet with a Racetrack Inlet

Dumbbell Inlet

The final two geometries have been given the dumbbell (dogbone) shaped inlet. The first duckfoot outlet with a dumbbell inlet is seen in Figure 4.7, plus the variant duckfoot geometry called duckfoot two is shown in Figure 4.8. This new inlet is called a dumbbell inlet and resembles its name namesake. This modification is a further attempt to investigate inlet effects of the cooling effectiveness. Duckfoot one with a round inlet and duckfoot one with a dumbbell inlet are the same geometry with only modifications at the entrance of the hole, yet the shape of these two holes looks noticeably different. These drastic differences have been added to the experiment to further increase the understanding of these cooling effects. In addition to this, the dumbbell inlet version of duckfoot one will also be compared to the altered geometry called duckfoot two which also has been generated with the same dumbbell inlet shape.

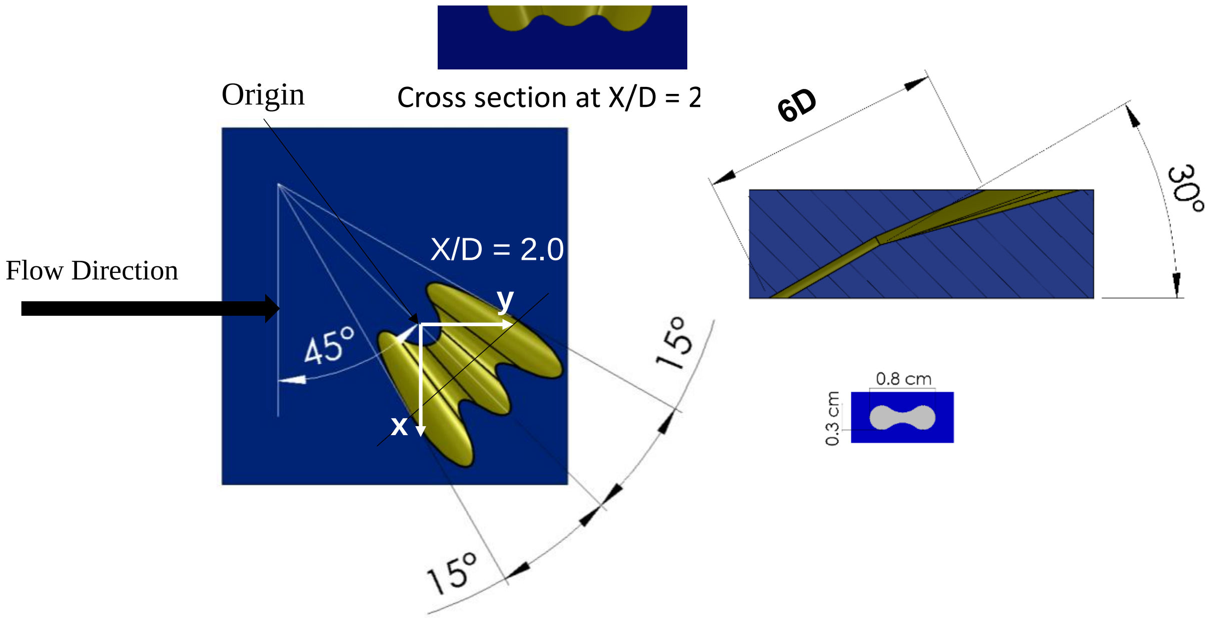

Figure 4.7: Duckfoot Outlet with a Dumbbell Inlet

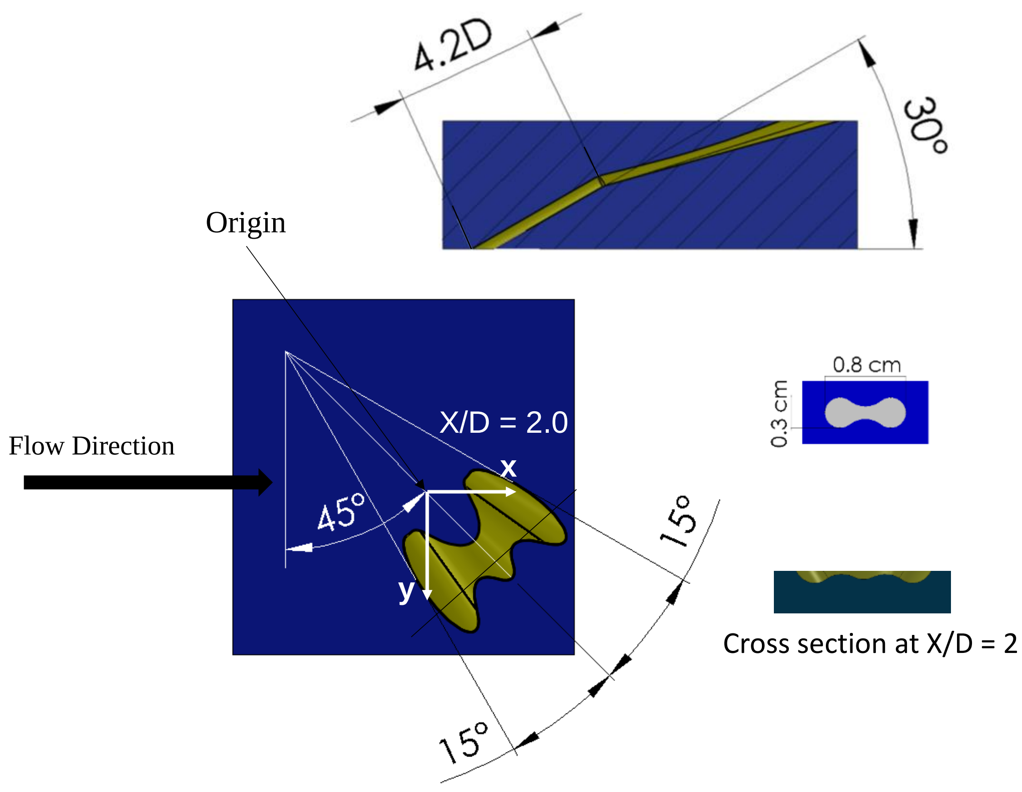

Figure 4.8: Duckfoot Two Outlet with a Dumbbell Inlet

PSP Setup

Only a few basic elements are required to conduct a PSP test. For these experiments, a CCD type camera from Cooke Crop. is used to record the images, this setup can be seen in Figure 4.9. This camera is driven by CamWare camera recording software. UNI263 Pressure Sensitive Paint is applied to all tested surfaces and calibration pieces used for the study. To excite the PSP, a 400 nm wavelength LED light from Innovative Scientific Solutions Inc. was used. When testing with PSP various gases are used as the coolant flow.

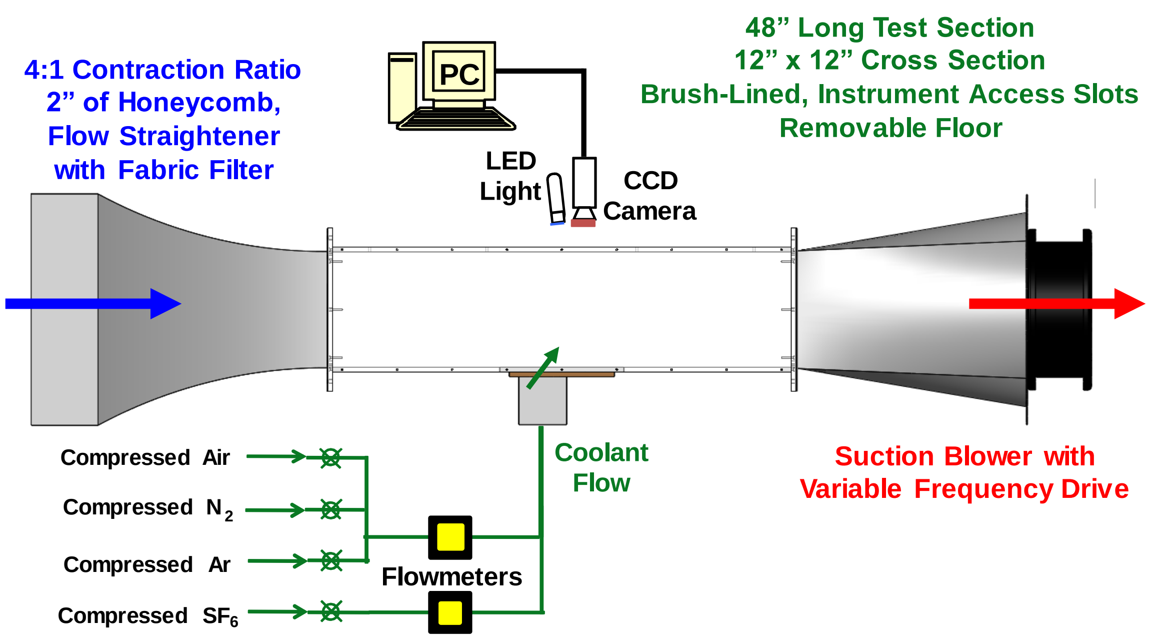

Figure 4.9: Wind Tunnel with PSP Instrumentation

Flow Conditions

The freestream velocity was chosen based on matching flow the conditions used in previous work by Vinton et al. [64]. In those experiments, a freestream velocity of 10 m/s was used. Where the film cooling holes start blowing into the boundary layer, the Reynolds number is approximately 325000. At this Reynolds Number, the boundary layer height is approximately 0.000876 meters where film coolant is blown into the mainstream flow. The 61 cm fan in this experiment was constantly monitored to ensure that the free stream velocity was always matching this condition. While the mainstream velocity in the tunnel always remains constant, the flow conditions from the film cooling geometry do not. Three blowing ratios M = 0.5, 1.0, and 1.5 are used and four density ratios DR = 1.0, 2.0, 3.0, and 4.0 are also used to vary to the tests. These flow conditions more accurately model the operating environment in a gas turbine. The three blowing and four density ratios lead to 12 different momentum flux ratios for each of test. All flow conditions are summarized in the Table 4.1.

Table 4.1: List of All Flow Conditions Used in the Experiment

Density Ratio	I at M = 0.5	I at M = 1.0	I at M = 1.5
1.0	0.25	1.0	2.25
2.0	0.125	0.5	1.125
3.0	0.083	0.33	0.75
4.0	0.0625	0.25	0.5625

CHAPTER FIVE

Compound Angle Effects on Film Cooling Effectiveness

The Pressure Sensitive Paint Technique has been used to investigate the performance of film cooling geometries over a flat surface. In order to determine which cooling geometry benefited the most with the addition of the compound angle, direct comparisons between the different geometries have also been made. These results are presented three different ways: 1) the detailed distributions, which look at the point by point cooling distributions recorded over the whole surface, 2) the laterally averaged effectiveness, which looks at the averaged effectiveness of a specific width at each X/D location, and 3) the overall area averaged effectiveness that averages the effectiveness over a defined physical area on the surface. Both round and advanced laidback fanshaped hole geometries have been investigated. The round hole as well as the laidback fanshaped round inlet, laidback fanshaped racetack inlet, duckfoot round, duckfoot racetrack, duckfoot dumbbell, and duckfoot 2 dumbbell geometries have been evaluated. A variety of flow conditions have been used to evaluate the cooling performance of each geometry. The study covered density ratios from DR = 1.0 to 4.0 and blowing ratios from M = 0.5 to 1.5. The performance of these cooling geometries has previously been outlined in work conducted by Vinton [65]; however, all of the cooling geometries were orientated in the streamwise direction with no compound angle. No alterations to the actual cooling geometries were made between the data from Vinton and this study; the cooling holes have simply been rotated. If the compound angle can increase cooling effectiveness over the surface, then this technique is a simple way to improve the efficiency of cooling layouts in hot sections of the engine and increase overall engine performance. Many studies have been performed pertaining to the round hole and the addition of the compound angle; however, there is far less data on compound angle effects for advanced shaped geometries. Also, the shapes in this study are proprietary, with no published data on these advanced cooling holes. Therefore, this study on the compound angle effects becomes more important. Because of this lack of data, these results will help fill a gap in knowledge for advanced shaped hole cooling effectiveness.

Round Hole Effectiveness Results

Cooling results for the round hole in the streamwise direction are presented in Figure 5.1. Six flow conditions are shown, three plots are at a density ratio of DR = 1.0 and DR = 3.0, with gradually increasing blowing ratios. The regions in front of the cooling hole as well as far to the left and right are red. This indicates a low level of cooling protection over that surface. In actual engine operating conditions, these areas would be very hot, so for the results in this study, areas that are predominantly red are areas that would be considerably hotter than the cooling flow. For the cooling distributions, the areas that are mostly blue and green are receiving a large amount of mainstream protection. This means they are well isolated from the mainstream flow. When operating in an engine, these areas would be considerably cooler than the mainstream flow. Therefore, in this study, blue areas indicate significantly cooler temperatures as compared to the mainstream flow.

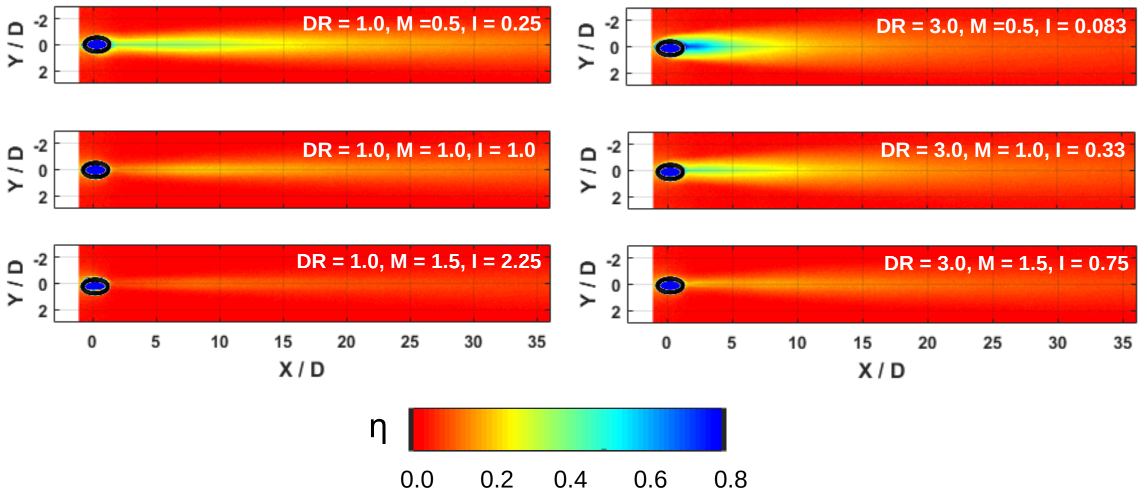

Figure 5.1: Blowing and Density Ratio Effects on the Streamwise, Round Hole

As it is clearly seen for the round hole, when the blowing ratio is increased, the cooling effectiveness is drastically decreased over the surface. This is seen because the flow from a round hole has a high level of momentum compared to the mainstream flow. This means that it can push through the boundary layer and lift off of the surface. As presented in Chapter Two, the flow will separate from the surface and then begin to reattach to the surface after it slows down. These effects are clearly seen in Figure 5.1. The hot sections of a turbine engine do not usually operate at a density ratio of DR = 1.0. Because of this, higher density ratios must also be studied to understand cooling effects at more realistic operating conditions. For the round hole in the streamwise direction, as the density ratio is increased, the cooling results will also be altered. Also seen in Figure 5.1, the cooling results at a density ratio of DR = 3.0 show these effects. As the density of the flow is increased the momentum of the flow coming from the round hole is reduced. The momentum of the cooling flow is reduced because the cooling flow velocity is reduced by three times when the cooling flow density is increased by three times. This slower heavier cooling flow is able to stay attached to the surface much more effectively at all three blowing ratios. These effects are seen in the density ratio of DR = 3.0. The flow has sunk onto the surface near the trailing edge of the hole, reducing the rate at which the coolant mixes with the mainstream and increasing the lateral and centerline effectiveness near the hole This results in an overall increase in area averaged cooling over the surface.

Some negative effects are seen when the density ratio is increased. When more cooling flow is used near the trialing edge of the hole, less flow is available to be used further downstream of the hole. At higher X/D locations the cooling flow lacks sufficient momentum to be able to resist the mainstream flow and the cooling effectiveness is reduced quicker than was seen at lower density ratios. This results in reduced centerline and laterally averaged cooling effectiveness far from the hole.

With the addition of the compound angle to the round hole, different cooling effectiveness distributions are seen. A compound angle of $\beta = 45°$ has shown to increase the cooling effectiveness. As the cooling flow exits the hole with a compound angle, the velocity in the streamwise direction is reduced. Also, the compound angle round hole is pushing this flow across the surface instead of straight down it. This allows it to act similarly to an advanced shape hole in that the cooling flow is spread out and slowed down before it reaches the surface, allowing for greater cooling effectiveness. Figure 5.2 shows a direct comparison of detailed cooling distributions at a density ratio of DR = 1.0; the round hole orientated streamwise to the flow versus a compound angle. It is seen clearly that at low X/D locations the compound angle outperforms the straight round hole, but further from the cooling geometry, the flow is blown off the surface and offers similar protection to the streamwise round hole.

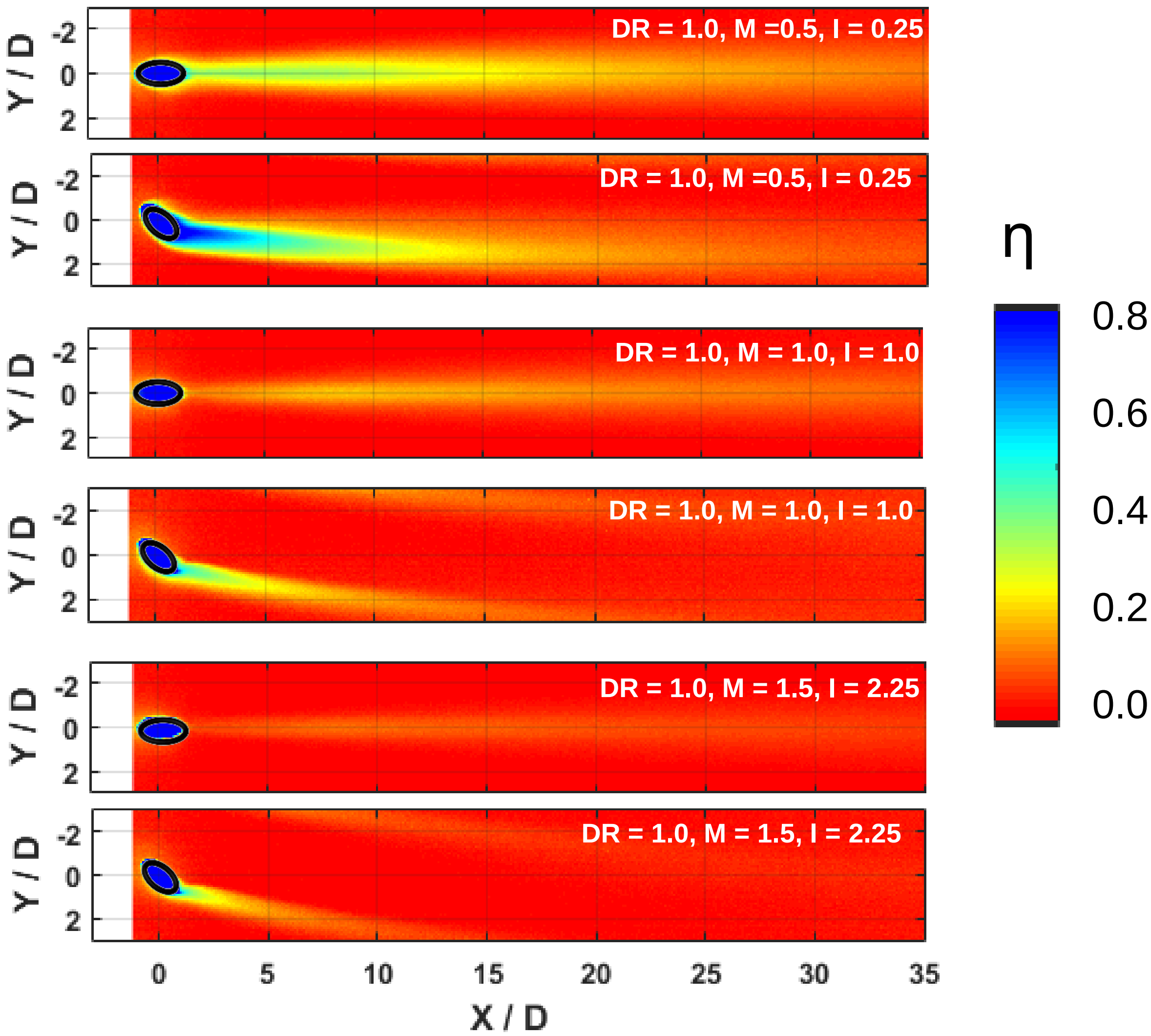

Figure 5.2: Detailed Round Hole with Streamwise and Compound Orientations at DR = 1.0

Looking at all of the detailed distributions for the compound angle round hole in Figure 5.3, the full effects of the flow conditions become apparent. When the holes are streamwise to the flow, their cooling performance is very dependent on the blowing ratio, the blowing ratio also seems to be the dominating flow condition for the compound angle round hole tests as well. At each of the four density ratios, as the blowing ratio is increased the cooling effectiveness is significantly altered. An additional density effect is also seen with both streamwise and compound angle holes, as the density ratio is increased the coolant sinks to the surface more near the trailing edge of the hole. This trend is observed because the coolant is heavier than the mainstream flow and as the momentum is reduced the flow is not blown off the surface as severely. This liftoff reduces the downstream coverage of the coolant and the total cooling effectiveness of the cooling geometry. The momentum flux is a function of both the density and blowing ratios. Two separate flow conditions yield approximately the same momentum flux is ratio of I = 0.5 and 0.25. Both of these times where the flow momentum is similar it turns out the overall averaged cooling effectiveness for the surface is approximately the same as well. Looking at the DR = 1, M = 0.5 and DR = 4, M = 1.0 case, as well as the DR = 2, M = 1.0 and DR = 4, M = 1.5 cases in Figure 5.5, the results show similar levels of overall cooling.

The direct quantitative comparison between the two orientations is seen with the laterally averaged cooling effectiveness plots in Figure 5.4. This lateral average occurs the same linear distance of 2.54 cm for every case tested. At every X/D downstream of the inlet, the average effectiveness across the surface in the Y/D direction is taken. This average only includes Y/D values that are included in the 2.54 cm range of the tested surface. The compound angle holes show a higher level of cooling near the trailing edge of the hole just as expected; however, further downstream the two sets of data tend to merge into each other as cooling levels become very similar. This trend then changes as the density ratio increases, both cooling holes start to show the same gradual decrease in effectiveness and look almost identical. At the higher density ratios the flow has lost a lot of momentum. As the flow enters the surface from a round hole, the low momentum

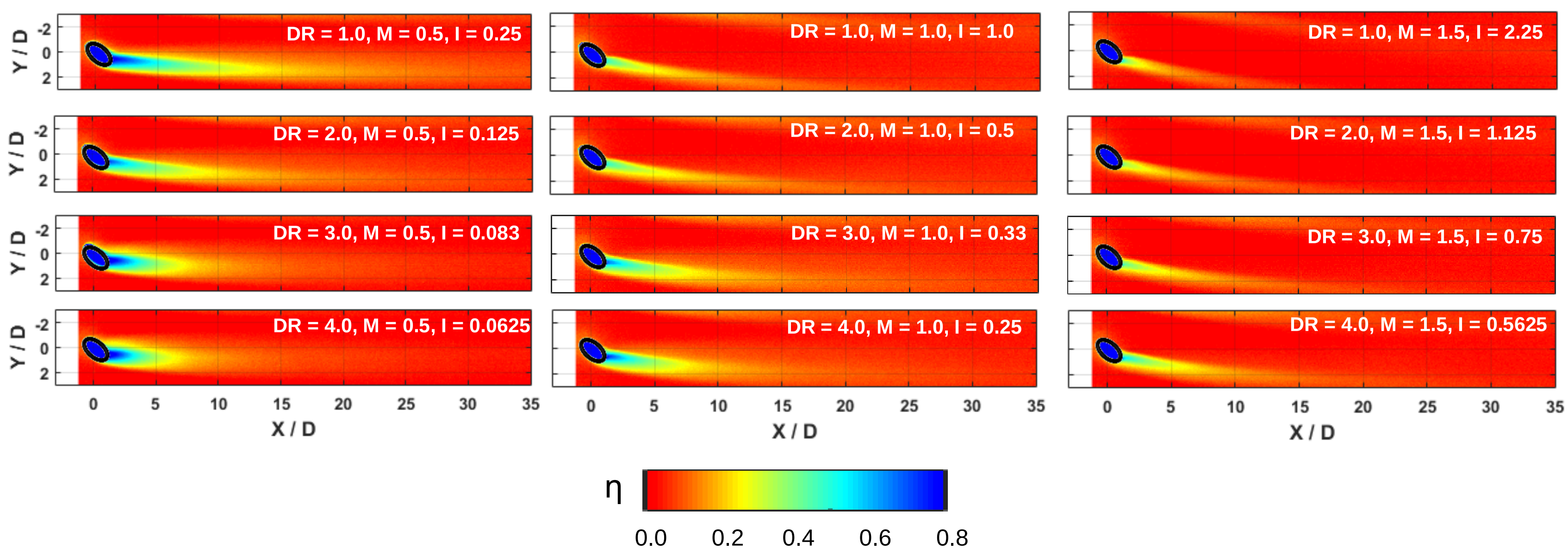

Figure 5.3: Detailed Film Cooling Effectiveness Distributions for a Round Outlet with a Round Inlet

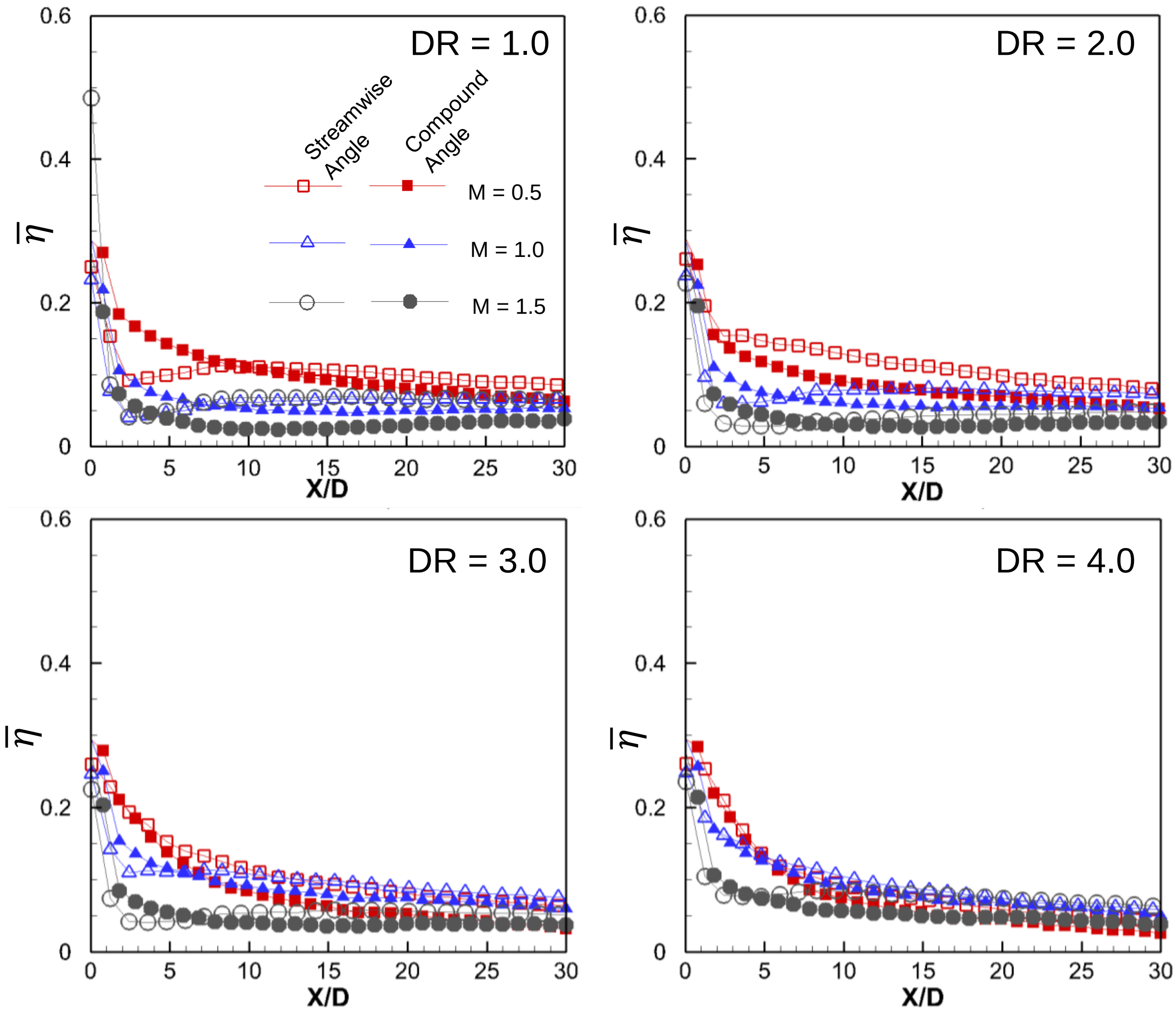

Figure 5.4: Laterally Averaged Cooling Effectiveness for the Round Hole

nullifies the effect of the compound angle causing the flow trends and characteristics to become very similar to that of the streamwise angle.

Finally, while looking at the averaged cooling effectiveness in Figure 5.5, it becomes clear the round hole has provided very similar levels of cooling performance regardless of the compound angle. A physical area of 2.54 cm by 9.5 cm is used in all of the area averaged calculations. The momentum flux is plotted with the overall average because it takes into account the changing density of the cooling flow. As the density of the flow is increased, there is a definite reduction in momentum even with the blowing

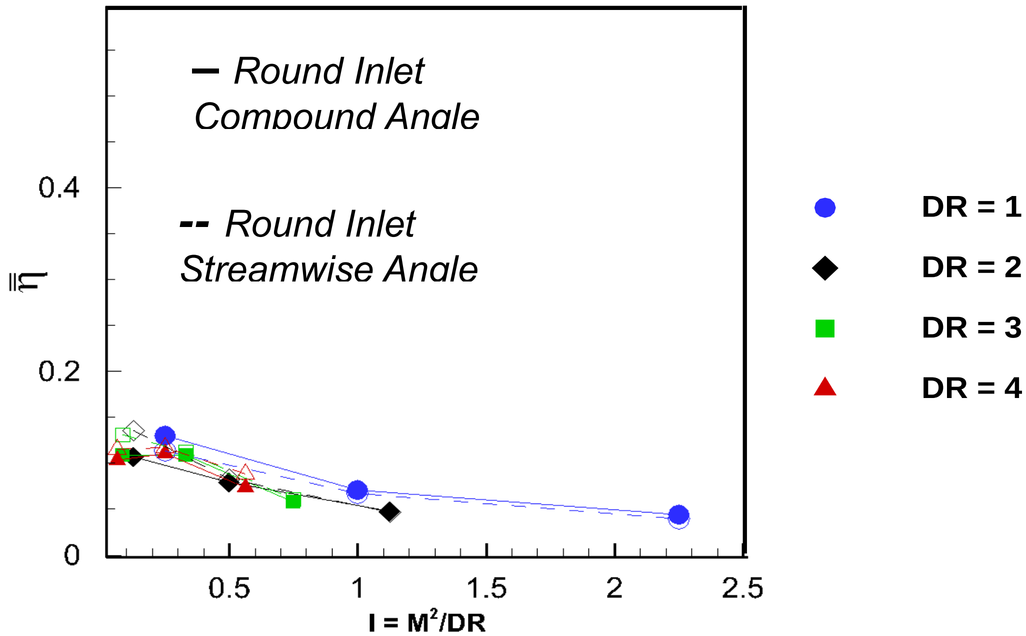

Figure 5.5: Round Hole Overall Area Averaged Cooling Effectiveness

ratio remaining constant. This helps to explain the changes in cooling performance that are seen with changing density ratio. The momentum flux is a better correlation for the overall average. If only the blowing ratio is plotted with the effectiveness, four distinctly different lines would be seen; this would be easy to compare with other data or take into account density ratio effects. The momentum flux takes this into account. When this happens the data will collapse on top of each other. This makes a much more consistent set of data. As seen on the detailed distributions, while the momentum of the cooling flow is increased, the overall cooling effectiveness is decreasing. High flow momentum at large blowing ratios leads to most of the coolant being blown off the surface. The compound angle does reduce these effects near the trailing edge of the hole, but overall it does not provide significant increases in cooling over the entire surface. This is a decreasing trend for film cooling geometries as engine designers tend to run engines at high blowing ratios.

Laidback Fanshape Effects

Looking only at the more traditional laidback fanshaped holes, the advanced shapes are more efficient than the round hole. The literature review in Chapter Two showed that advanced cooling shapes were able to spread out the coolant laterally and slow it down before it reached the surface. This combination results in the elevated film cooling effectiveness for these shapes. The laidback, fanshaped outlet with round inlet shows much higher cooling than the round hole does; it follows opposite trends to those seen with the round shape. In Figure 5.6 the direct comparison between the streamwise and compound angles were made. A first initial difference between the streamwise and compound angle is the flow exiting the side of the hole on the compound angle case at low blowing ratios. This is observed because the flow lacks sufficient momentum at high density ratios to follow the outlet shape onto the surface.

Density and blowing ratio effects are seen in Figure 5.7. Just as with the round hole geometry, the compound angle, laidback fanshape outlet with a round inlet begins with higher cooling effectiveness at locations near the trailing edge of the cooling geometry. Just as with the round holes, the addition of the compound angle is further slowing the flow before it exits to the surface. Further downstream from the cooling geometry the effectiveness begins to resemble the streamwise cooling results as the flow mixes with the mainstream at the same rate as the streamwise flow. With the increase in lateral coolant spread, the density and blowing ratio now have opposite effects on cooling. As blowing ratio increases, the cooling now increases over the surface, while an increase of density ratio, slows the flow too much and gradually decreases cooling.

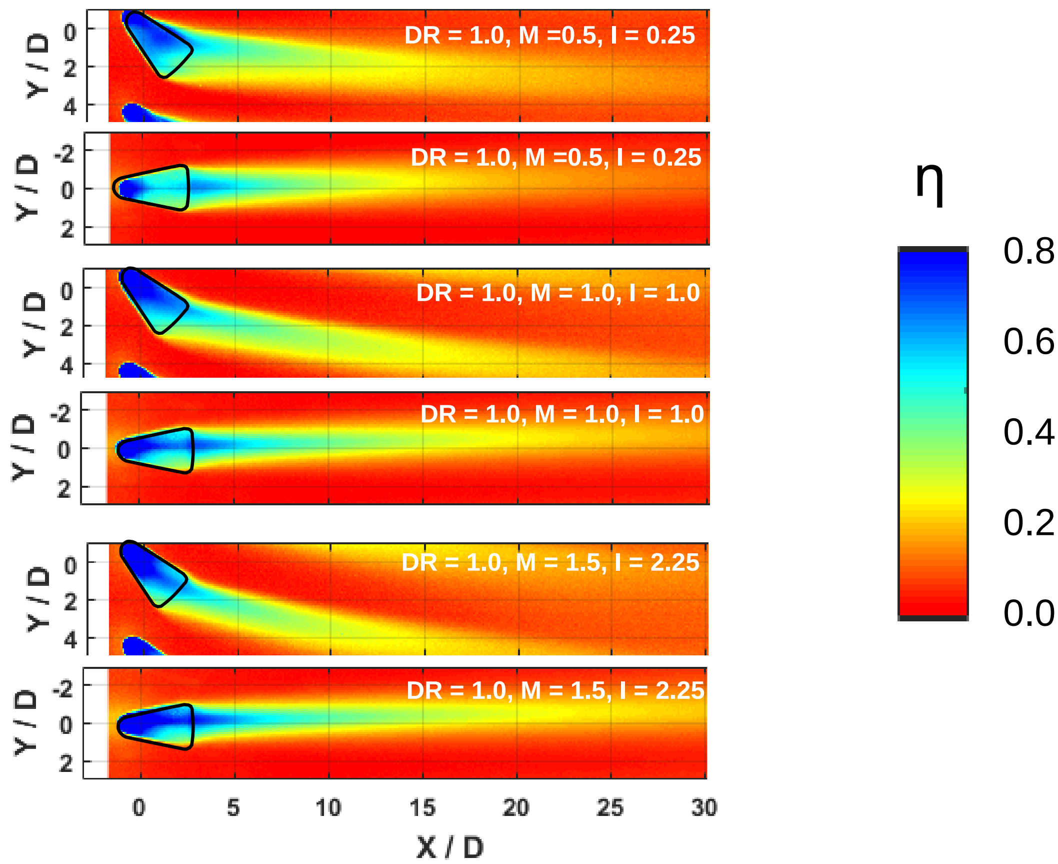

Figure 5.6: The Laidback Fanshape Outlet with a Round Inlet (Streamwise vs Compound Orientation Comparison)

Because the momentum is being reduced so much, the spread coolant is mixed into the mainstream quicker at the higher density ratios.

As the blowing ratio is increased, for any density ratio, the overall effectiveness is increased. This is the opposite trend that was observed for the round hole. When the density ratio is increased for these advanced shapes the overall effectiveness is decreased, as opposed to the round hole results which showed elevated cooling performance at higher density ratios. When the blowing ratio is increased the cooling effectiveness increases, opposite to the round hole trends. The advanced shape outlet is able to keep the coolant on the surface and provide much higher cooling effectiveness over the round hole geometry. The laterally averaged effectiveness in Figure 5.8 also gives a quantitative confirmation of these results as well. The averaged results for the first laidback fanshape outlet with a round inlet show the opposite trends to the area averaged results of the round hole. As the flow conditions change in Figure 5.9 for the overall area, the cooling coverage does not change significantly. This is an advantageous results for advanced shaped film cooling. Engine designers tend to operate engines at high blowing ratios. In the event of a failure which resulted in a reduction or loss of cooling air, engine designers can still count on advanced cooling geometries protecting the components. With the addition of the compound angle, the streamwise velocity and momentum are further reduced inside of the hole before it reaches the surface. This further increases the cooling flow's ability the stay attached to the surface. These effects are especially seen near the trailing edge of this cooling geometry.

Laidback Fanshape Outlet With Racetrack Inlet

This version of the laidback fanshape is fundamentally the same as the previous version tested. The only difference between the two shapes is the inlet of the cooling hole. Figures 5.10 and 5.11 show the detailed cooling distributions and laterally averaged plots for all the flow cases. The laidback fanshape outlet with a racetrack inlet shows the same overall trends as the laidback fanshape outlet round inlet; however, the overall cooling performance for the racetrack inlet is higher than what was seen for all but one of the cases of shaped outlet with a round inlet. The DR = 4, M = 0.5 case shows an actual reduction in cooling under the compound version, as the cooling flow lacks enough momentum to make it out of the cooling geometry and is mixed into the mainstream very

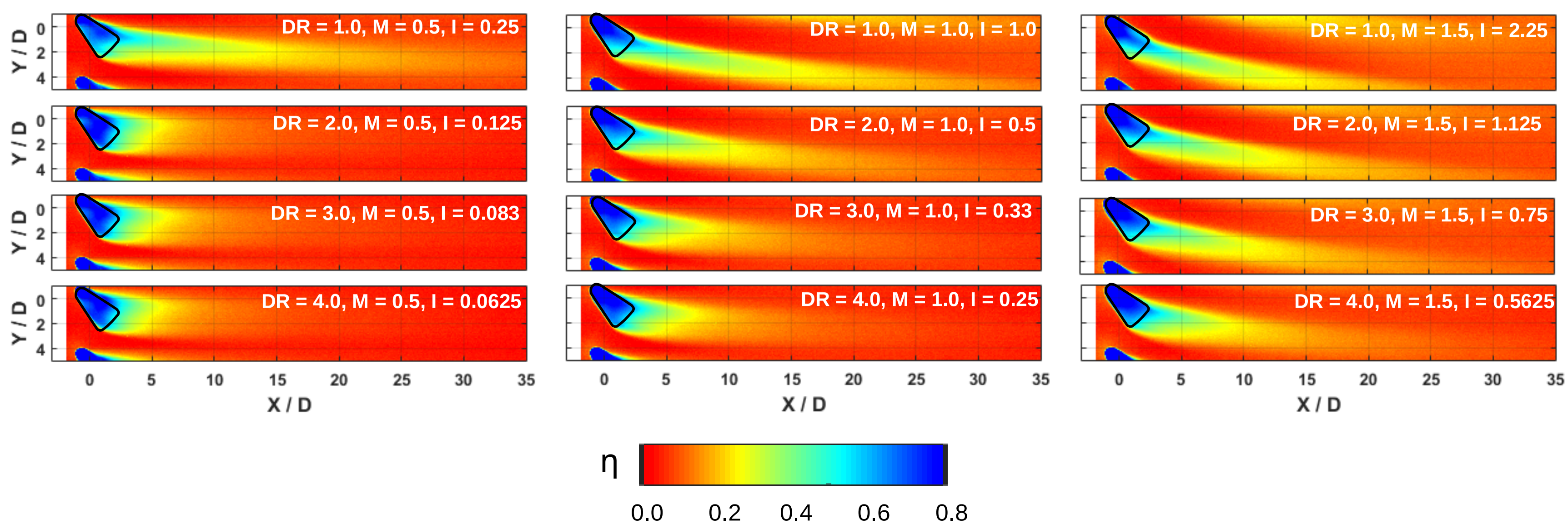

Figure 5.7: Detailed Film Cooling Effectiveness Distributions for a Laidback Fanshape Outlet with a Round Inlet

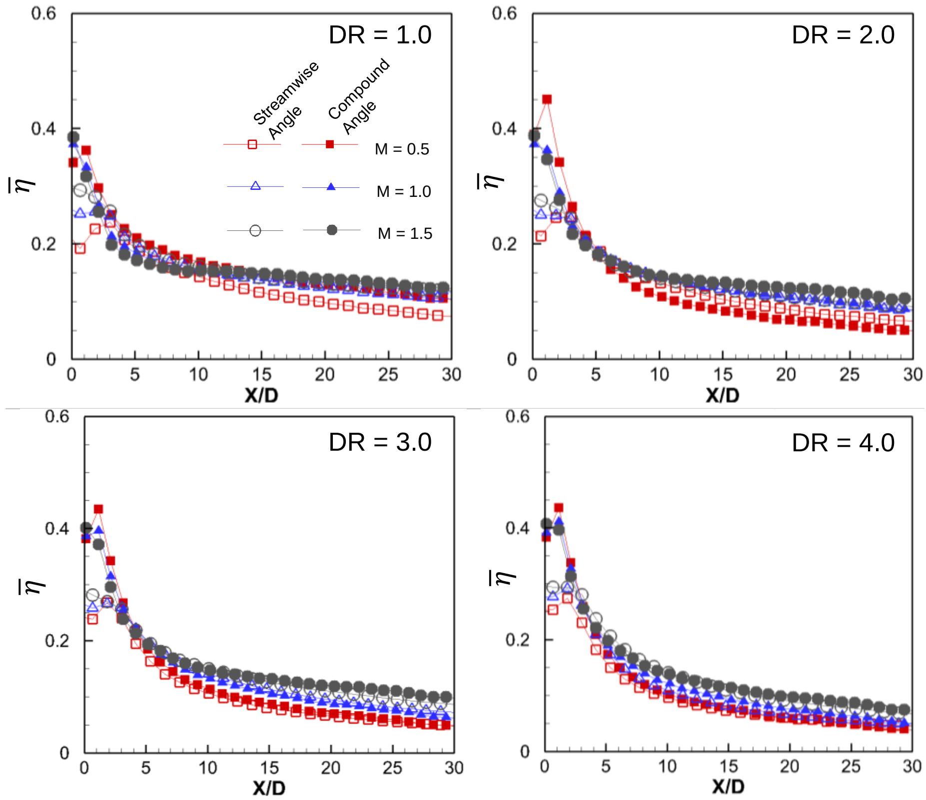

Figure 5.8: Laterally Averaged Film cooling Effectiveness for the Laidback Fanshaped Outlet with a round Inlet

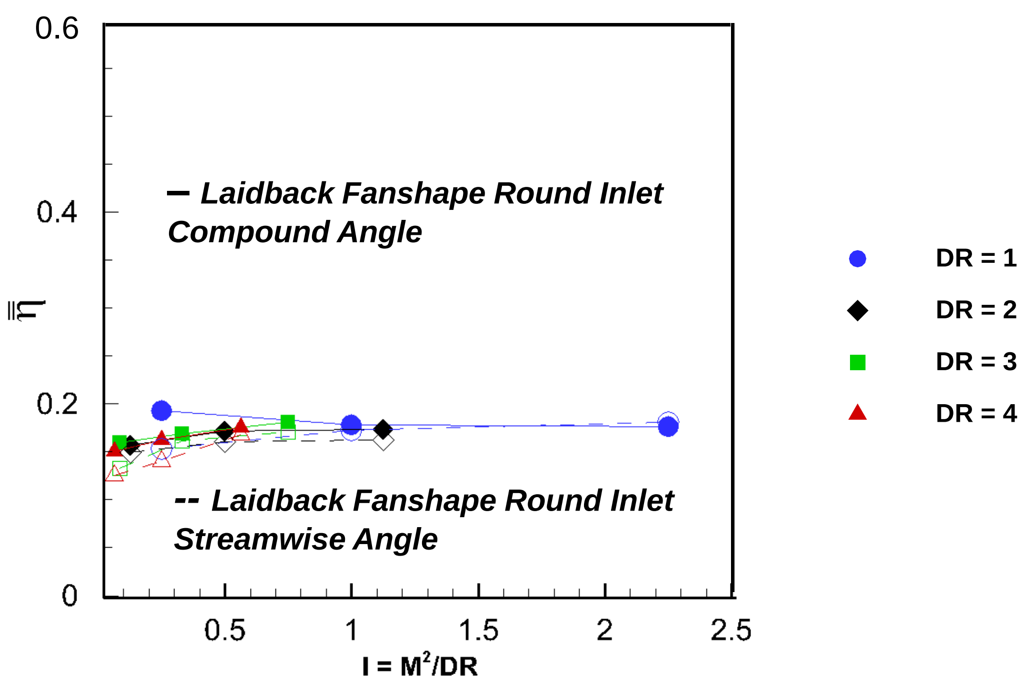

Figu aidback Fanshaped
Outlet with a Round Inlet

rapidly. The racetrack inlet has an additive effect on the lateral spread of the coolant. This inlet is at a 2:1 size ratio, so it is twice as wide as it is tall. This inlet also has an effect on the outlet shape as well; it results in a wider and deeper film cooling hole. This means that the flow is slowed down more than with the laidback fanshape with a round inlet, this leads to an increased cooling effectiveness for most cases. Several flow effects are seen at different sets of flow conditions. The mainstream flow is forcing the coolant to one side of the cooling hole before it reaches the surface. Because of this, a non-uniform flow distribution over the surface is observed. Specifically, at the lowest density and blowing ratio, the split in the flow is the most pronounced. With this flow condition, the coolant is not under any density effects to keep it attached to surface. Also, the flow lacks sufficient momentum to make the turn, the compound angle is trying to add to the cooling flow effectiveness. The coolant is spread out more with the outlet, but the similar density flow does not have sufficient momentum to flow the direction of the outlet geometry. The high density, low blowing ratio cases also show similar trends between the streamwise and compound angles. In both hole orientations, the coolant is not able to leave the hole geometry on the surface and cooling effectiveness is reduced. Looking at Figure 5.11, the density ratio of DR = 3.0 shows very equivalent cooling performance while the DR = 4 actually shows a reduction in performance with the compound angle. The cooling flow shows to barely make it out of the cooling holes before it is mixed into the mainstream. This slow, high density flow also lacks sufficient momentum to resist mixing into the boundary layer and then off the surface, rapidly reducing cooling effectiveness.

The overall area average in Figure 5.12 and the laterally averaged results show that the compound angle is starting to have more an effect over the entire surface instead of just at the trailing edge of the geometry. For all but two flow conditions the area averaged effectiveness is showing elevated cooling levels over the streamwise version of the laidback fanshape outlet with a racetrack inlet. This cooling geometry begins to get into specific flow conditions where the flow does not have enough momentum to resist the boundary layer and is carried away by the mainstream flow. This leads to lower cooling levels for two specific flow conditions at extremely low momentum flux ratios below $I = 0.1$. When looking at momentum flux values over this value, even at high density ratios the cooling flow could reach the surface easier and had a higher streamwise velocity when it reached the surface. It was able to more effectively resist the mainstream flow and show higher cooling over the averaged surface. For all other cases, the compound angle showed improved cooling levels over the surface for the laidback fanshaped outlet with a racetrack inlet.

Duckfoot Cooling Geometries

The duckfoot geometries look vastly different than the laidback fanshape geometries; however, they are still considered to be advanced, laidback fanshapes. The main difference between the tested laidback fanshape and duckfoot is three “channels” at the outlet of the geometry which are there to guide to the cooling flow out laterally from the inlet. The duckfoot outlets also are designed to be efficient at cooling the surface under many flow conditions. With the addition of the compound angle, the duckfoot outlet shape is able to disperse and spread the cooling flow even more efficiently. The duckfoot outlet combined with the compound angle shows increased cooling at all X/D locations. Near the trailing edge of the outlet, the effects are much more substantial.

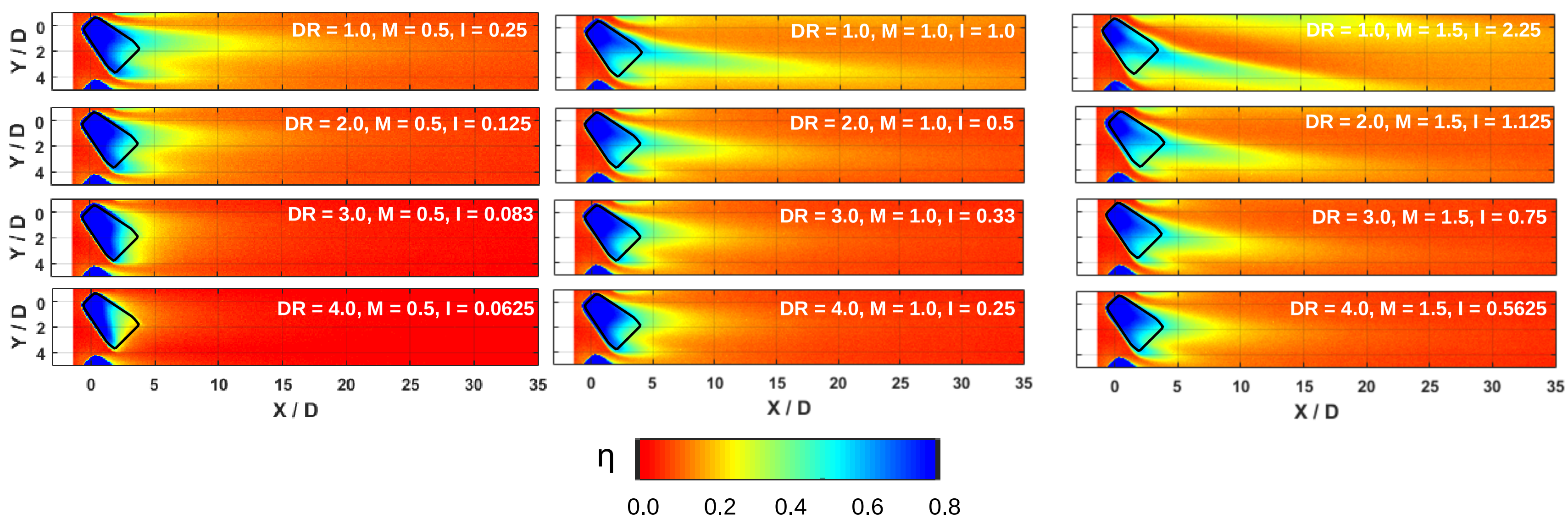

Figure 5.10: Detailed Film Cooling Effectiveness Distributions for a Laidback Fanshape Outlet with a Racetrack Inlet

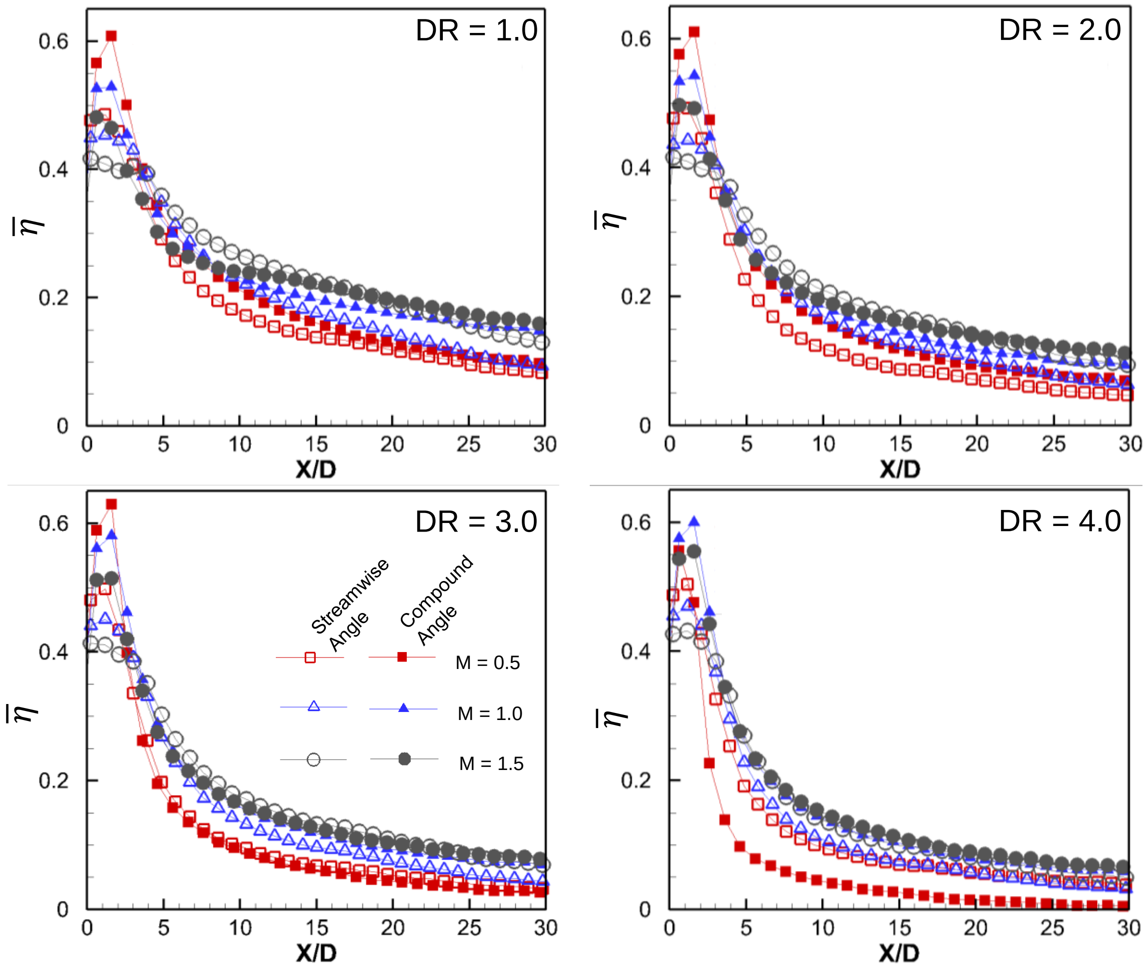

Figure 5.11: Laterally Averaged Film Cooling Effectiveness for the Laidback Fanshaped Outlet with a Racetrack Inlet

The compound angle duckfoot is able to slow the momentum of the flow even more, but the cooling flow is still fast enough that it can resist the effects of the boundary layer. Figure 5.13 shows the detailed distribution of cooling effectiveness for all the flow cases. The high levels of trailing edge cooling are apparent for all cases of the duckfoot outlet with a round inlet. Also because the coolant is spread out so efficiently across the surface, it is mixed into the boundary layer slower than for the streamwise orientated duckfoot outlet with a round inlet hole. With the round inlet, the cooling flow is starting out in the middle of the outlet, it is then not able to take full advantage of the advanced shaped

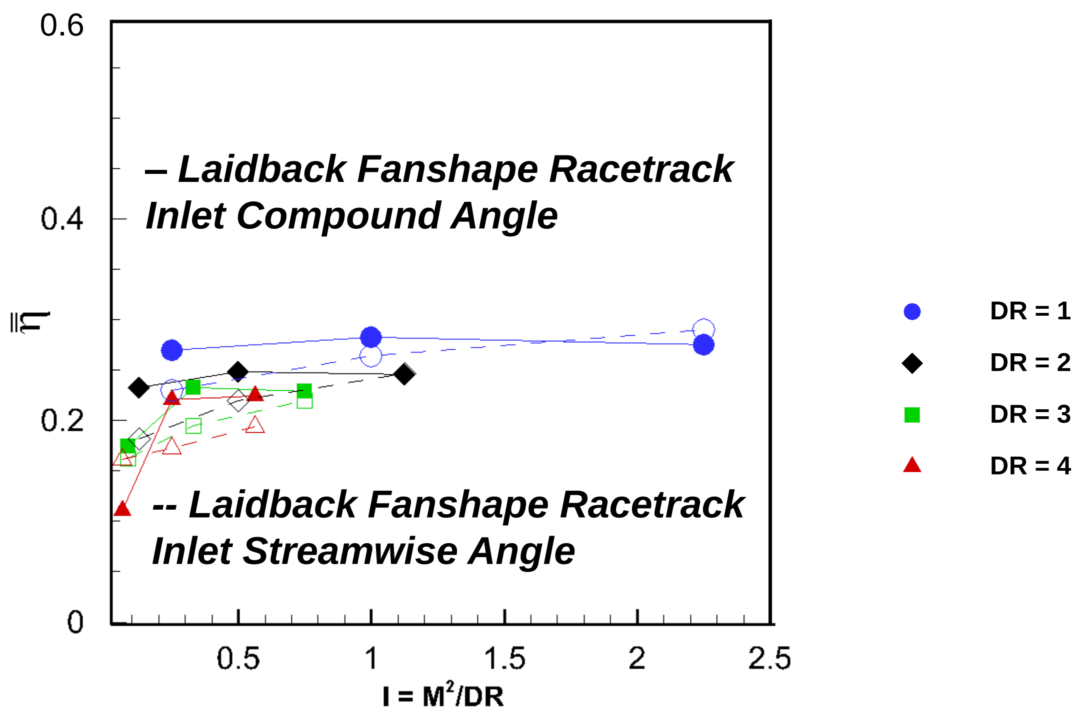

Figure 5.12: Area Averaged Film Cooling Effectiveness for the Laidback Fanshaped Outlet with a Racetrack Inlet

duckfoot outlet. Because of this, the flow splits in two at the trailing edge of the geometry. The mainstream pushes more of the coolant to one side of the hole before it exits to the surface, which leads to the unbalanced distribution on the coolant. However, since some coolant does remain in the "channels" of the duckfoot, the coolant is spread out more, increasing the lateral and overall effectiveness of the geometry.

The lateral average plots in Figure 5.14 show that the duckfoot outlet with a round inlet is the first compound angle cooling geometry that shows improvement in cooling over all of the downstream locations. These positive effects are seen in all of the density ratios. As well, the trailing edge of the cooling geometries also shows the highest levels of cooling effectiveness increase. The overall area averaged plot in Figure 5.15 also shows that the addition of the compound angle has increased the cooling effectiveness at all flow conditions. Just as the laidback fanshape shape outlet, the duckfoot shape cooling effectiveness is very insensitive to blowing ratio changes at each density ratio. With similar trends as the previous advanced shapes tested, this shape sees a gradual drop in cooling effectiveness are the density ratio increases. This is a result of the cooling flow momentum being low far downstream. The duckfoot outlet with a round inlet is able to do something the previous geometries could not. The cooling effectiveness of the compound angle at a density ratio of DR = 3.0 is the same as the streamwise orientation effectiveness at a DR = 1.0. This is a huge improvement as, once again, actual turbine engines at density ratios closer to DR = 3.0 and up.

Duckfoot Racetrack Inlet

Just like for the laidback fanshape, the racetrack inlet also provides further enhanced cooling effects for the duckfoot outlet geometry. This combination matches an inlet that is very good at spreading out the coolant flow with an outlet designed to also spread coolant flow. The addition of the compound angle further increases these cooling effects across the surface. The detailed effectiveness plots show how the cooling holes cover almost all of the downstream surface with the compound angle. At a density ratio of DR = 1.0 there are no red areas anywhere downstream of the cooling hole at any of the blowing ratios. The new orientation for this geometry produces much higher levels of cooling compared to the streamwise version. This is confirmed with detailed distributions and laterally averaged plots seen in Figure 5.16 and 5.17, respectively. As with the laidback fanshape hole, the racetrack inlet has already started to spread the coolant before it reaches the outlet geometry. This helps cooling gases stay inside the cooling geometry longer before they flow onto the surface. Now that the cooling flow is staying in the cooling holes longer, it exits onto the surface more evenly, increasing cooling effectiveness. At low density ratios these effects are obvious; however, under high density and low blowing ratio flow conditions a drop in effectiveness can be seen from the compound angle holes. This drop is an addition from the gradual reduction in effectiveness that is seen in all advanced shaped cooling holes. The compound angle outperforms the streamwise orientation by so much because of how well the flow is taking advantage of the advanced outlet. The duckfoot outlet with a compound angle has a larger lateral area over the surface, since the coolant is staying the channels until the trailing edge more coolant is being spread out, increasing cooling efficiency.

Just as seen on the duckfoot outlet with a round inlet, the racetrack inlet version also provides elevated levels of cooling at all locations downstream of the hole. The racetrack inlet, however, shows a larger improvement over the streamwise version than the duckfoot outlet with a round inlet version. The duckfoot outlet with a racetrack inlet shows the largest gains of cooling effectiveness with the addition of the compound angle. The overall area average of the racetrack duckfoot shows that even the highest density ratio of DR = 4.0 of the compound angle flow, provides an equal amount of cooling as the DR = 1.0 for the streamwise flow. These effects are seen if Figure 5.18. It is consistently observed that as density ratio is increased the overall effectiveness for an advanced shaped hole will trend to decrease. This still effects the compound angle version, but the compound angle starts at cooling levels high enough that the lowest cooling values of the compound angle still match the highest seen for the streamwise cases. The perfectly correlated data set will show all four density ratios collapsing onto each other and forming a common curve. The data collected for the duckfoot outlet with a

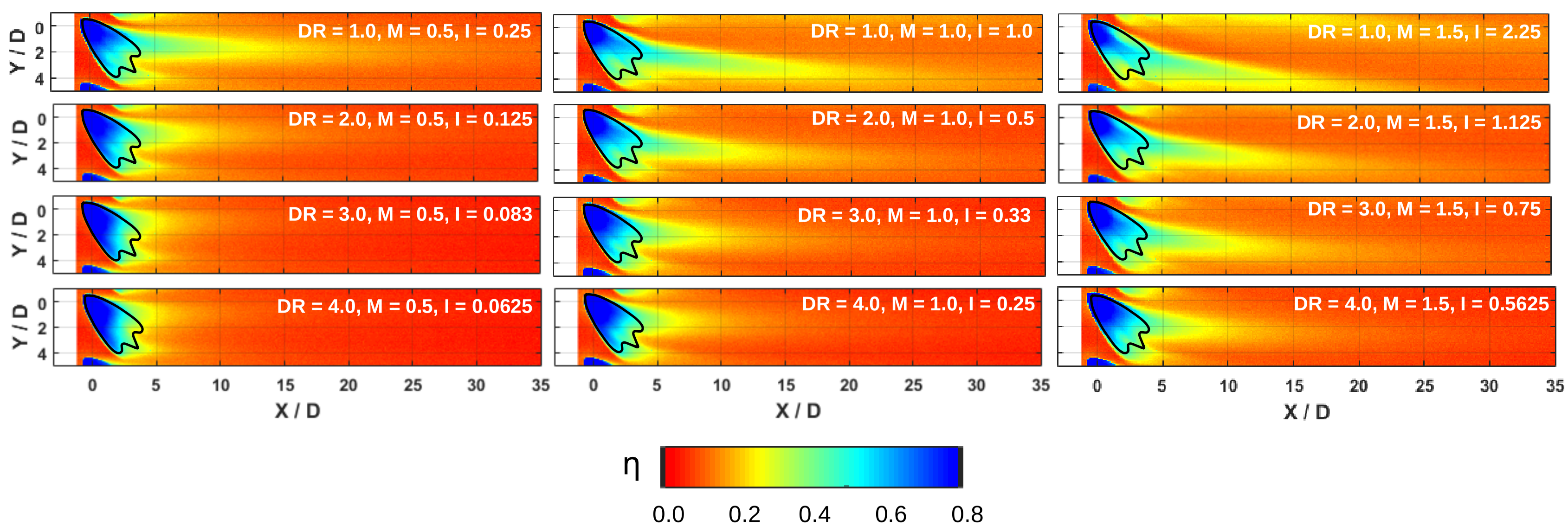

Figure 5.13: Detailed Film Cooling Effectiveness Distributions for a Duckfoot Outlet with a Round Inlet

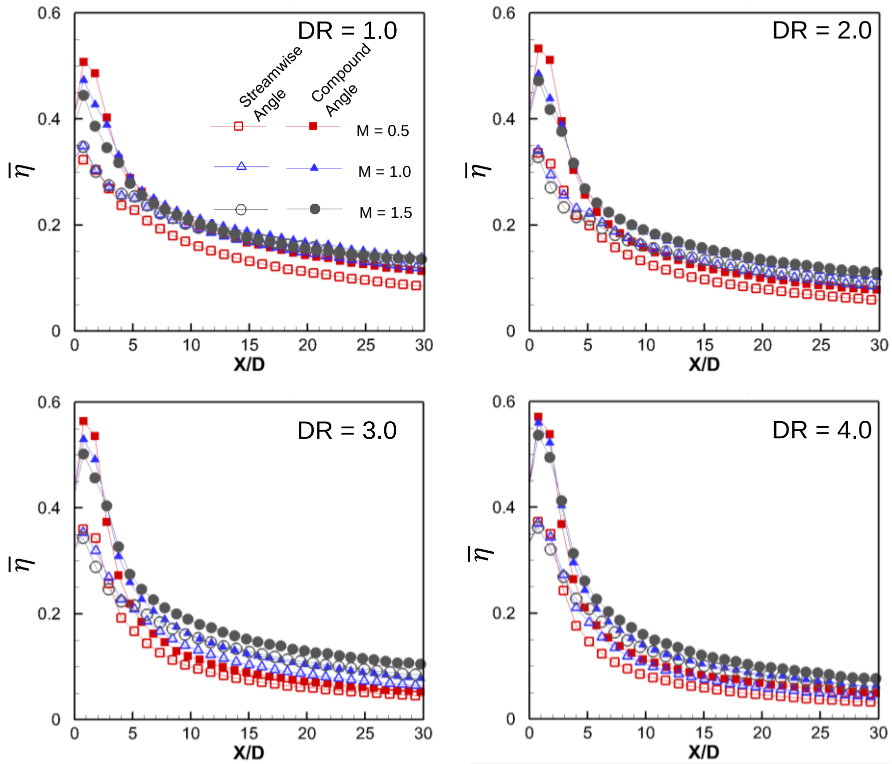

Figure 5.14: Laterally Averaged Film cooling Effectiveness for the Duckfoot Outlet with a Round Inlet

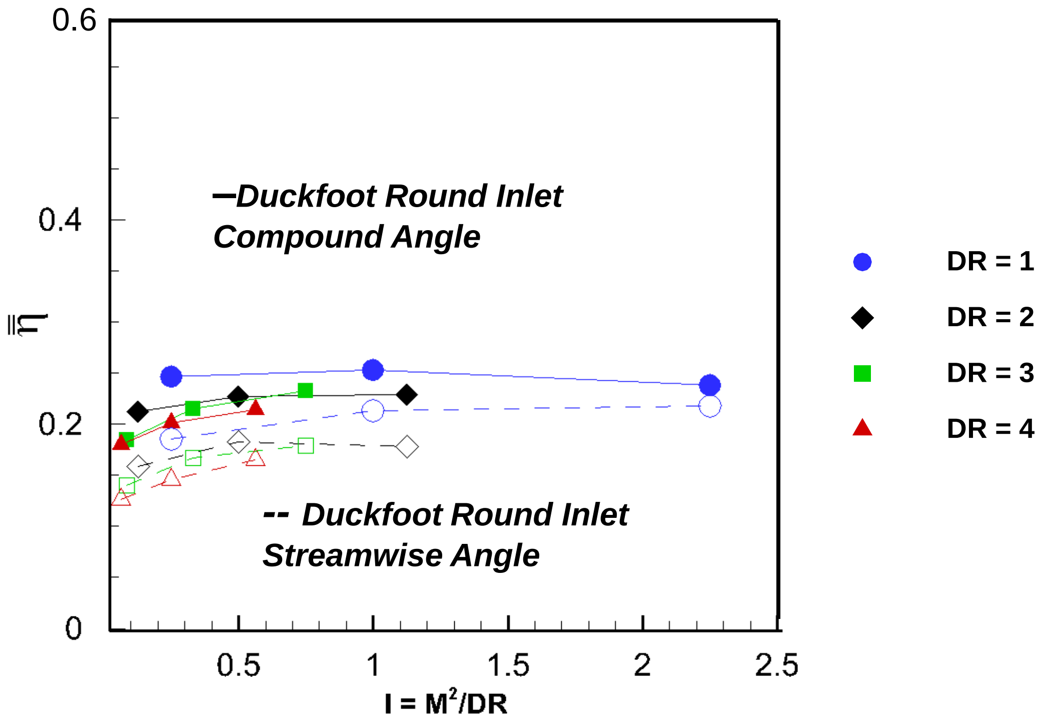

Figure 5.15: Area Averaged Film Cooling Effectiveness for the Duckfoot Outlet with a Round Inlet

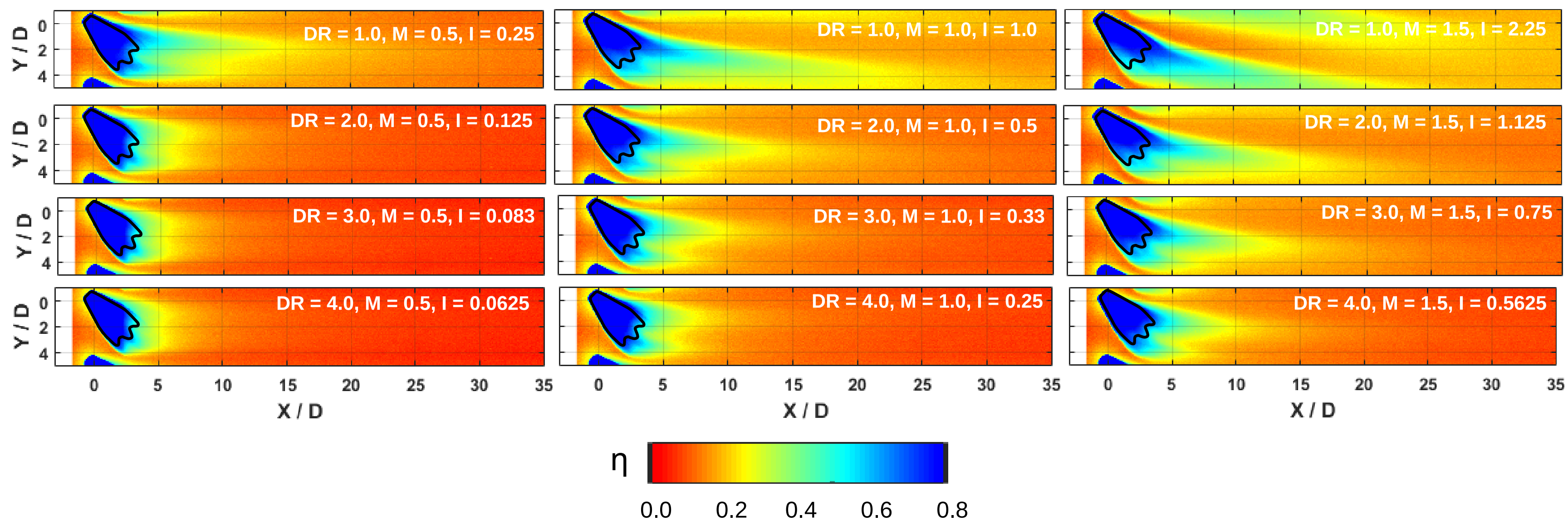

Figure 5.16: Detailed Film Cooling Effectiveness Distributions for a Duckfoot Outlet with a Racetrack Inlet

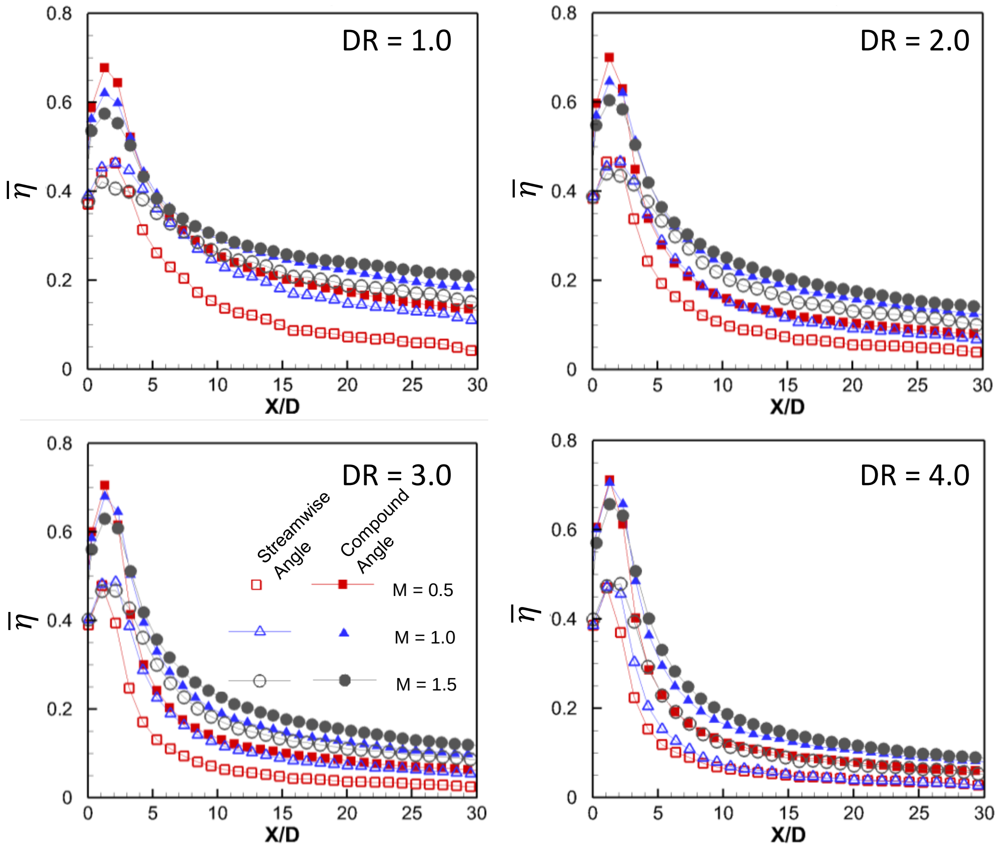

Figure 5.17: Laterally Averaged Film cooling Effectiveness for the Duckfoot Outlet with a Racetrack Inlet

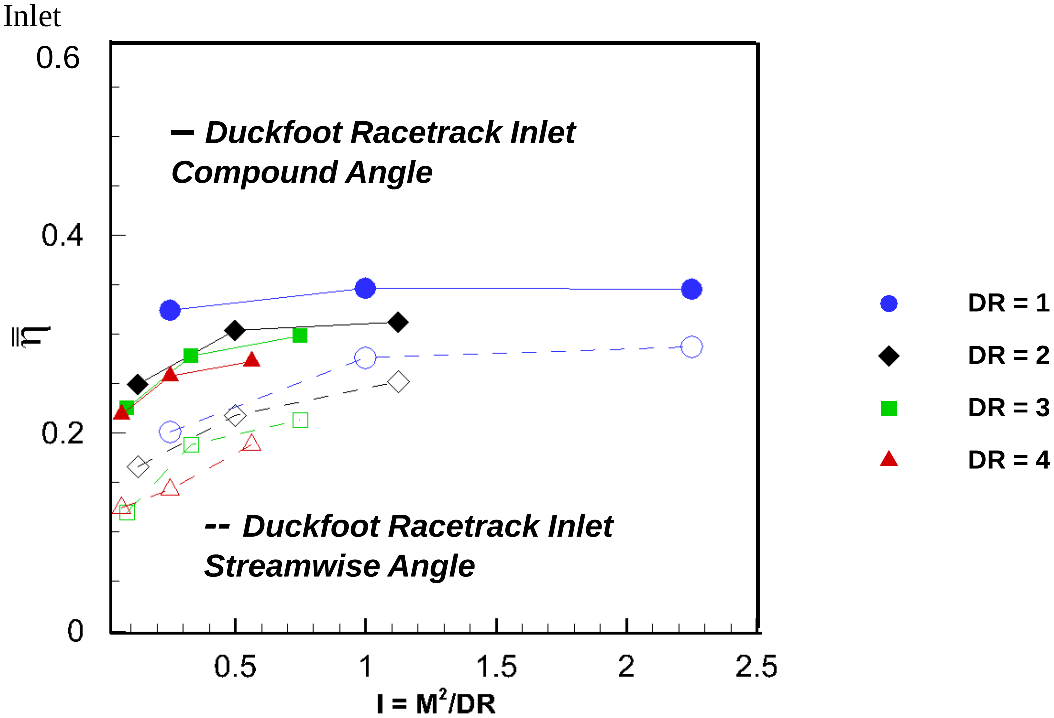

Figure 5.1 [illegible] tlet with a Racetrack Inlet

racetrack inlet does collapse for density ratios DR = 2 and 3. The DR = 1.0 shows levels higher than what was expected. The large volume of cooling flow at a low density ratio of DR = 1.0 covers the surface at the momentum flux for the hole and then shows the increased cooling efficiency. The duckfoot outlet with a dumbbell inlet also shows the trends of the previous geometries at the high density and low blowing ratio conditions. As the flow is leaving the holes film cooling holes at a density ratio of DR = 3 and 4 it is not coming out with enough momentum. Even though the vorticity near the trailing edge has been reduced with the advanced geometries. The flow still mixes with the mainstream very quickly, reducing effectiveness.

Duckfoot Outlet With a Dumbbell Inlet

In the streamwise configuration, the dumbbell inlet with a duckfoot outlet showed cooling levels much higher than any of the other inlet geometries in the study. When the dumbbell inlet is paired with the duckfoot outlet, it drastically alters the outlet shape of the hole. The outlet then becomes wider and shorter than the other versions of the duckfoot. When the geometry is tested in the streamwise orientation, the coolant is spread out to the entire width of the hole. This results in a wider region of high cooling effectiveness. When the compound angle is applied to this advanced geometry the opposite effects are seen. The coolant is no longer able to fill the “toes” of the duckfoot geometry and most of the coolant is dispersed from the one side of the hole. This means that the lateral spreading effect of the hole is not able to function correctly. A reduction in cooling effectiveness is then seen across the surface; these effects are clearly seen in Figure 5.19. The high density ratio, low blowing ratio cases that already have low flow momentum are very effected by the compound angle version of the hole geometry. The mainstream flow has more interactions on the side of the hole that is laterally further from the inlet. That means there is more coolant to mainstream interaction that further decreases cooling effectiveness.

The quantitative drop in cooling effectiveness is very clearly seen in the laterally averaged plots in Figure 5.20. The net effect of the compound angle on the duckfoot outlet with a dumbbell inlet is a reduction in cooling effectiveness. It seems that the side of the hole which is further upstream has more mainstream interaction. This cooling flow is mixed into the boundary layer much quicker than the flow further downstream of the hole, giving the uneven distribution of coolant. This mixing is one of the main attributing factors in the reduction of cooling effectiveness. The overall area average for the duckfoot outlet dumbbell inlet also confirms that the drop in cooling effectiveness over the surfaces. Figure 5.21 of the overall averages shows this effect. Looking at the overall area average results for the duckfoot outlet with a dumbbell inlet, the cooling effectiveness drops significantly with the addition of the compound angle for all cases.

Duckfoot Two With Dumbbell Inlet

The duckfoot outlet has two different versions, the previous three hole geometries were the same outlet with only the three inlet geometries altering the shape at the outlet. Duckfoot two is an altered version of the duckfoot geometry. With the same inlet, a thinner outlet has been generated. The design of the hole forces even more of the cooling flow laterally away from the inlet source. This should in theory further increase the cooling effectiveness. In the streamwise orientation this cooling hole performs better than any of the others in this study. The same effects seen with the duckfoot outlet with a dumbbell inlet do still occur when the compound angle is applied to the

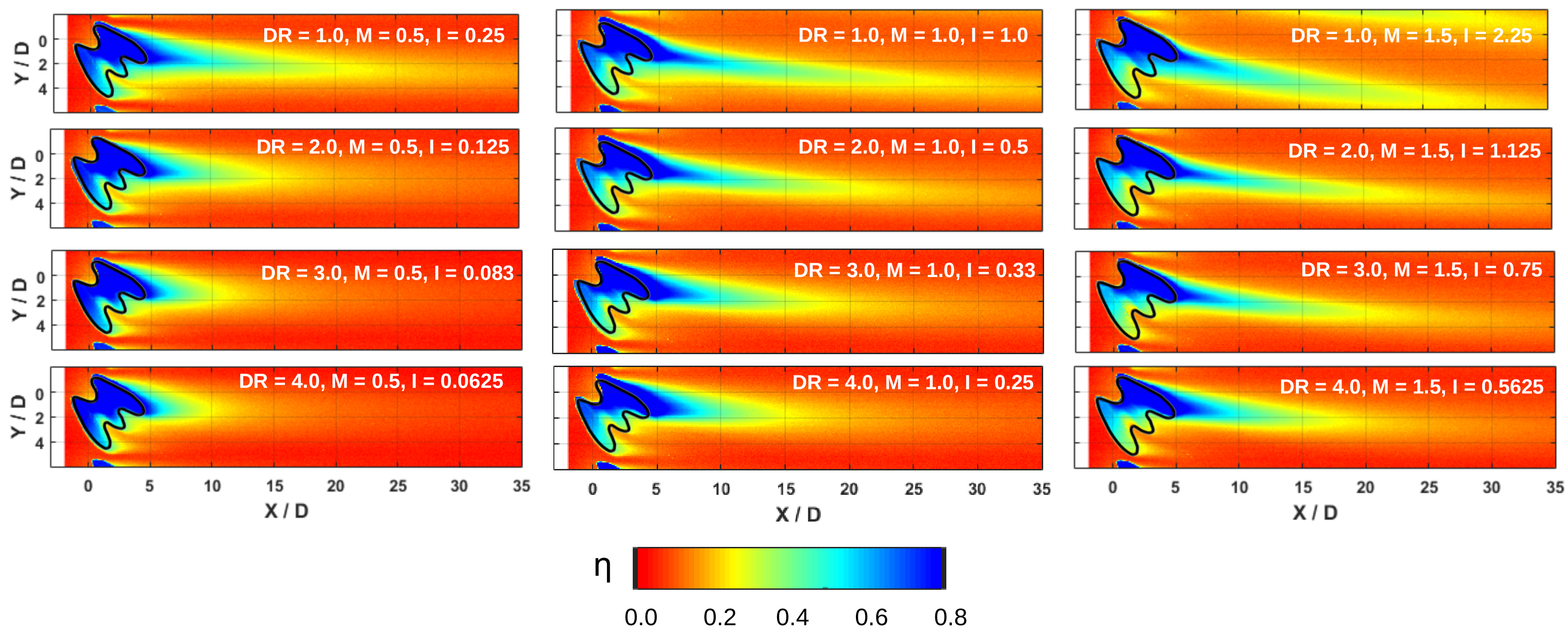

Figure 5.19 Detailed Film Cooling Effectiveness Distributions for a Duckfoot Outlet with a Dumbbell Inlet

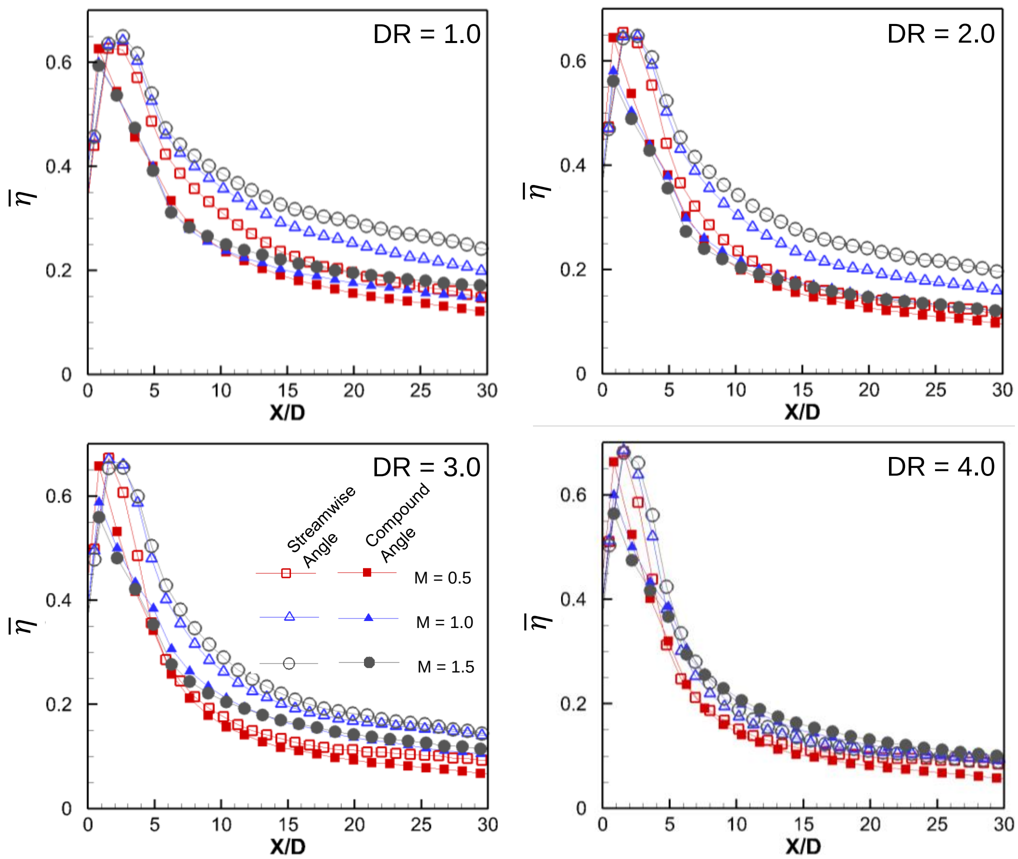

Figure 5.20: Laterally Averaged Film cooling Effectiveness for the Duckfoot Outlet with a Dumbbell Inlet

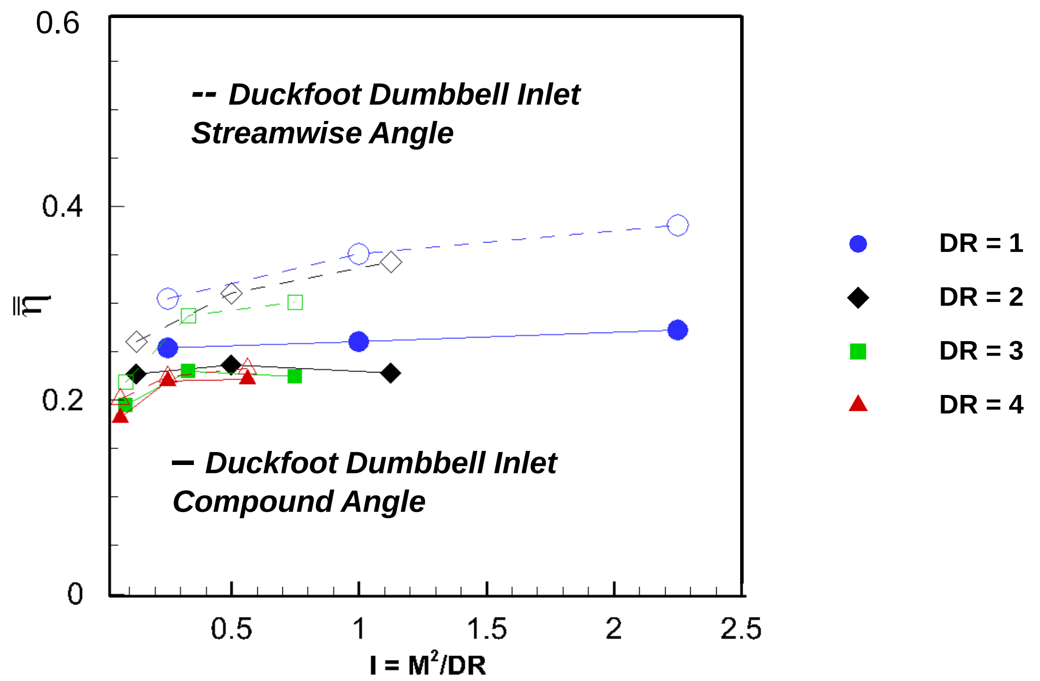

Figure 5.21: Area Averaged Film Cooling Effectiveness for the Duckfoot Outlet with a Dumbbell Inlet

duckfoot two outlet with a dumbbell inlet. Figure 5.22 shows the detailed distributions for the duckfoot two outlet with a dumbbell inlet geometry. The redesign of the duckfoot outlet forces the coolant to both edges of the cooling hole. These effects are not as strong in the first duckfoot oulet with a dumbbell inlet compared to the duckfoot two outlet with a dumbbell inlet. However, the flow is being slowed down too much with the compound angle and mixing with the mainstream is faster than was seen with the streamwise testing of this geometry. This is easily seen in the detailed plots. When the density ratio increases, the effectiveness gradually drops, the cooling flow is losing even more momentum the heavier it gets. This makes it even more susceptible to mainstream mixing.

The laterally averaged effectiveness in Figure 5.23 shows the decreases of duckfoot two are not as severe as for the first duckfoot outlet with a dumbbell inlet. However, the plots still clearly illustrate that the effectiveness has been reduced with the introduction of the compound angle. The plots show that at a density ratio of DR = 4.0 the cooling over the surface was nearly identical. This is the only flow condition that did not show a large drop in effectiveness. These trends are confirmed with the area overall averaged plot in Figure 5.24. The overall average is higher for the streamwise case until the highest density ratio. Even though the results show similar cooling levels for this case, there is only the potential for losses in effectiveness with the addition of the compound angle for the duckfoot two outlet with a dumbbell inlet geometry. For most of the geometries, the addition of the compound angle has made a positive effect on cooling effectiveness, surprisingly this does not hold true for the outlet geometries that have been altered with the dumbbell inlet.

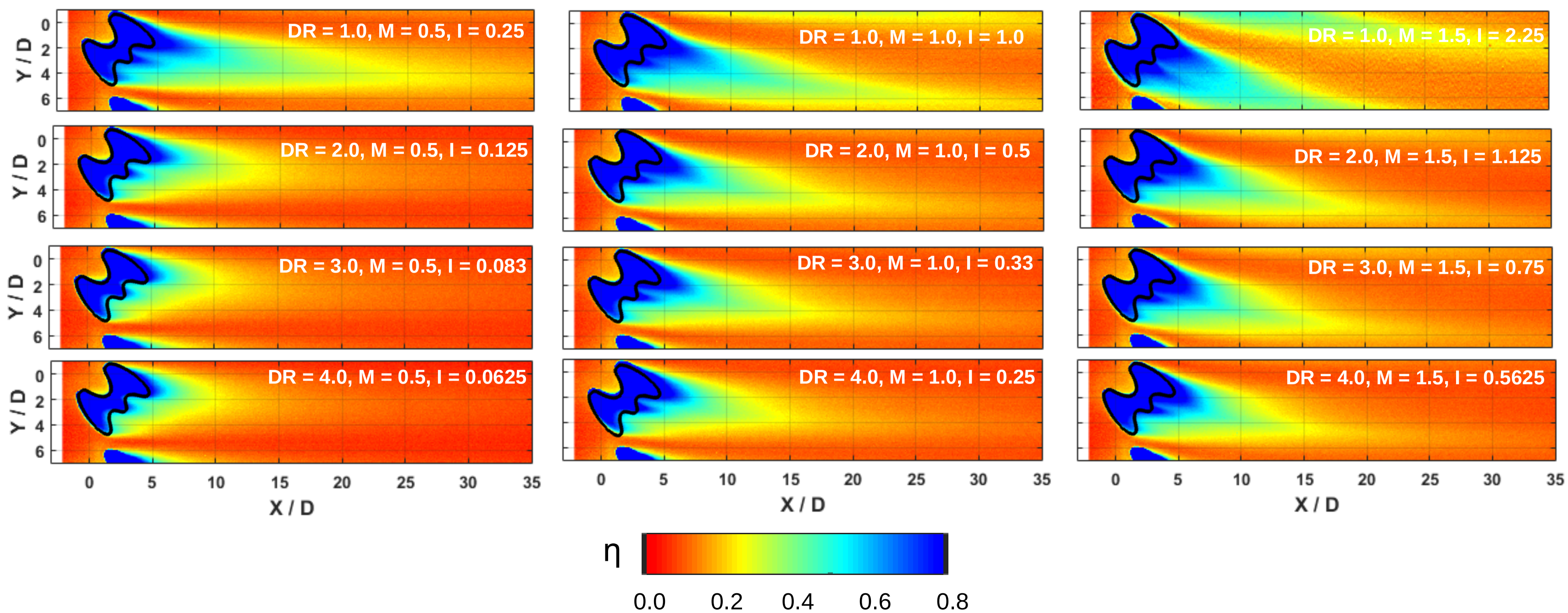

Figure 5.22: Detailed Film Cooling Effectiveness Distributions for a Duckfoot Two Outlet with a Dumbbell Inlet

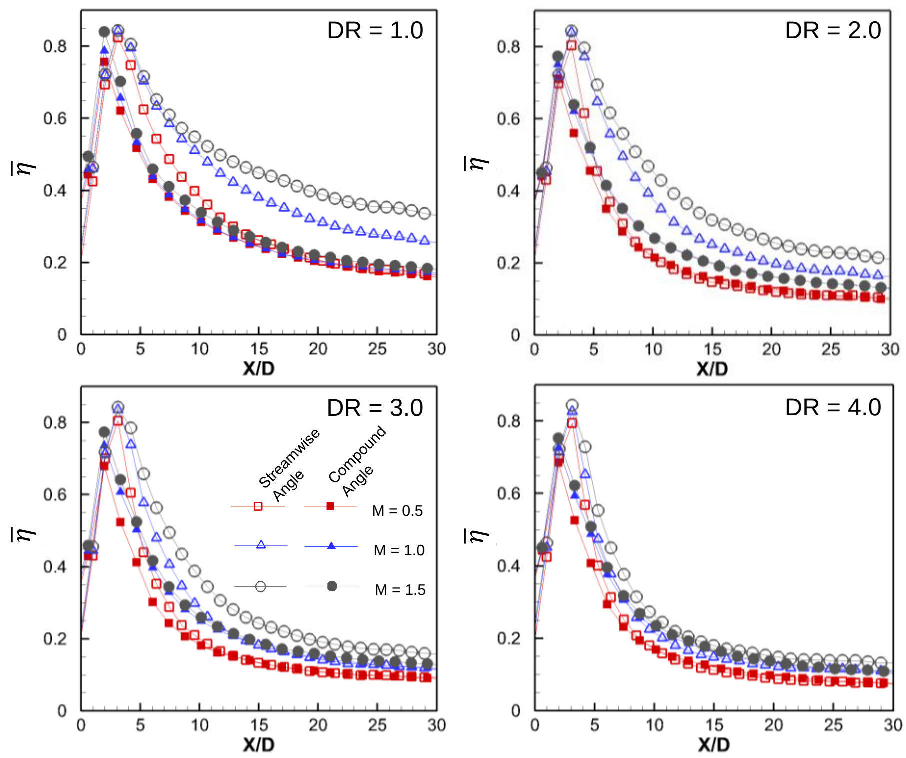

Figure 5.23: Laterally Averaged Film cooling Effectiveness for the Duckfoot Two Outlet with a Dumbbell Inlet

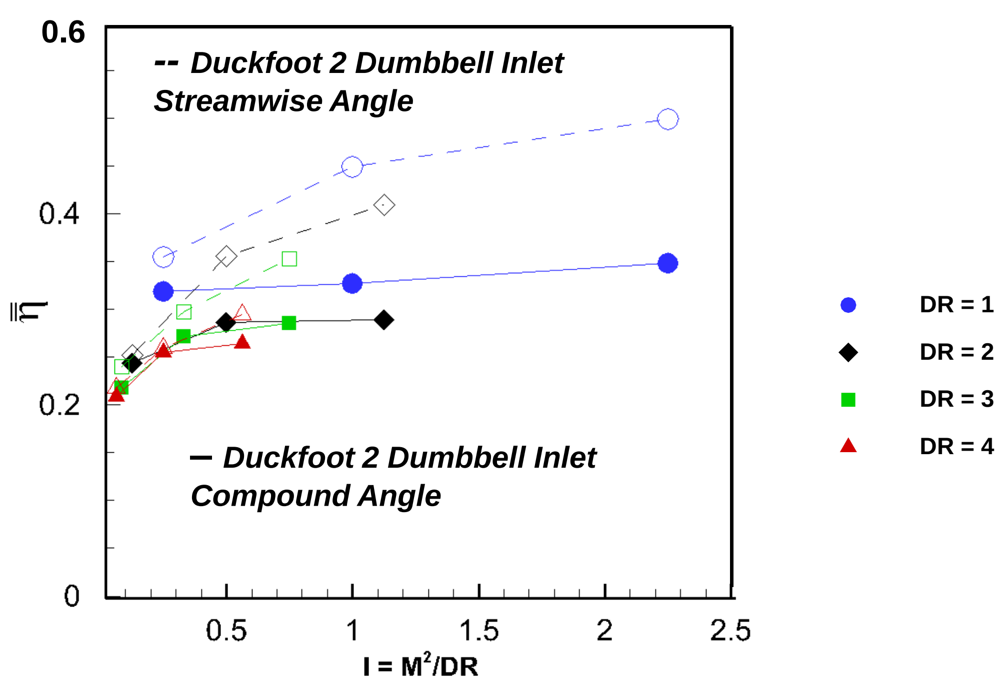

Figure 5.24: Area Averaged Film Cooling Effectiveness for the Duckfoot Two Outlet with a Dumbbell Inlet

The detailed and quantitative results have been presented for each of the seven cooling geometries in both the streamwise and compound angle orientations. In order to get a sense of the true effects that just the inlet or outlet has on cooling effectiveness a direct comparison is required. More commonly, the outlet is studied and optimized in film cooling studies. In order for this to happen all other factors such as varying inlet shape must be eliminated. In this study, this means looking at the cooling holes which have a round inlet. To show these effects, the laterally averaged cooling effectiveness of three different hole shapes will be compared. The basic round, laidback fanshape outlet with a round inlet, and the duckfoot outlet with a round inlet geometries will be examined. Starting at a density ratio of DR = 1.0, the effect of the outlet is seen in Figure 5.25. These plots look at the streamwise versus compound angle for each hole type and compare the three holes types to each other with the duckfoot outlet with a round inlet showing the highest performance. At the low density ratios the three distinct outlet shapes are easy to separate and show clear gradual improvement over the streamwise versions of each hole. When the density ratio is increased in Figure 5.26 the cooling trends start to collapse on each other. For the density ratio of DR = 3.0 the cooling trends still show the duckfoot outlet with a round inlet is the best performing geometry, but at the low momentum cases, all three geometries perform with similar lateral cooling effectiveness. When the blowing ratio is increased, the laidback fanshape outlet with a round inlet and the duckfoot outlet with a round inlet perform better than the round hole; yet these two are still close to each other. The one exception is the compound angle duckfoot round which out-performs the five other holes on the plot at the higher blowing ratio.

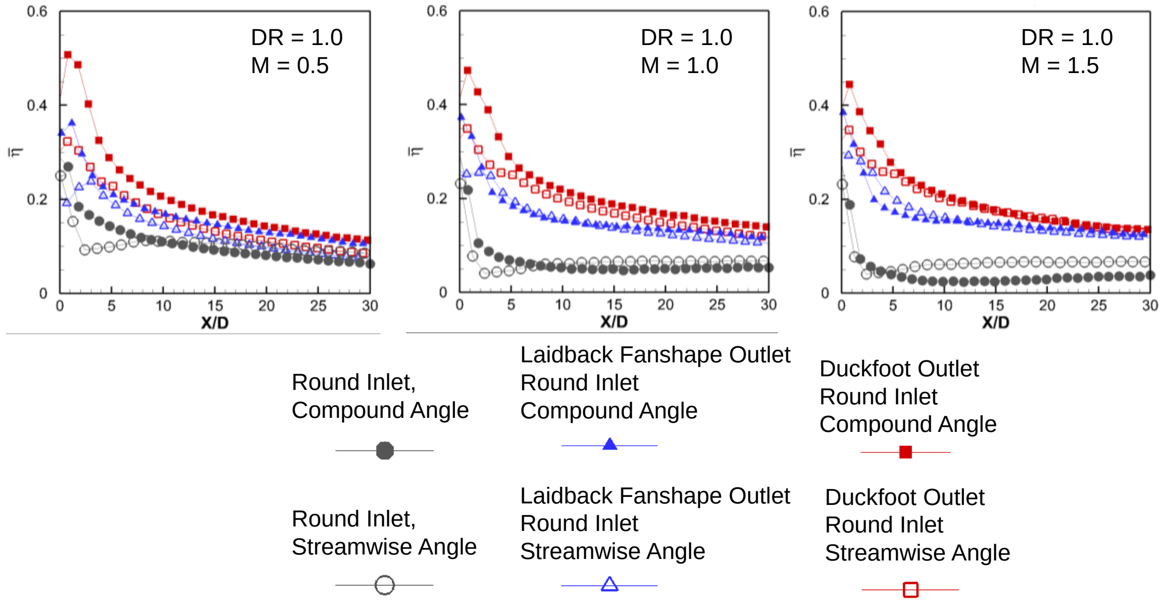

Figure 5.25: Hole Outlet Effects on the Laterally Averaged Film Cooling Effectiveness at DR = 1.0

This outlet is the most efficient at spreading the coolant out from the round hole. This shape keeps the coolant in the outlet more efficiently and thus spreads it over the surface more efficiently as well; resulting in the highest cooling effectiveness between the three holes. When looking at the averages in Figure 5.27 the results from the lateral average plots are confirmed. The laidback fanshapes show their insensitivity to changes in blowing ratio, especially at low density ratios. The outlet study shows the effects of a more advanced outlet to cooling effectiveness. Overall the duckfoot has shown to perform the best; however, this increase in effectiveness must be balanced in terms of cost of production between the duckfoot and the laidback fanshape.

The inlet effect on film cooling has not been properly examined, but can be seen in Figure 5.28. Much like with the outlet comparison other differences between the hole types need to be eliminated to show the true inlet effects. To understand the inlet effects

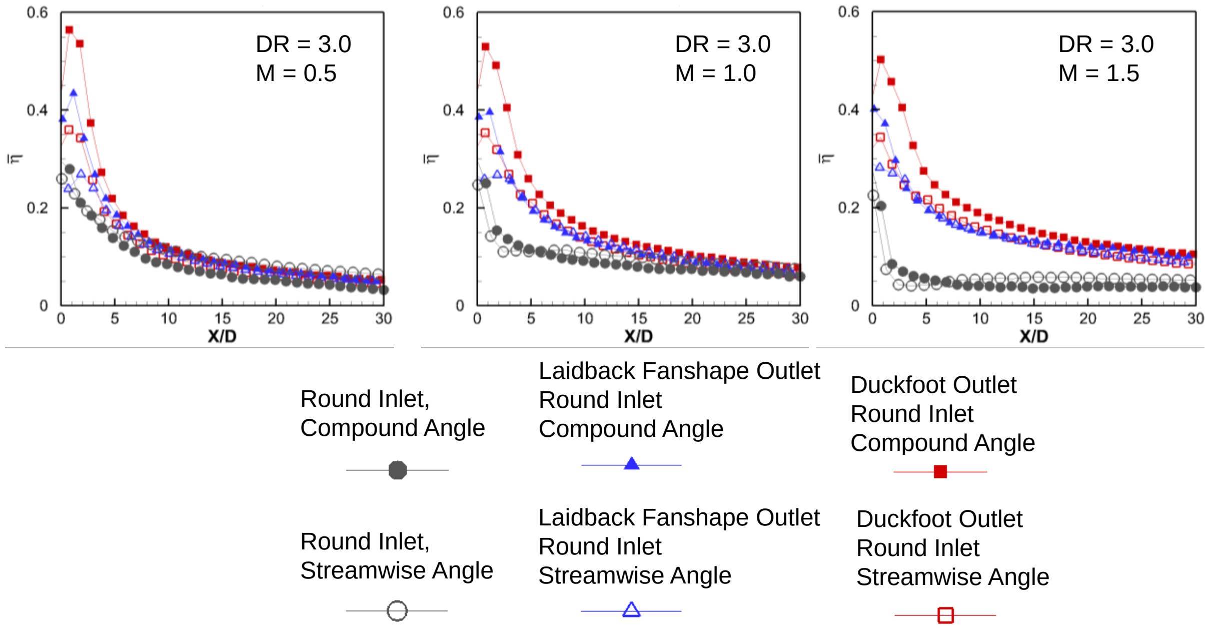

Figure 5.26: Hole Outlet Effects on the Laterally Averaged Film Cooling Effectiveness at DR = 3.0

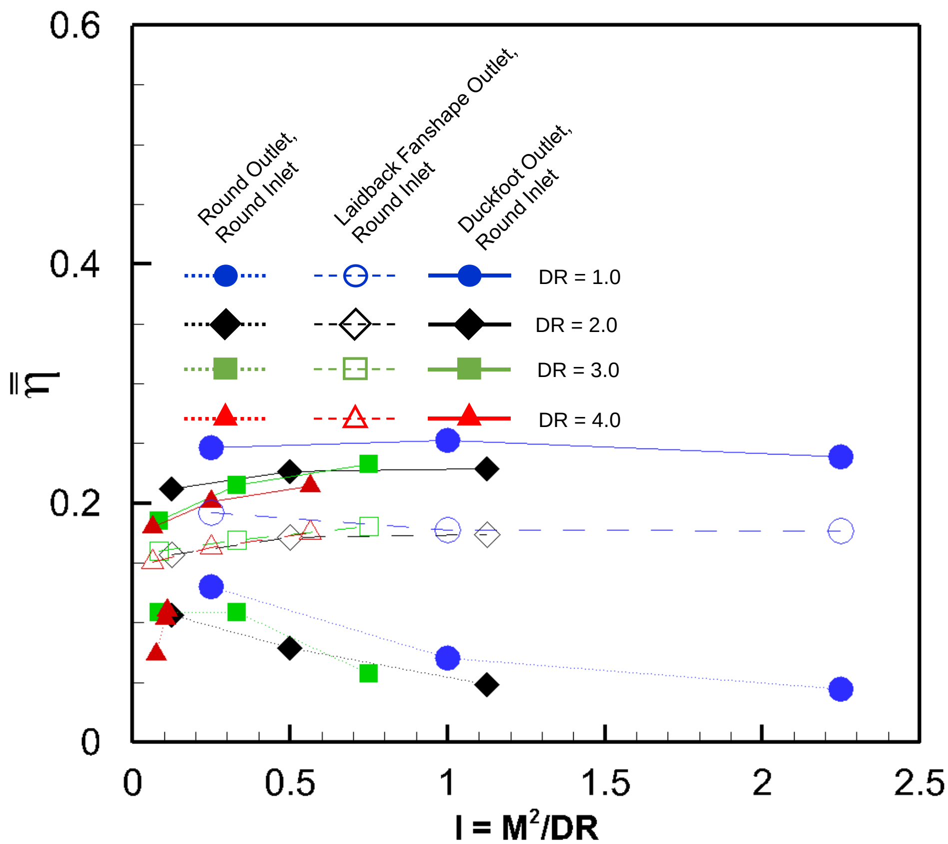

Figure 5.27: Hole Outlet Effects on the Overall Area Averaged Film Cooling Effectiveness

two different comparisons will be made. One will be made with the laidback fanshape outlet and one will be made with the duckfoot outlet. The laterally averaged effectiveness of the two laidback fanshaped outlets is compared. These holes overall do have a slightly different shape, but that difference is generated from only the different inlets of each geometry. At a density ratio of DR = 3.0, with the compound angle the inlet has shown only an increase in cooling near the trailing edge of the hole.

Seen in Figure 5.29 the inlet effects for the duckfoot outlet are more complicated and unexpected for the compound angle cases. Instead of the gradual increase in cooling effectiveness between the inlets, the duckfoot outlet with a racetrack inlet now shows to have the second highest cooling performance and is very near the performance of the duckfoot 2 with a dumbbell inlet. As well, at the density ratio of DR = 3.0, all four of the lines almost collapse onto each other; the reduced momentum of the cooling flow means all of the effectiveness decay rates are almost the same at large X/D locations. Only near the trailing edge was there big difference between the laterally averaged cooling rates of the four cooling geometries. This is seen because the inlets and compound angle is slowing and spreading the coolant over the surface more effectively. The positive effects end with the racetrack inlet; this hole geometry seems to generate the perfect momentum flux as the flow leaves the geometry and enters onto the surface. The overall area average results for the laidback fanshape outlets and duckfoot outlets are seen in Figures 5.30 and 5.31. They show that the racetrack inlet has resulted in an increase in cooling for both of the outlets. At the density ratio of DR = 3.0 the overall improvement from the round inlet to the racetrack inlet is an effectiveness of around $\eta = 0.05$ to 0.07. This is overall a small increase for the altered geometries. The compound angle has in effect, reduced the

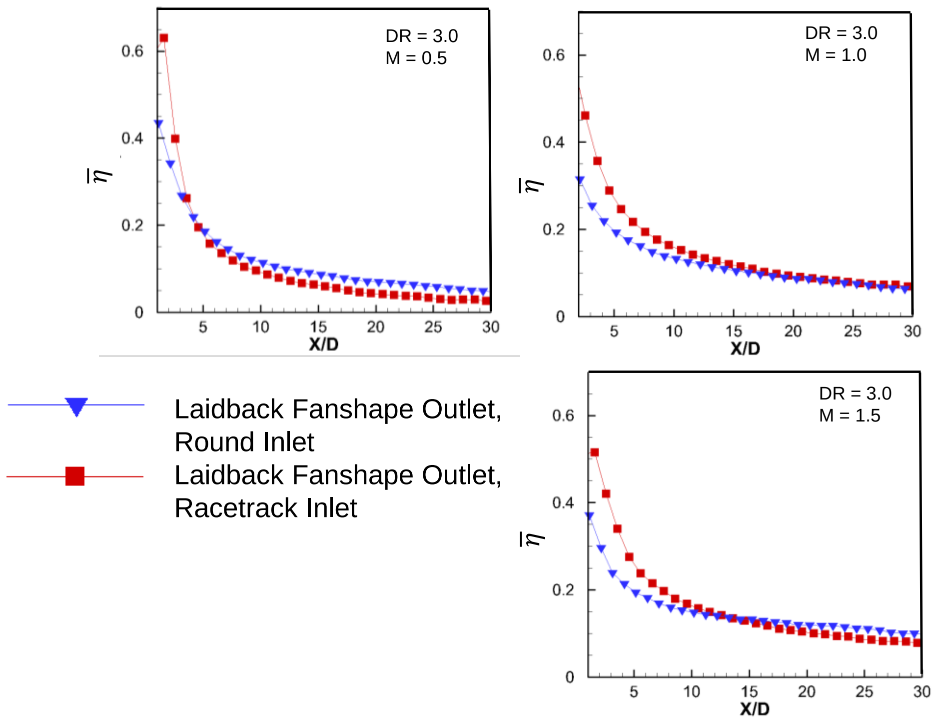

Figure 5.28: Effect of Inlet Shape on the Laterally Averaged Film Cooling Effectiveness From Laidback Fanshaped Holes (DR = 3.0)

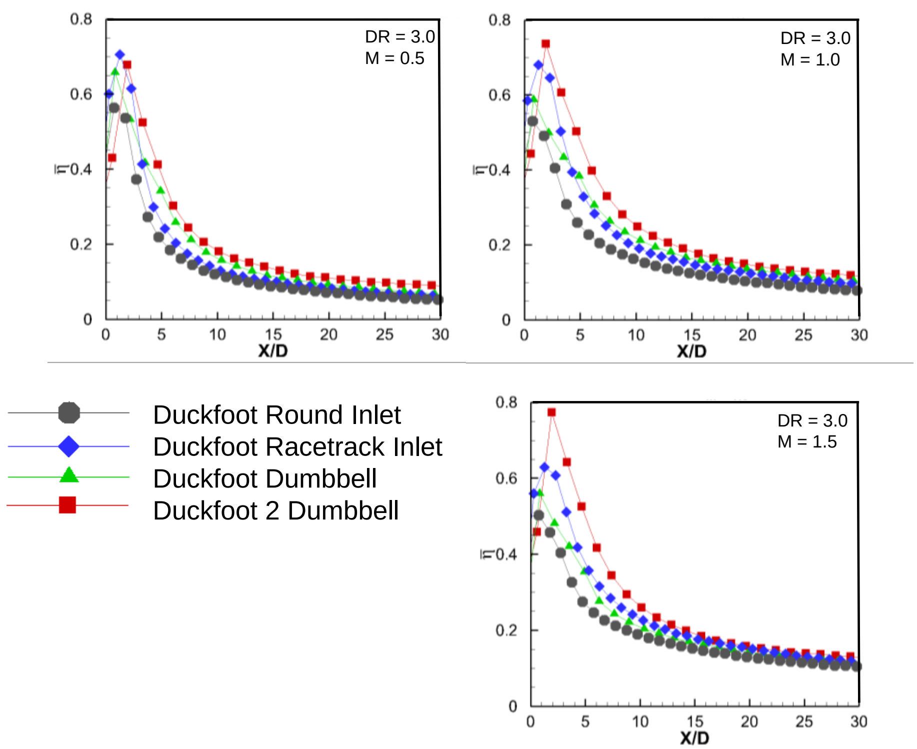

Figure 5.29: Effect of Inlet Shape on the Laterally Averaged Film Cooling Effectiveness From Dumbbell Shaped Holes (DR = 3.0)

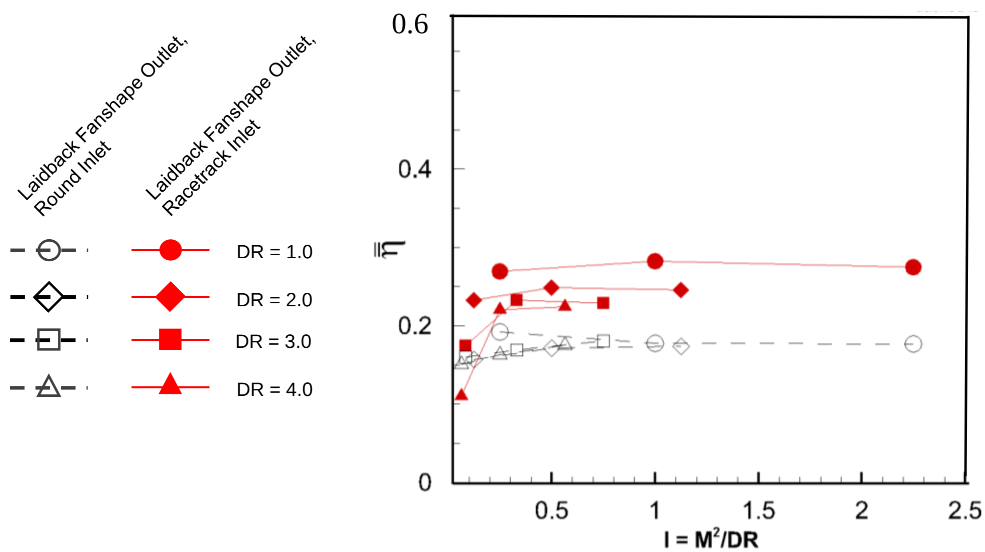

Figure 5.30: Inlet Effects on Averaged Effectiveness For Laidback Fanshape Outlets

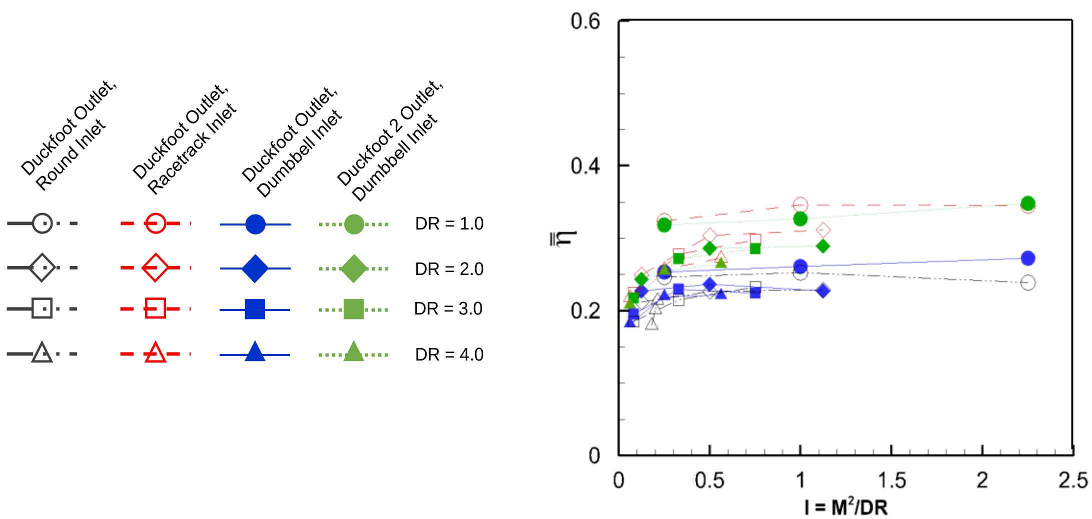

Figure 5.31: Inlet Effects on Averaged Effectiveness For Duckfoot Outlets

differences between the two inlet shapes, but it has also increased the cooling performance of both laidback fanshapes. The inlet has had a slightly different effect on the duckfoot oulet. The streamwise cases show a gradual increase in overall cooling effectiveness from the round to the dumbbell inlets. Overall area average plots show different trends. The four shapes form two groups with the duckfoot outlet with the dumbbell inlet and round inlet showing similar cooling levels, and the duckfoot 2 outlet with a dumbbell inlet and racetrack inlet forming similar trends. The duckfoot outlet with a racetrack inlet is a much more simple shape than the duckfoot 2 outlet with a dumbbell inlet. With the addition of the compound angle, both are performing at similar efficiencies. This means the compound has proven to have an excellent effect on the racetrack inlet geometries and a negative effect on the dumbbell inlet cooling shapes.

In total seven different tests have been performed in this experiment. Seven different hole types were tested in the compound angle and streamwise orientations, with stremwise data provided by Vinton [65]. Based on all the results of the study, generally, the same three cooling holes performed the best for the streamwise and compound angle cooling tests. For both the streamwise and compound angle holes, the duckfoot outlet with a dumbbell inlet and duckfoot 2 outlet with a dumbbell inlet performed in the top three of all the tested hole geometries; the effectiveness is seen in Figure 5.32. For the streamwise case the laidback fanshape outlet with a racetrack inlet slightly outperformed the duckfoot outlet with a racetrack inlet. While with the compound angle holes the duckfoot outlet with a racetrack inlet performed closely with duckfoot 2 outlet with a dumbbell inlet. These results show two things. The compound angle has had an effect on the performance of the duckfoot outlet with a racetrack inlet. Elevating it from performing below a streamwise laidback fanshape to being just as effective as the streamwise, duckfoot 2 outlet with a dumbbell inlet hole. This more simple hole, relatively speaking, now shows similar cooling efficiencies as this very advanced intricate cooling geometry. Also, it is clear to see how the compound angle has effected both of the duckfoot outlets with a dumbbell inlet geometry. It becomes clear that adding a compound angle to these geometries negates the effects of the dumbbell inlet. This is an unexpected and surprising result.

Figure 5.33 looks at each individual, overall area averaged effectiveness for each of the 14 tests. A plethora of data has been shown with many different trends and results to analyze. Within each of the 14 hole types, twelve different flow conditions have been recorded. With this much data it can be difficult to draw the correct conclusion. In order to make the most relevant decision and recommendations, the flow conditions must be narrowed down. The flow conditions of DR = 3.0 and M = 1.5 will be solely looked at for this final analysis; these are the likely conditions that these cooling geometries would be operating under in the real world.

Looking specifically at the streamwise cases, the effect of the inlet is clear, the cooling between the round, racetrack, and dumbbell inlets gradually increases as the more advanced inlets are added to the advanced shapes. The effects of the inlet is clear, as the laidback fanshape and duckfoot outlets with racetrack inlets show almost identical effectiveness levels. The highest performing shape is the duckfoot 2 outlet with a dumbbell inlet shape providing an effectiveness at $\eta = 0.35$. By comparison, the much simpler duckfoot outlet with a racetrack inlet shows a cooling effectiveness of $\eta = 0.21$. There is a 66% increase in cooling with the duckfoot 2 outlet with the dumbbell inlet over the duckfoot outlet with the racetrack inlet while in the streamwise orientation. This increase could potentially justify the use of the much more complicated and expensive duckfoot 2 outlet with a dumbbell inlet hole geometry. In this scenario, the compound version of these cooling holes really becomes important. The duckfoot outlet with a

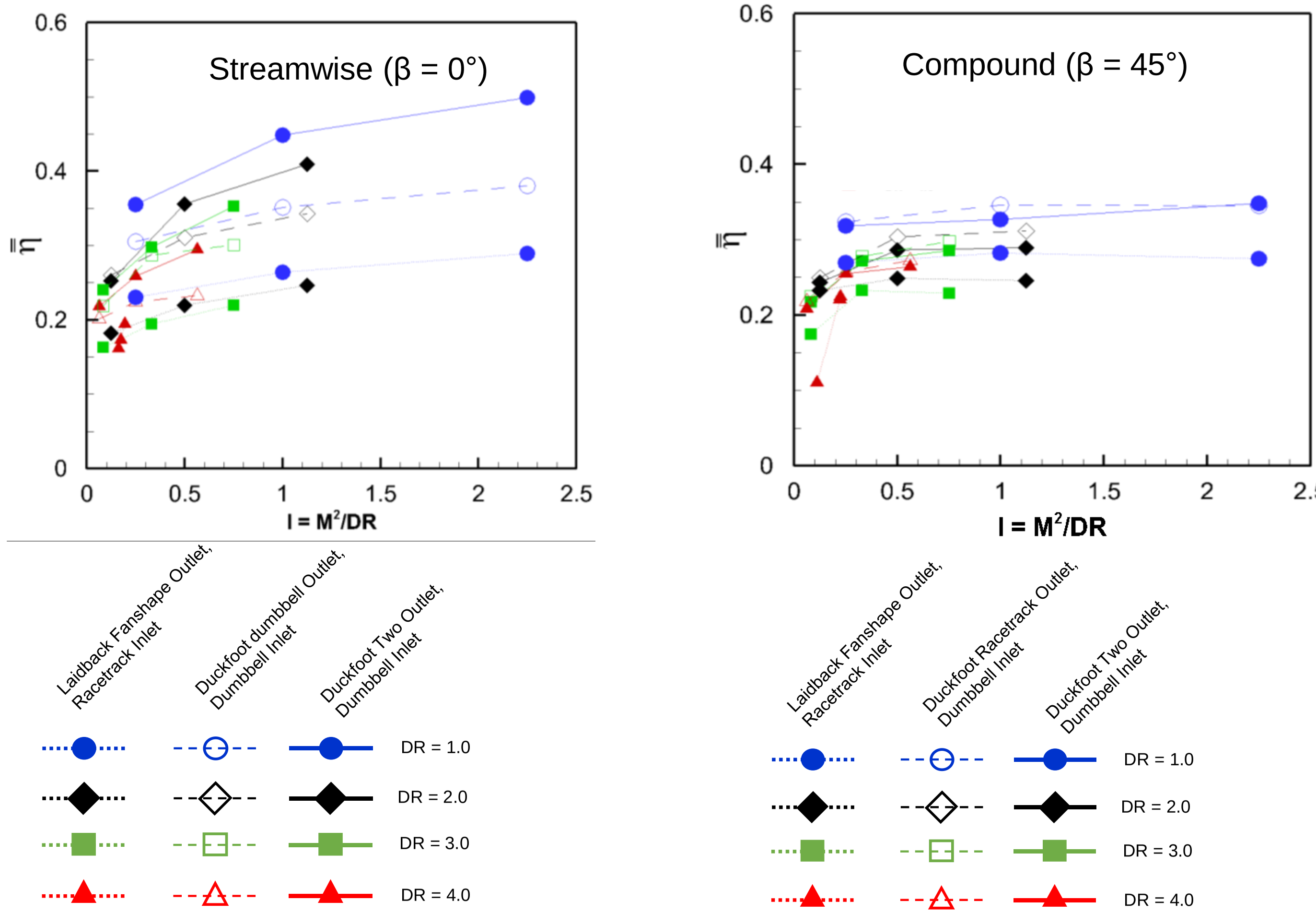

Figure 5.32: Overall Average of the Most Effective Geometries With Both Compound and Streamwise Angles

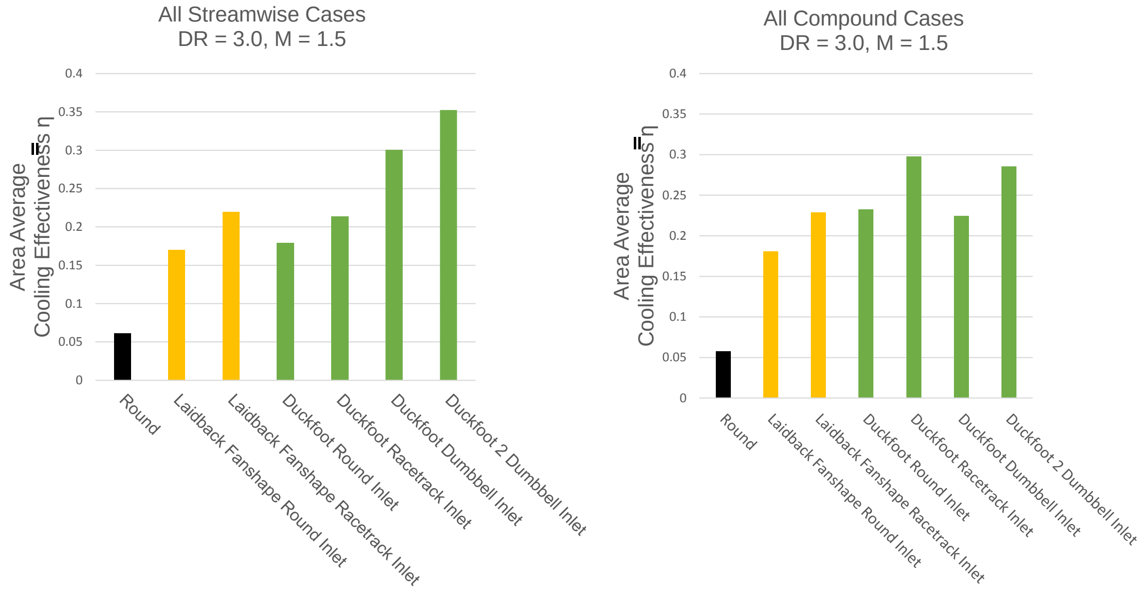

Figure 5.33: The Overall Effectiveness of Each of the 14 Tested Cooling Geometries Tested at a DR = 3.0 and M = 1.5

racetrack inlet gained the most cooling efficiency with the addition of the compound angle, showing an increase of 35% over the streamwise version of the hole. In addition to this, it now has an overall cooling effectiveness of $\eta \approx 0.30$. This puts it closer to the performance of the streamwise duckfoot 2 outlet with a dumbbell inlet hole. Comparing the two holes, between the compound angle duckfoot outlet with a racetrack inlet and the streamwise duckfoot 2 outlet and dumbbell inlet, there is only a 16% difference in cooling effectiveness. With this difference, now the high cost to the duckfoot 2 is less justifiable. Under these conditions, the most economical hole geometry to advance cooling design becomes the compound angle duckfoot outlet with the racetrack inlet. For the increased simplicity and thus reduced production costs, plus the overall increase in cooling performance over current film cooling geometries it becomes a very good candidate. This translates to the compound angle duckfoot outlet with a racetrack inlet having the lowest cost per total increase in performance. Additionally, it is a more open hole meaning, it has fewer tight turns and complex angles than the duckfoot 2 outlet with a dumbbell inlet. It will be more resistant to foreign object debris (FOD) clogging the cooling holes and causing cooling issues. Ultimately, all of the results from this experiment say that overall, the best geometry tested was the streamwise, duckfoot 2 outlet with the dumbbell inlet; however, this is not the most recommended hole geometry of the study. The compound angle, duckfoot outlet with a racetrack inlet should be viewed as the most ideal geometry The performance of the racetrack inlet in both the streamwise and compound versions of each hole are very clear. Both of the outlets experience an improvement in cooling performance. The duckfoot sees a larger gain from the racetrack addition. The deeper toes in the geometry keep the coolant in the cooling hole longer and force it further laterally from the inlet of the hole. In the streamwise orientation, the duckfoot holes are the best at minimizing trailing edge vorticity of any of the tested geometries. This greatly attributes to the cooling performance they are able to provide. The compound angle has neutralized these gains and caused the drastic drop in cooling for both of the dumbbell inlet holes. The duckfoot outlet with a racetrack inlet hole also sees greatly reduced trailing edge vorticity in the streamwise orientation. However, when this hole is rotated the vorticity could be theoretically reduced further also attributing to decreased downstream film to mainstream mixing, and the increased overall cooling effectiveness.

CHAPTER SIX

Compound Angle Film Cooling Conclusions

A new wind tunnel has been designed and built for the use in Pressure Sensitive Paint (PSP) experiments. This new tunnel has been optimized for the ease of testing flat plate PSP experiments. It has an internal cross sectional area 4 times of the old tunnel and is able to sustain an internal velocity of approximately 12 m/s. This larger tunnel has also been designed to expand the types of experiments that can be performed. The new tunnel has been validated by running similar tests and producing similar results as old tunnel. In this experiment, results from both wind tunnel test setups have been used.

Several conclusions can be drawn about the effects of the compound angle on the film cooling effectiveness of advanced geometries. For the round hole, two changes have been observed in the cooling effectiveness. Near the trailing edge, the cooling effectiveness was elevated for the round hole while the downstream effectiveness was reduced. Overall, the averaged cooling effectiveness with the round hole was not increased with the addition of the compound angle.

The compound angle did have a positive effect on cooling effectiveness for the laidback fanshape geometries. The laidback fanshape outlet with a round inlet showed higher cooling effectiveness than the simple round hole. This was seen because of the laidback fanshape aspects of the hole. The compound angle did have a slight effect on the cooling effectiveness of the laidback fanshape outlet with a round inlet. Near the trailing edge of the hole, the cooling was greatly increased, but as the flow continued downstream, the effectiveness decays at the same rate as the streamwise orientation of the hole. With the racetrack inlet added to the laidback fanshape outlet, the cooling effectiveness was shown to increase. The coverage at the trailing edge was increased and unlike the round inlet case, the racetrack inlet case did not have the cooling effectiveness decay at the same rate resulting in slightly enhanced cooling over the whole surface.

The duckfoot outlets had a variety of responses with the addition of the compound angle. Looking first at the duckfoot outlet with a round inlet, similar trends to the laidback fanshape holes were seen and improved upon overall. The addition of the compound angle to the duckfoot outlet with a round inlet has pushed the cooling effectiveness well above what was seen with the streamwise case. Also, because the cooling started off higher and decayed slower, the effectiveness was higher than it was for the streamwise case. When looking at the duckfoot outlet with a racetrack inlet, similar trends as the duckfoot outlet with the round inlet case were seen; in this case however, the improvements were the highest of any of cooling geometries tested. Near the trailing edge of the outlet there is a 50% increase in cooling effectiveness while downstream the effectiveness is higher at every point over the streamwise version of the hole.

Up to this point, the addition of the compound angle has either had no significant effect on overall cooling effectiveness, or it has generally improved the overall cooling performance of the geometries. The addition of the compound angle to the dumbbell inlet, duckfoot outlet geometries only shows negative effects to cooling performance. In the case of duckfoot outlet with a dumbbell inlet, the compound angle has produced a dramatic drop in the cooling effectiveness. The effects are not consistent for all the flow conditions. At the low density ratios, the cooling air is forced to be ejected from only one side of the geometry. This gives the cooling distributions a more pointed look, instead of the gradual change in cooling effectiveness seen in the streamwise version of the hole geometry. At high density ratios the negative effects are not as dramatic; the heavier flow with less momentum has a less significant difference in cooling effectiveness. The duckfoot 2 outlet with a dumbbell inlet also suffers from the same effects as the duckfoot one dumbbell. This version of the duckfoot is thinner forcing the coolant to the outside toes. That means, despite the compound angle, the cooling effectiveness has been reduced as significantly. At high density ratios in fact, the effectiveness was equivalent to the streamwise cases of this geometry. Despite this, the overall effectiveness in the duckfoot 2 dumbbell was not improved with the addition of the compound angle.

Limited studies have been performed to show inlet effects on film cooling effectiveness. The round, racetrack, and dumbbell inlets do have large effects of the performance of a film cooling outlet geometry. Looking in the streamwise condition, the round inlet centers the flow reducing the effect of the different outlet shapes. As seen with the laidback fanshape outlet with a round and the duckfoot outlet with a round inlet performing very similarly, despite the differences in the outlet. The same results are seen with the duckfoot outlet. As all three inlets are applied to the outlet geometry, only the changes in the inlet alter the outlet shape. Comparing all three duckfoot one shapes, it is clear the effectiveness is increasing as each inlet is tested. The negative side of this comes from the cost of production. The dumbbell inlet would theoretically be much more expensive to produce than a round hole. Choosing the cooling geometry type for each blade is a big decision to control production costs and long term running costs of each engine. This means the cooling effects of the inlet also need to be taken into account when deciding what shape will be used for the film cooling scheme.

The addition of the compound angle to these advanced shapes has produced positive and negative effects for the cooling effectiveness. The duckfoot outlet with the round and racetrack inlets have shown to have only increasing effects with the compound angle. When the duckfoot outlets were paired with the dumbbell inlets the result was a reduced overall effectiveness. The streamwise version of the duckfoot outlet with the dumbbell inlet shows to have very high effectiveness; this cooling efficiency has actually been matched with the compound angle, duckfoot outlet racetrack inlet. This is a very important result. When looking at the more traditional, laidback fanshape, the addition of the compound angle has also increased the overall cooling performance. Meaning that currently used cooling geometries can actually be used more efficiently if they were just orientated differently with a compound angle. Overall the highest levels of cooling effectiveness have come from the streamwise, duckfoot 2 outlet with the dumbbell inlet. Over the same physical area as all the others, this geometry showed to have a cooling effectiveness of around $\eta = 0.5$. This very advanced cooling geometry has performed extremely well under every engine operating condition; however, this geometry would be very difficult and expensive to produce on a turbine blade. That means overall, it is recommended the next step forward in improving film cooling effectiveness be with the duckfoot one outlet with the racetrack inlet.

There is additional work that needs to be done with these film cooling geometries. The inlet of the film cooling geometry has been shown to have large effects on the cooling effectiveness. More research needs to be performed in this area. The aspect ratio and shape of the inlets need to be altered and optimized. The results of this study have shown that the inlet can have drastic effects on the overall cooling performance of an outlet geometry. The inlets vary in shape and aspect ratios from 1:1 to 2.65:1. These inlets have helped to spread out the flow, because of this, there needs to be more investigation as to what aspect ratios and inlet shapes will provide the greatest improvements. In addition, the advanced duckfoot 2 outlet with the dumbbell inlet, needs to be studied further. This amazing cooling performance is not well enough understood. A CFD study on dumbbell inlet geometries would help to understand to physics and fluid dynamics that are occurring inside this advanced shape. A CFD study would be a great start into understanding the flow physics inside of this cooling hole. Previous S-PIV investigations by Vinton [65] show that vorticity at the trailing edge of the hole in the streamwise orientation is reduced compared to the round hole. This understanding of the flow inside of the advanced cooling shapes can help designers create new and improve currently used film cooling holes, just as the addition of the compound angle has done. Finally, because the duckfoot outlet with the racetrack inlet showed to have such an improvement, PIV studies on the duckfoot outlet modified with a compound angle would also be extremely beneficial. This would allow for the further understanding of how the rotated holes are reducing the vorticity along the surface and helping to increase the cooling effectiveness.

APPENDICES

APPENDIX A

Appendix A contains all of the detailed drawings for all of the fabricated parts that were built for the new wind tunnel used in these experiments. Most of the parts were manufactured in house. The exceptions are the air inlet and the diffuser. These two components were built by NORFAB inc. the two pieces were build out of 306 grade stainless steel. The metal frame and supports are made from standard 1026 steel. The wind tunnel itself is made from one half inch thick polycarbonate sheets from Tap Plastic. The detailed work on all the components was completed at Baylor by our in house machinist. Overall, the tunnel foot print is approximately ten feet long, three feet wide, and eight feet tall. The metal drawings are listed first, with the drawings used in the plastic tunnel after that, and finally the plenum drawings are included last.

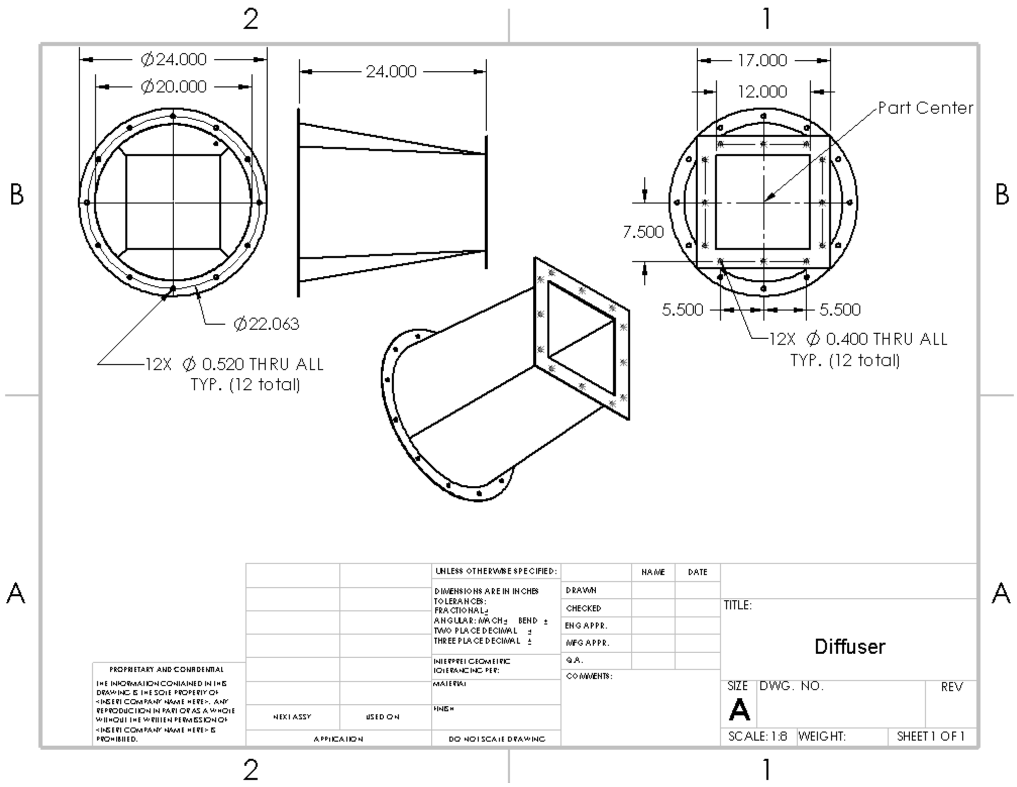

Figure A.1: Detailed Diffuser Drawing

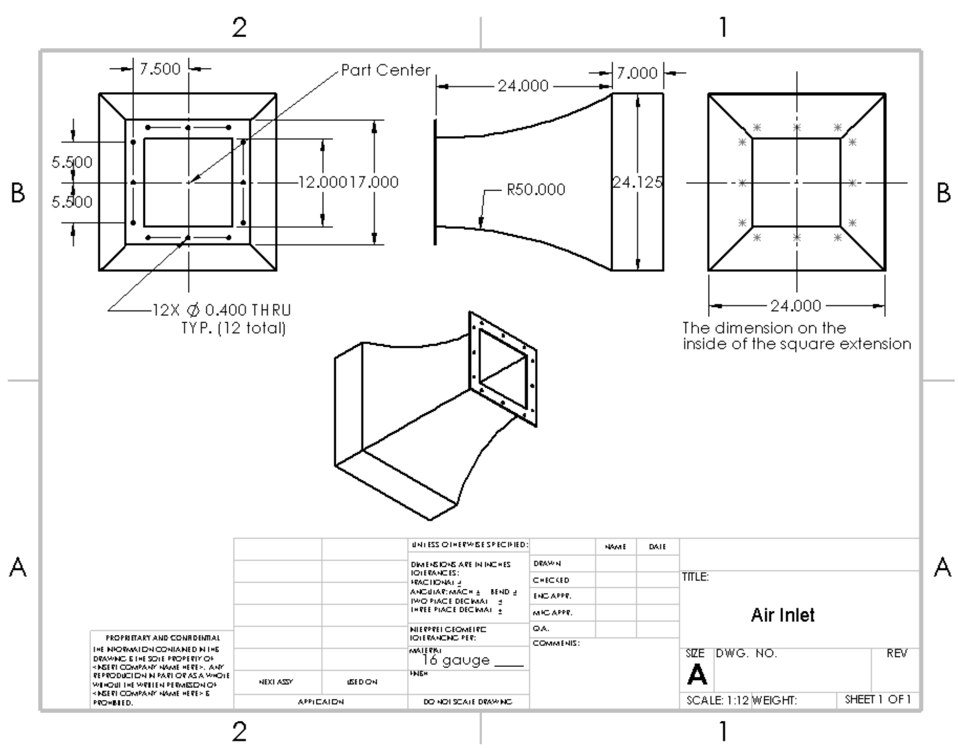

Figure A.2: Detailed Inlet Drawing

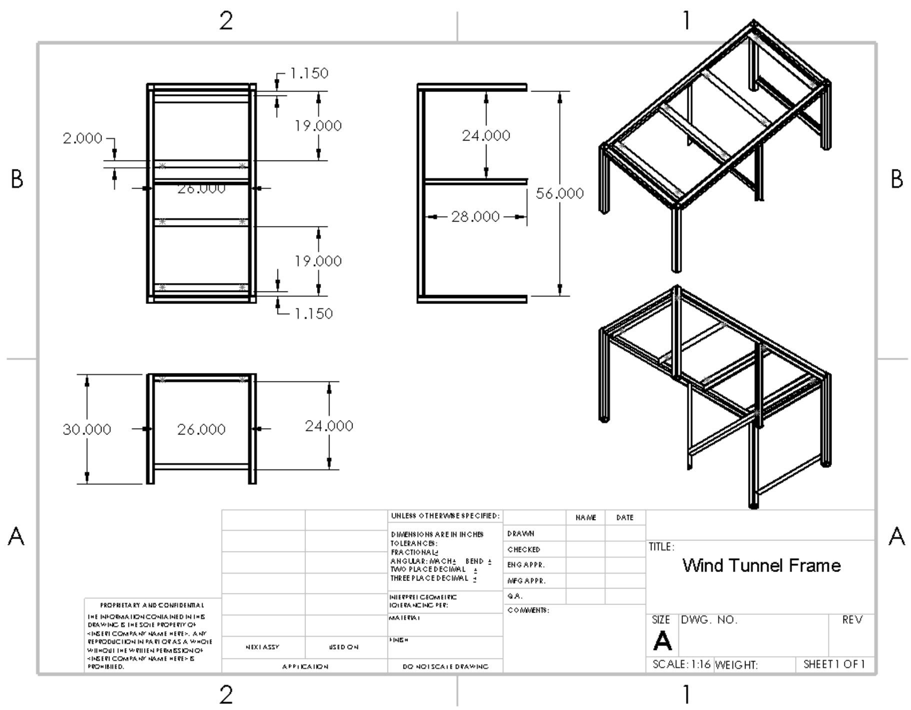

Figure A.3: Wind Tunnel Fame Assembly

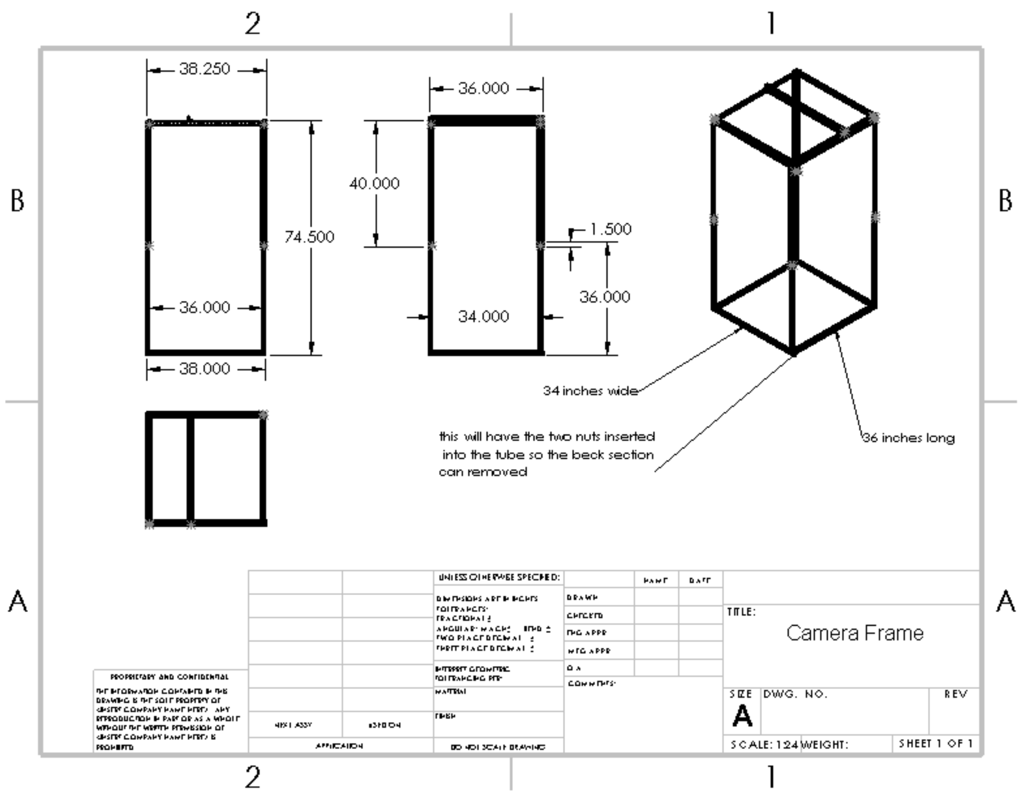

Figure A.4: Camera and Light Source Frame

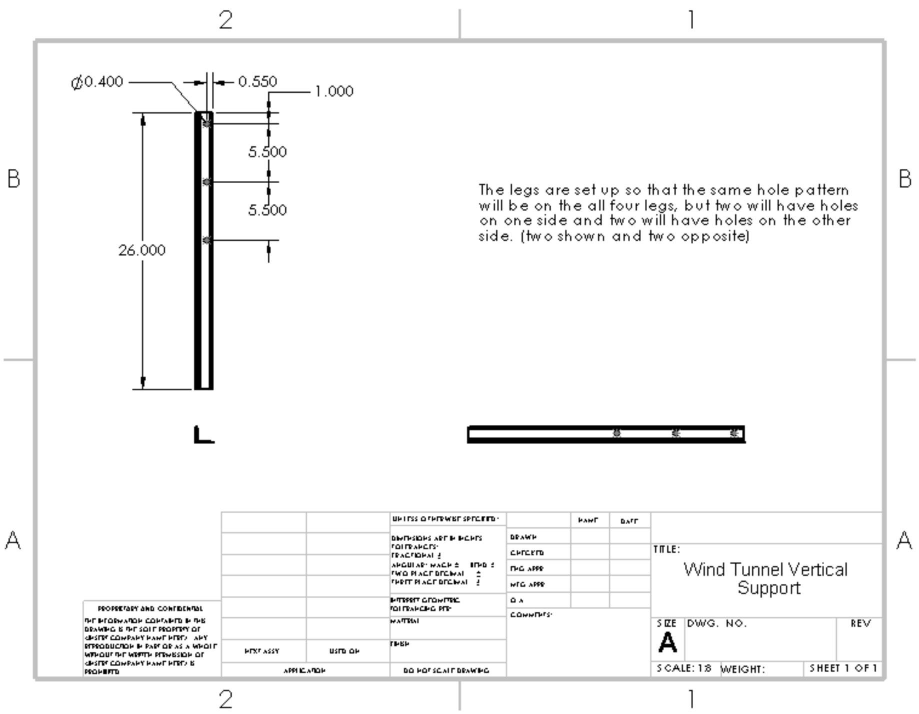

Figure A.5: Tunnel Support Legs

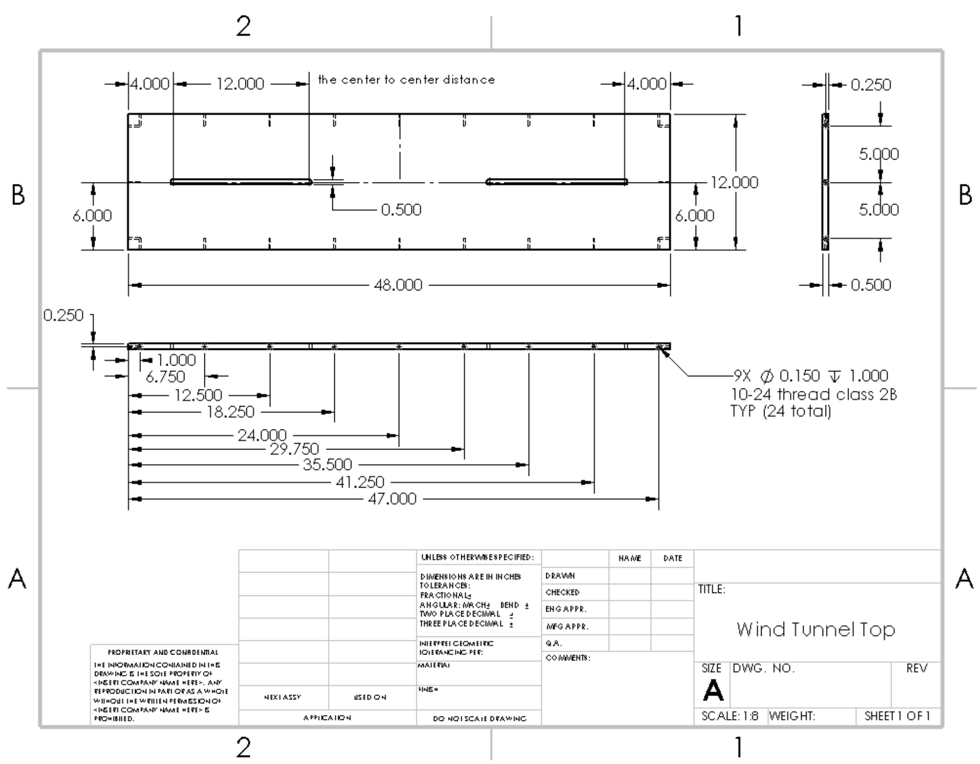

Figure A.6: Wind Tunnel Top

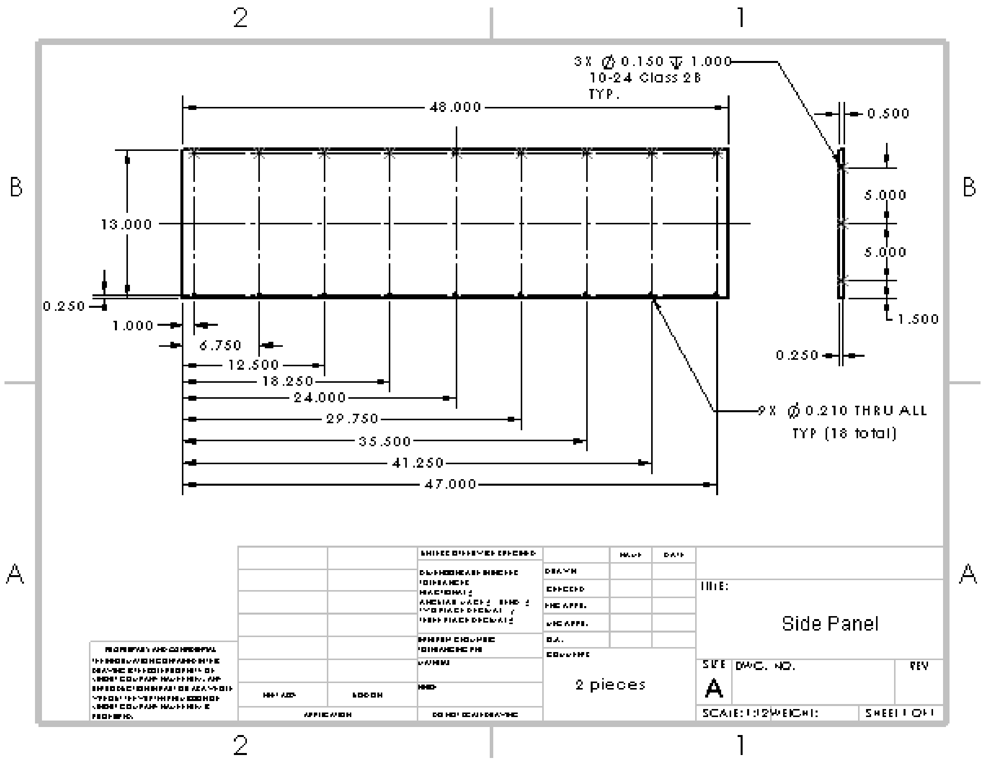

Figure A.7: Wind Tunnel Side Panels

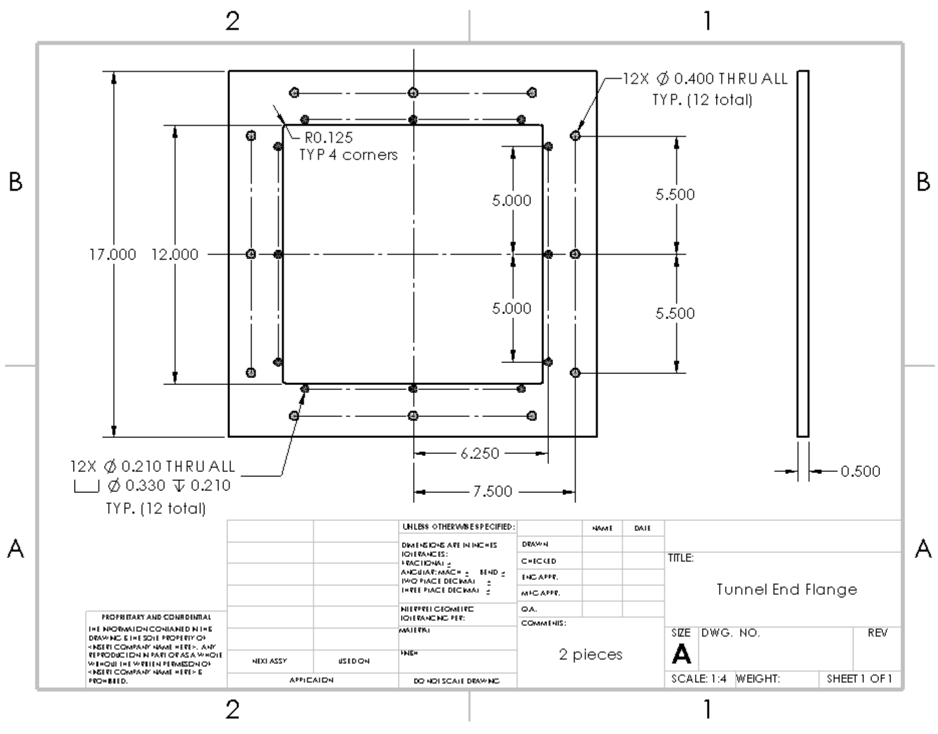

Figure A.8: The End Flange of the Wind Tunnel

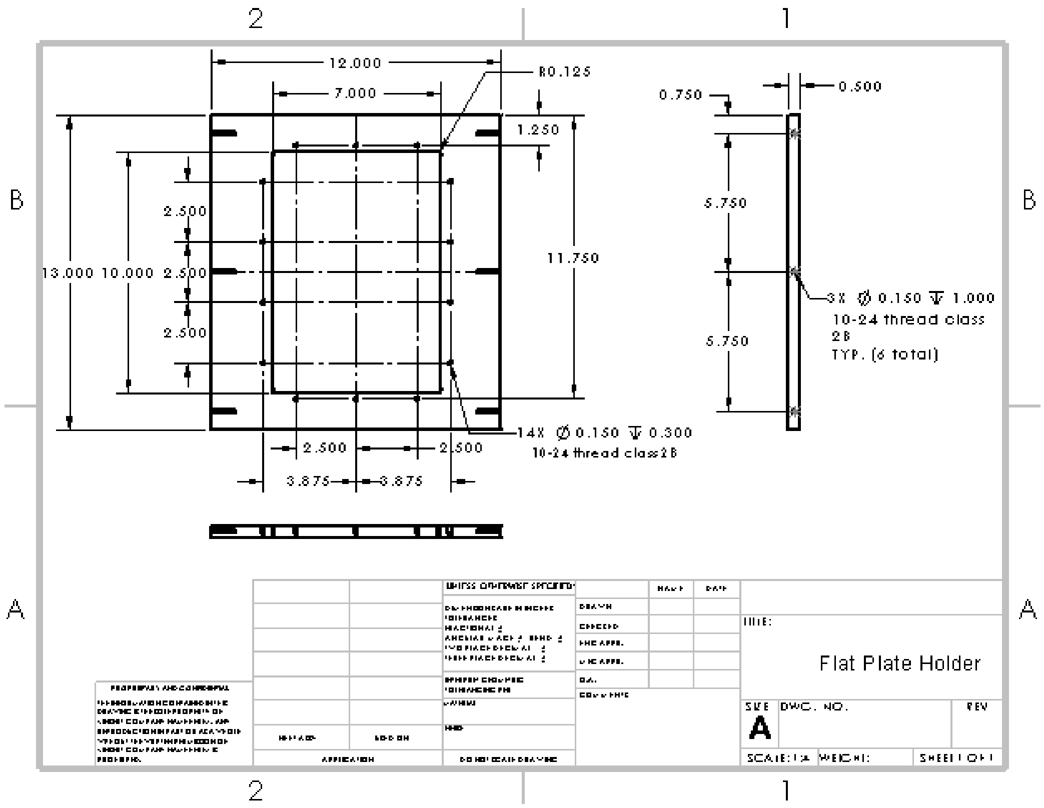

Figure A.9: The Center Bottom Insert Flat Plate Experiments

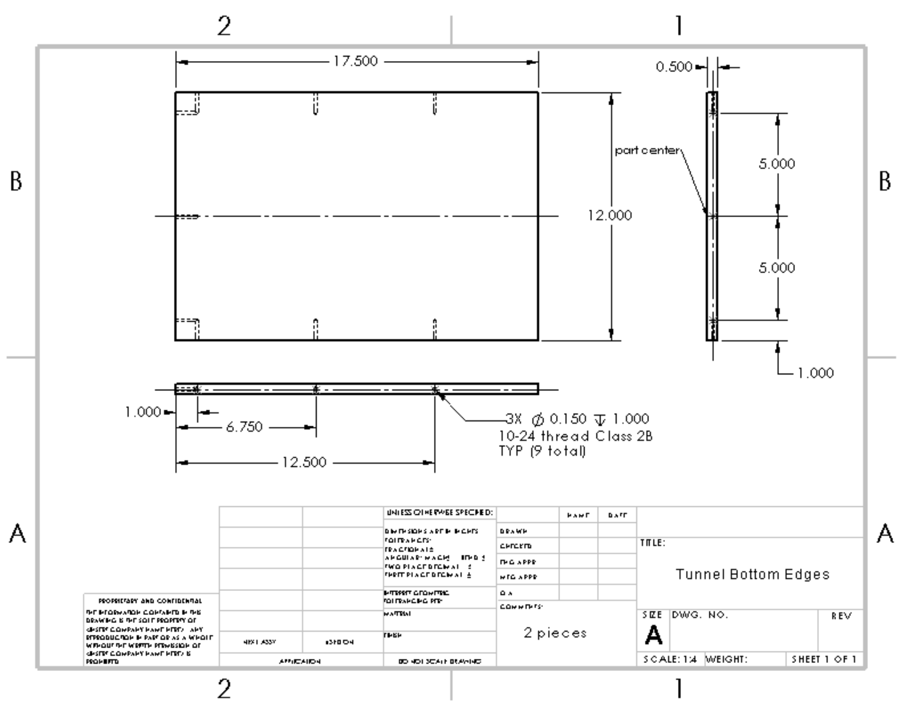

Figure A.10: Outer Panels of the Wind Tunnel Bottom

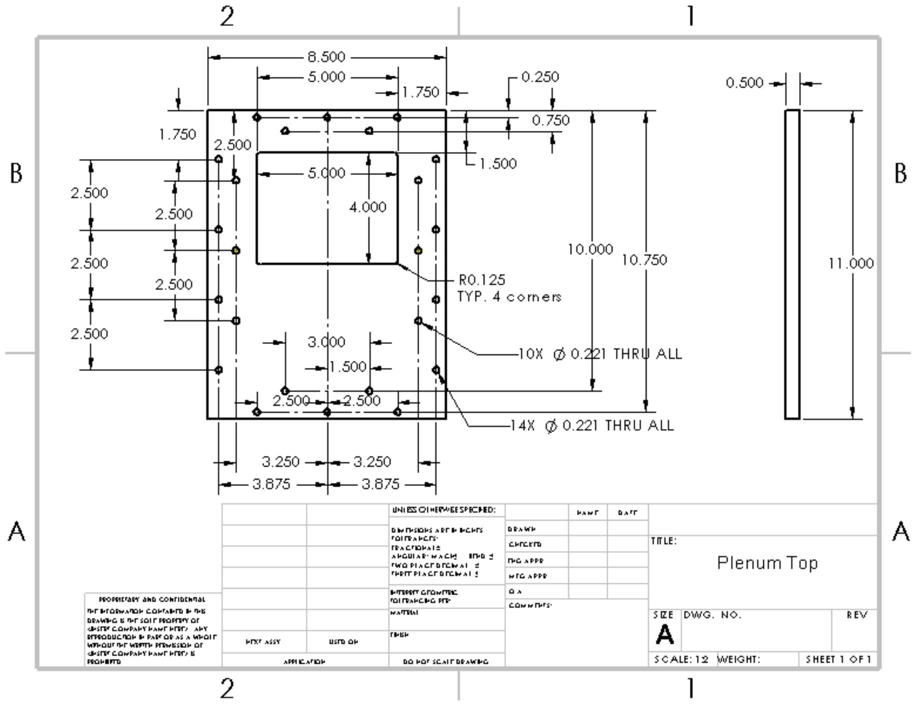

Figure A.11: Plenum Top Panel

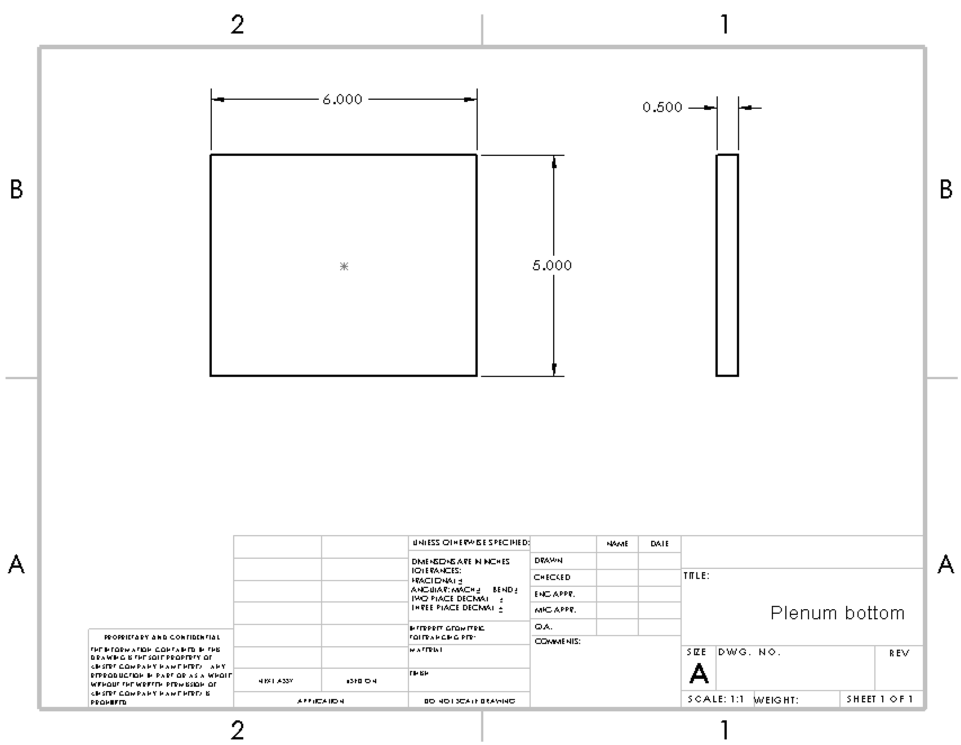

Figure A.12: Bottom Plenum Panel

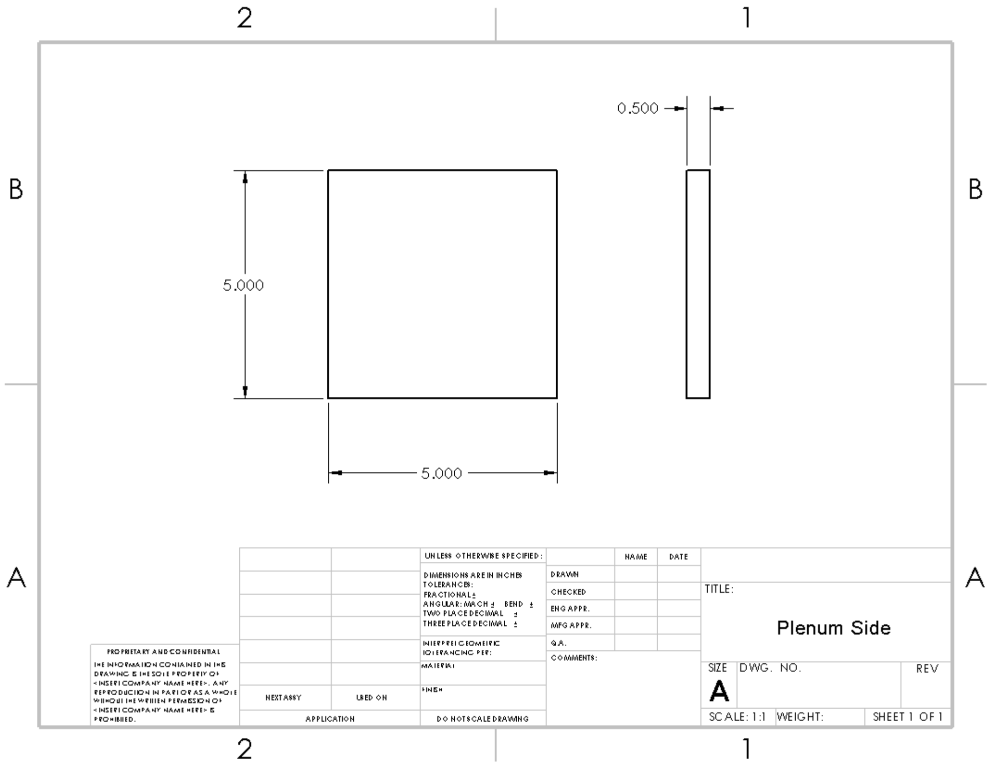

Figure A.13: Plenum Side Panels

APPENDIX B

The largest contributor to uncertainty in the PSP method is the CCD camera that is used to record the intensity of the fluorescence of the paint on the surface. The camera has random noise in its recoding as well as pixel to pixel variability within the camera. To start calculating the uncertainty it is necessary to start with the basic equations. Looking at cooling effectiveness first as a concentration ratio and then as partial pressure ratios over the surface in both the clean mainstream and in the film of the cooling flow.

$$\eta = \frac{\left(C_{1w} - C_m\right)}{C_2 - C_m} \tag{B.1}$$

$$\eta = \frac{\left(C_{1w} - C_m\right)}{C_2 - C_m} \tag{B.2}$$

$$\eta = \frac{\left(C_m - C_{1w}\right)}{C_m} \tag{B.3}$$

$$\eta = \frac{\left[\left(\frac{P}{P_{ref.air}}\right) - \left(\frac{P}{P_{ref.mix}}\right)\right]}{\left(\frac{P}{P_{ref.air}}\right)} \tag{B.4}$$

$$\left(\frac{P}{P_{ref.mix}}\right) = x\cdot\left[\frac{\left(I_{ref} - I_{black}\right)}{I_{mix} - I_{black}}\right]^3 + y\cdot\left[\frac{\left(I_{ref} - I_{black}\right)}{I_{mix} - I_{black}}\right]^2 + z\cdot\left[\frac{\left(I_{ref} - I_{black}\right)}{I_{mix} - I_{black}}\right] - w \tag{B.5}$$

After the basic equation is established, the equation to calculate the partial pressure of oxygen on the surface from the recorded light intensity must be used. There are two versions of this equation. Both use the intensity recorded of the reference and black images. The difference comes when looking at the intensity of the air images and mixed coolant images. Seen below these equations are substituted into the full effectiveness equation.

$$\eta = \frac{\left[x\cdot\left[\frac{(I_{ref}-I_{black})}{I_{air}-I_{black}}\right]^3 + y\cdot\left[\frac{(I_{ref}-I_{black})}{I_{air}-I_{black}}\right]^2 + z\cdot\left[\frac{(I_{ref}-I_{black})}{I_{air}-I_{black}}\right] - w\right] - \left[x\cdot\left[\frac{(I_{ref}-I_{black})}{I_{mix}-I_{black}}\right]^3 + y\cdot\left[\frac{(I_{ref}-I_{black})}{I_{mix}-I_{black}}\right]^2 + z\cdot\left[\frac{(I_{ref}-I_{black})}{I_{mix}-I_{black}}\right] - w\right]}{x\cdot\left[\frac{(I_{ref}-I_{black})}{I_{air}-I_{black}}\right]^3 + y\cdot\left[\frac{(I_{ref}-I_{black})}{I_{air}-I_{black}}\right]^2 + z\cdot\left[\frac{(I_{ref}-I_{black})}{I_{air}-I_{black}}\right] - w} \quad \text{(B.6)}$$

The Kline and McClintock method to find uncertainty has been used in this study. This method requires that the partial derivative of each variable within the governing equation. These partial derivatives of each of the four variables are seen below. The four deviatives are multiplied by the error in the recorded images to then be substituted into the square root equation.

$$\delta\eta_{\delta I\_black} := \frac{\frac{1.0234}{I_{N2}-I_{black}} - \frac{1.0234}{I_{air}-I_{black}} - \frac{1.0234\cdot I_{ref} + -1.0234\cdot I_{black}}{(I_{N2}-I_{black})^2} + \frac{1.0234\cdot I_{ref} + -1.0234\cdot I_{black}}{(I_{air}-I_{black})^2} - \frac{0.181\cdot(2\cdot I_{ref}-2\cdot I_{black})}{(I_{N2}-I_{black})^2} + \frac{0.181\cdot(2\cdot I_{ref}-2\cdot I_{black})}{(I_{air}-I_{black})^2} + \frac{0.362\cdot(I_{ref}-I_{black})^2}{(I_{N2}-I_{black})^3} - \frac{0.362\cdot(I_{ref}-I_{black})^2}{(I_{air}-I_{black})^3} - \frac{0.7944\cdot(I_{ref}-I_{black})^2}{(I_{N2}-I_{black})^3} + \frac{0.7944\cdot(I_{ref}-I_{black})^3}{(I_{N2}-I_{black})^4} + \frac{0.7944\cdot(I_{ref}-I_{black})^2}{(I_{air}-I_{black})^3} - \frac{0.7944\cdot(I_{ref}-I_{black})^3}{(I_{air}-I_{black})^4}}{\frac{1.0234\cdot I_{ref} + -1.0234\cdot I_{black}}{I_{air}-I_{black}} - \frac{0.181\cdot(I_{ref}-I_{black})^2}{(I_{air}-I_{black})^2} + \frac{0.2648\cdot(I_{ref}-I_{black})^3}{(I_{air}-I_{black})^3} - 0.1106} - \frac{\left[\frac{1.0234\cdot I_{ref} + -1.0234\cdot I_{black}}{I_{air}-I_{black}} - \frac{1.0234\cdot I_{ref} + -1.0234\cdot I_{black}}{I_{N2}-I_{black}} - \frac{0.2648\cdot(I_{ref}-I_{black})^3}{(I_{N2}-I_{black})^3} + \frac{0.2648\cdot(I_{ref}-I_{black})^3}{(I_{air}-I_{black})^3} + \frac{0.181\cdot(I_{ref}-I_{black})^2}{(I_{N2}-I_{black})^2} - \frac{0.181\cdot(I_{ref}-I_{black})^2}{(I_{air}-I_{black})^2}\right]\left[\frac{1.0234\cdot I_{ref} + -1.0234\cdot I_{black}}{(I_{air}-I_{black})^2} - \frac{1.0234}{I_{air}-I_{black}} + \frac{0.181\cdot(2\cdot I_{ref}-2\cdot I_{black})}{(I_{air}-I_{black})^2} - \frac{0.362\cdot(I_{ref}-I_{black})^2}{(I_{air}-I_{black})^3} - \frac{0.7944\cdot(I_{ref}-I_{black})^2}{(I_{air}-I_{black})^3} + \frac{0.7944\cdot(I_{ref}-I_{black})^3}{(I_{air}-I_{black})^4}\right]}{\left[\frac{1.0234\cdot I_{ref} + -1.0234\cdot I_{black}}{I_{air}-I_{black}} - \frac{0.181\cdot(I_{ref}-I_{black})^2}{(I_{air}-I_{black})^2} + \frac{0.2648\cdot(I_{ref}-I_{black})^3}{(I_{air}-I_{black})^3} - 0.1106\right]^2} = \begin{pmatrix} 1.437\times10^{-4} \\ 8.377\times10^{-5} \end{pmatrix}$$

$$\delta\eta_{\delta I\_ref} := \frac{\frac{1.0234}{I_{air}-I_{black}} - \frac{1.0234}{I_{N2}-I_{black}} + \frac{0.181\cdot(2\cdot I_{ref}-2\cdot I_{black})}{(I_{N2}-I_{black})^2} - \frac{0.181\cdot(2\cdot I_{ref}-2\cdot I_{black})}{(I_{air}-I_{black})^2} - \frac{0.7944\cdot(I_{ref}-I_{black})^2}{(I_{N2}-I_{black})^3} + \frac{0.7944\cdot(I_{ref}-I_{black})^2}{(I_{air}-I_{black})^3}}{\frac{1.0234\cdot I_{ref} + -1.0234\cdot I_{black}}{I_{air}-I_{black}} - \frac{0.181\cdot(I_{ref}-I_{black})^2}{(I_{air}-I_{black})^2} + \frac{0.2648\cdot(I_{ref}-I_{black})^3}{(I_{air}-I_{black})^3} - 0.1106} - \frac{\left[\frac{1.0234}{I_{air}-I_{black}} - \frac{0.181\cdot(2\cdot I_{ref}-2\cdot I_{black})}{(I_{air}-I_{black})^2} + \frac{0.7944\cdot(I_{ref}-I_{black})^2}{(I_{air}-I_{black})^3}\right]\left[\frac{1.0234\cdot I_{ref} + -1.0234\cdot I_{black}}{I_{air}-I_{black}} - \frac{1.0234\cdot I_{ref} + -1.0234\cdot I_{black}}{I_{N2}-I_{black}} - \frac{0.2648\cdot(I_{ref}-I_{black})^3}{(I_{N2}-I_{black})^3} + \frac{0.2648\cdot(I_{ref}-I_{black})^3}{(I_{air}-I_{black})^3} + \frac{0.181\cdot(I_{ref}-I_{black})^2}{(I_{N2}-I_{black})^2} - \frac{0.181\cdot(I_{ref}-I_{black})^2}{(I_{air}-I_{black})^2}\right]}{\left[\frac{1.0234\cdot I_{ref} + -1.0234\cdot I_{black}}{I_{air}-I_{black}} - \frac{0.181\cdot(I_{ref}-I_{black})^2}{(I_{air}-I_{black})^2} + \frac{0.2648\cdot(I_{ref}-I_{black})^3}{(I_{air}-I_{black})^3} - 0.1106\right]^2} = \begin{pmatrix} -1.231\times10^{-5} \\ 3.016\times10^{-5} \end{pmatrix}$$

$$\delta\eta_{\delta I\_air} := \frac{\frac{0.362\cdot(I_{ref}-I_{black})^2}{(I_{air}-I_{black})^3} - \frac{1.0234\cdot I_{ref} + -1.0234\cdot I_{black}}{(I_{air}-I_{black})^2} - \frac{0.7944\cdot(I_{ref}-I_{black})^3}{(I_{air}-I_{black})^4}}{\frac{1.0234\cdot I_{ref} + -1.0234\cdot I_{black}}{I_{air}-I_{black}} - \frac{0.181\cdot(I_{ref}-I_{black})^2}{(I_{air}-I_{black})^2} + \frac{0.2648\cdot(I_{ref}-I_{black})^3}{(I_{air}-I_{black})^3} - 0.1106} - \frac{\left[\frac{0.362\cdot(I_{ref}-I_{black})^2}{(I_{air}-I_{black})^3} - \frac{1.0234\cdot I_{ref} + -1.0234\cdot I_{black}}{(I_{air}-I_{black})^2} - \frac{0.7944\cdot(I_{ref}-I_{black})^3}{(I_{air}-I_{black})^4}\right]\left[\frac{1.0234\cdot I_{ref} + -1.0234\cdot I_{black}}{I_{air}-I_{black}} - \frac{1.0234\cdot I_{ref} + -1.0234\cdot I_{black}}{I_{N2}-I_{black}} - \frac{0.2648\cdot(I_{ref}-I_{black})^3}{(I_{N2}-I_{black})^3} + \frac{0.2648\cdot(I_{ref}-I_{black})^3}{(I_{air}-I_{black})^3} + \frac{0.181\cdot(I_{ref}-I_{black})^2}{(I_{N2}-I_{black})^2} - \frac{0.181\cdot(I_{ref}-I_{black})^2}{(I_{air}-I_{black})^2}\right]}{\left[\frac{1.0234\cdot I_{ref} + -1.0234\cdot I_{black}}{I_{air}-I_{black}} - \frac{0.181\cdot(I_{ref}-I_{black})^2}{(I_{air}-I_{black})^2} + \frac{0.2648\cdot(I_{ref}-I_{black})^3}{(I_{air}-I_{black})^3} - 0.1106\right]^2} = \begin{pmatrix} -2.264\times10^{-4} \\ -1.217\times10^{-3} \end{pmatrix}$$

$$\delta\eta_{\delta I\_N2} := \frac{\frac{1.0234\cdot I_{ref} + -1.0234\cdot I_{black}}{(I_{N2}-I_{black})^2} - \frac{0.362\cdot(I_{ref}-I_{black})^2}{(I_{N2}-I_{black})^3} + \frac{0.7944\cdot(I_{ref}-I_{black})^3}{(I_{N2}-I_{black})^4}}{\frac{1.0234\cdot I_{ref} + -1.0234\cdot I_{black}}{I_{air}-I_{black}} - \frac{0.181\cdot(I_{ref}-I_{black})^2}{(I_{air}-I_{black})^2} + \frac{0.2648\cdot(I_{ref}-I_{black})^3}{(I_{air}-I_{black})^3} - 0.1106} = \begin{pmatrix} 7.498\times10^{-5} \\ 1.103\times10^{-3} \end{pmatrix}$$

Figure B.1: The Partial Derivatives of Each of the Four Variables in the Effectiveness Equation

Two more sets of information are required to complete the calculation. A sample set of data is required to complete the uncertainty. For this experiment two have been provided, one with a low effectiveness and one with a high effectiveness. In addition to a sample data set, the error in each measurement must also be calculated. This is done with by multiplying the standard deviation of the oxygen pressure on the by each of the four variables in the equation. The error of the recorded images is calculated by finding the standard deviation of the intensity of the averaged air image.

$$error_{mix} := I_{mix} \cdot airpressure_{stddev} = \begin{pmatrix} 101.012 \\ 20.53 \end{pmatrix} \qquad error_{black} := I_{black} \cdot airpressure_{stddev} = \begin{pmatrix} 7.464 \\ 7.464 \end{pmatrix}$$

$$error_{air} := I_{air} \cdot airpressure_{stddev} = \begin{pmatrix} 17.879 \\ 19.834 \end{pmatrix} \qquad error_{ref} := I_{ref} \cdot airpressure_{stddev} = \begin{pmatrix} 17.954 \\ 19.947 \end{pmatrix}$$

$$uncertainty := \overrightarrow{\sqrt{(dI_{mix} \cdot error_{mix})^2 + (dI_{air} \cdot error_{air})^2 + (dI_{black} \cdot error_{black})^2 + (dI_{ref} \cdot error_{ref})^2}} = \begin{pmatrix} 7.428 \times 10^{-3} \\ 0.076 \end{pmatrix}$$

$$I_{black} := \begin{pmatrix} 397 \\ 397 \end{pmatrix} \quad I_{ref} := \begin{pmatrix} 955 \\ 1061 \end{pmatrix} \quad I_{air} := \begin{pmatrix} 951 \\ 1055 \end{pmatrix} \quad I_{mix} := \begin{pmatrix} 5373 \\ 1092 \end{pmatrix} \quad airpressure_{stddev} := 0.0188$$

The uncertainly can then be calculated with MATHCAD 15.0. The results show that high effectiveness values have lower levels of uncertainty. This is due to a greater difference in values between the air intensity images and the mixed flow intensity images. Finally using the effectiveness equation the actual cooling effectiveness can be determined.

$$\eta := \frac{\left[x \cdot \left(\frac{I_{ref} - I_{black}}{I_{air} - I_{black}}\right)^3 + y \cdot \left(\frac{I_{ref} - I_{black}}{I_{air} - I_{black}}\right)^2 + z \cdot \left(\frac{I_{ref} - I_{black}}{I_{air} - I_{black}}\right) - w\right] - \left[x \cdot \left(\frac{I_{ref} - I_{black}}{I_{mix} - I_{black}}\right)^3 + y \cdot \left(\frac{I_{ref} - I_{black}}{I_{mix} - I_{black}}\right)^2 + z \cdot \left(\frac{I_{ref} - I_{black}}{I_{mix} - I_{black}}\right) - w\right]}{\left[x \cdot \left(\frac{I_{ref} - I_{black}}{I_{air} - I_{black}}\right)^3 + y \cdot \left(\frac{I_{ref} - I_{black}}{I_{air} - I_{black}}\right)^2 + z \cdot \left(\frac{I_{ref} - I_{black}}{I_{air} - I_{black}}\right) - w\right]} = \begin{pmatrix} 0.849 \\ 0.074 \end{pmatrix}$$

APPENDIX C

Three different Matlab codes are used to post process the recorded data. The intensity code seen below, is used to determine the averaged intensity of each pixel for each of the four types of intensity images that taken.

```
% Gas Turbine Heat Transfer
% Department of Aerospace and Mechancial Engineering
% The University of Arizona
% Lesley Wright, Assistant Professor

%***********************************************************************
**
%*         PSP AND EXPERIMENTAL MEASUREMENT TECHNIQUES               *
%* PSP - Detailed Pressure and Film Cooling Effectiveness Distributions
*
%
%*                     Film Cooling Effectiveness Distributions
*
%***********************************************************************
**


% ************************ INTENSITY CALCULATION
************************
%        From recorded images calculate the intensity at every pixel




clear all     % clear all saved variables

clc           % clear command window

tic     % start internal timer


%
***********************************************************************
*
%
***********************************************************************
*
%
***********************************************************************
*
```

```
%
*********************************************************************
*


% ---------------         CHANGE INPUTS AS NEEDED       ---------------
---



% specify area over which to determine intensity
X0 = 1;    % x-coordinate of starting point
Y0 = 1;    % y-coordinate of starting point

W = 901;   % width of area
H = 1116;   % height of area


% Define pixels to re-define coordinates (from pixels to x/D and y/D)
% film cooling hole diameter (pixels)
D = 22;


% x (flow) direction offset
xx = 421;

% y (lateral) direction offset
yy = 48;


% specify the file name of the save images -- ex. n1_0001.tif
name = 'ref_';


% specify the file for the intensity output
ofile = 'ref.mat';     % open (create) specified data file



% specifiy the starting and ending number for the saved images
Start = 1;     % first image number
End = 250;     % last image number




% -----------------------         END INPUTS           --------------
----





% establish a matrix of zeros - size H x W
sum = zeros(H,W);
```

```
inten_matrix = zeros(H,W);


% begin loop to average intensity at each pixel over the given number
% images -- do the calculations from Start (first image)
% to End (last image)

for i = Start:End

    % show progress of program by alerting user after every 10 images
have
    % been completed
    if(~ mod(i,10))                 % if the count is divisible by 10,
        fprintf('%d\n',End-i)     % show the count in the command window
    end


    % create a character string with the image (counter, i) number,
    % preceeded by zeros
    num = sprintf('%04d',i);    % "0001" or "0150"

    % create a string of the entire image name
    % "name,num,.tif" -- "n1_0150.tif"
    ifile = strcat(name,num,'.tif');

    % read each image file and create a  data file (I) with the
    % intensity at each point (2D aray)
    I = imread(ifile, 'tif' );

    % add the coordinates of the selected area to the data
    I = I(Y0:Y0+H-1,X0:X0+W-1);
    inten = double(I);
    sum = sum + inten;

end


for ii = 1:W
    yD(ii) = (ii-xx)/D;
    for jj = 1:H

        xD(jj) = (jj-yy)/D;
        inten_matrix(jj, ii) = sum(jj,ii) / (End-Start+1);


    end
end




% in matrix format, save the x/d, y/d, and intensity variables
% these variables are saved in the XXX.mat file, and once loaded into
% MabLAB, the three variables are separately identified
```

```
save(ofile, 'xD', 'yD', 'inten_matrix');




% generate contour plot of intensity (with weighted pixel average)

figure
colormap([0 0 1;0 0 1;0 0.05263 1;0 0.1053 1;0 0.1579 1;0 0.2105 1;0
0.2632 1;0 0.3158 1;0 0.3684 1;0 0.4211 1;0 0.4737 1;0 0.5263 1;0
0.5789 1;0 0.6316 1;0 0.6842 1;0 0.7368 1;0 0.7895 1;0 0.8421 1;0
0.8947 1;0 0.9474 1;0 1 1;0.04545 1 0.9545;0.09091 1 0.9091;0.1364 1
0.8636;0.1818 1 0.8182;0.2273 1 0.7727;0.2727 1 0.7273;0.3182 1
0.6818;0.3636 1 0.6364;0.4091 1 0.5909;0.4545 1 0.5455;0.5 1 0.5;0.5455
1 0.4545;0.5909 1 0.4091;0.6364 1 0.3636;0.6818 1 0.3182;0.7273 1
0.2727;0.7727 1 0.2273;0.8182 1 0.1818;0.8636 1 0.1364;0.9091 1
0.09091;0.9545 1 0.04545;1 1 0;1 0.95 0;1 0.9 0;1 0.85 0;1 0.8 0;1 0.75
0;1 0.7 0;1 0.65 0;1 0.6 0;1 0.55 0;1 0.5 0;1 0.45 0;1 0.4 0;1 0.35 0;1
0.3 0;1 0.25 0;1 0.2 0;1 0.15 0;1 0.1 0;1 0.05 0;1 0 0;1 0 0]);
imagesc(yD, xD, inten_matrix)

colorbar
axis image
grid on

xlim([-15 15]);
ylim([-3 35]);

set(gca,'YTick',[-5 0 5 10 15 20 25 30 35])
set(gca,'XTick',[-15 -10 -5 0 5 10 15])

xlabel('Y / D','FontWeight','bold');
ylabel('X / D','FontWeight','bold');

fclose all;

toc     % stop internal timer
```

Once all the intensity files have been generated they are used by the Pressure Effective code to generate the detailed plots of cooling effectiveness.

```
% Gas Turbine Heat Transfer
% Department of Mechancial Engineering
% Baylor University
% Lesley Wright, Assistant Professor

%*********************************************************************
**
%*              PSP EXPERIMENTAL MEASUREMENT TECHNIQUE
*
%* PSP - Detailed Pressure and Film Cooling Effectiveness Distributions
*
%*
*
%*********************************************************************
**


% ****** STATIC PRESSURE AND FILM COOLING EFFECTIVENESS CALCULATION
******

%  From previously created intensity data files (Intensity.m) and input
%  calibration data, calculate the static pressure and film cooling
%  effectivness at each pixel.




%  STATIC PRESSURE
%        P/Pref = P/Pref = a3(Iref/I)^3 + a2(Iref/I)^2 + a1(Iref/I) +
a0

%  Pressure Ratio is calculated based on the user defined calibration.
%  Input Data Files:    black.dat
%                       ref.dat
%                       a1.dat, a2.dat, n1.dat, n2.dat, ar1.dat,
ar2.dat, etc.
%  Output Data Files:   a1pres.dat, etc.





%  FILM COOLING EFFECTIVENESS
%              eff = [(P/Pref)air - (P/Pref)n2] / (P/Pref)air
%  Film Cooling Effectiveness is calculated for two density ratios
based on
%  coolant flows of air & nitrogen (DR = 1) and air & argon (DR = 1.5)
%  Input Data Files:    a1pres.dat, a2pres.dat, n1pres.dat, n2pres.dat,
%                       ar1pres.dat, ar2pres.dat, etc
```

```
%  Output Data Files:   N2effect11.dat, N2effect12.dat,
%                       N2effect21.dat, N2effect22.dat,
%                       AReffect11.dat, AReffect12.dat,
%                       AReffect21.dat, AReffect22.dat,




clear all     % clear all saved variables
close all     % close all open windows
clc           % clear command window

tic     % start internal timer


%
***********************************************************************
*
%
***********************************************************************
*
%
***********************************************************************
*
%
***********************************************************************
*




% ---------------         CHANGE INPUTS AS NEEDED       ---------------
---


ofile = 'eff11.mat';     % open (create) specified data file
ofile2 = 'eff11_cl.mat';     % open (create) specified data file
ofile3 = 'eff11_latavg.mat';     % open (create) specified data file


% Define Size of Images
% These must match those used for black and reference
NX = 901;
NY = 1116;


% Input Coefficients from PSP Calibration
% P/Pref = a3(Iref/I)^3 + a2(Iref/I)^2 + a1(Iref/I) + a0
a_0 = -0.0354;
a_1 =  0.2137;
a_2 =  0.8986;
```

```
a_3 =  -0.1237;              % Travis Calibration


% Define Y boundaries for Lateral Average
% For example spanwise average: -1.0 < Y/D < 1.0

% Lower Limit of Average
low_yd = -2;

% Upper Limit of Average
high_yd = 4.8;



% Define Y boundaries for Overall Average
% For example spanwise average: -1.0 < Y/D < 1.0
%                               +2.0 < X/D < 14

% Lower Limit of Average
low_xd = 0.0;

% Upper Limit of Average
high_xd = 27.4;


% Load Intensity Data Files (Ib, Iref, test data: Ia1, Ia2, In1, In2)
blackdat = load('black.mat');      % Ib
xD =  blackdat.xD;
yD =  blackdat.yD;
blackint = blackdat.inten_matrix;

refdat = load('ref.mat');      % Iref
refint = refdat.inten_matrix;

airdat = load('A1.mat');      % Ia1
airint = airdat.inten_matrix;

mixdat = load('mix1.mat');      % In1
mixint = mixdat.inten_matrix;


H = size(blackint, 1);
W = size(blackint, 2);



Iratio_a1 = (refint - blackint)./ (airint - blackint);
Iratio_data = (refint - blackint)./ (mixint - blackint);
```

```
Pratio_a1 = a_3.*(Iratio_a1).^3 + a_2.*(Iratio_a1).^2 +
a_1.*(Iratio_a1) + a_0;
Pratio_data = a_3.*(Iratio_data).^3 + a_2.*(Iratio_data).^2 +
a_1.*(Iratio_data) + a_0;


eff = (Pratio_a1 - Pratio_data)./ Pratio_a1;


save(ofile, 'xD', 'yD', 'eff');



%----------------------------------------------------------------------
---
%----------------------------------------------------------------------
---
%----------------------------------------------------------------------
---
%----------------------------------------------------------------------
---
%----------------------------------------------------------------------
---
%----------------------------------------------------------------------
---


figure
colormap([1 0 0; 1 0 0; 1 0.0526 0; 1 0.1053 0; 1 0.1579 0; 1 0.2105 0;
1 0.2632 0; 1 0.3158 0; 1 0.3684 0; 1 0.4211 0; 1 0.4737 0; 1 0.5263 0;
1 0.5789 0; 1 0.6316 0; 1 0.6842 0; 1 0.7368 0; 1 0.7895 0; 1 0.8421 0;
1 0.8947 0; 1 0.9474 0; 1 1 0; 0.9545 1 0.0455; 0.9091 1 0.0909;
0.8636 1 0.1364;    0.8182 1 0.1818;    0.7727 1 0.2273; 0.7273 1
0.2727; 0.6818 1 0.3182;    0.6364 1 0.3636;    0.5909 1 0.4091;
0.5455 1 0.4545; 0.5000 1 0.5000; 0.4545 1 0.5455;    0.4091 1 0.5909;
0.3636 1 0.6364;    0.3182 1 0.6818;0.2727 1 0.7273; 0.2273 1 0.7727;
0.1818 1 0.8182;    0.1364 1 0.8636;    0.0909 1 0.9091;  0.0455 1
0.9545; 0 1 1;         0 0.95 1;         0 0.9 1;         0 0.85 1;0
0.8 1; 0 0.75 1;         0 0.7 1;         0 0.65 1;         0 0.6 1; 0
0.55 1; 0 0.5 1;         0 0.45 1;         0 0.4 1;         0 0.35 1;0
0.3 1; 0 0.25 1; 0 0.2 1; 0 0.15 1; 0 0.10 1; 0 0.05 1; 0 0 1; 0 0 1]);
imagesc(yD, xD, eff)

colorbar
caxis([0 .8])

axis image
grid on

xlim([-15 15]);
ylim([-3 35]);

set(gca,'YTick',[-5 0 5 10 15 20 25 30 35], 'FontWeight','bold')
set(gca,'XTick',[-15 -10 -5 0 5 10 15], 'FontWeight','bold')
```

```
xlabel('Y / D','FontWeight','bold', 'FontSize',12);
ylabel('X / D','FontWeight','bold', 'FontSize',12);



%-----------------------------------------------------------------------
---
%-----------------------------------------------------------------------
---
%-----------------------------------------------------------------------
---
%-----------------------------------------------------------------------
---
%-----------------------------------------------------------------------
---
%-----------------------------------------------------------------------
---

eff_rotate = rot90(eff);
eff_flip = fliplr(eff_rotate);
xD_rotate = rot90(xD,2);
yD_rotate = rot90(yD,2);

figure
colormap([0 0 0.560784339904785;0 0 0.623529434204102;0 0
0.686274528503418;0 0 0.749019622802734;0 0 0.811764717102051;0 0
0.874509811401367;0 0 0.937254905700684;0 0 1;0 0.062745101749897 1;0
0.125490203499794 1;0 0.18823529779911 1;0 0.250980406999588 1;0
0.313725501298904 1;0 0.376470595598221 1;0 0.439215689897537 1;0
0.498039215803146 1;0 0.560784339904785 1;0 0.623529434204102 1;0
0.686274528503418 1;0 0.749019622802734 1;0 0.811764717102051 1;0
0.874509811401367 1;0 0.937254905700684 1;0 1 1;0 1 0.874509811401367;0
1 0.749019622802734;0 1 0.623529434204102;0 1 0.501960813999176;0 1
0.376470595598221;0 1 0.250980406999588;0 1 0.125490203499794;0 1
0;0.125490203499794 1 0;0.250980406999588 1 0;0.376470595598221 1
0;0.501960813999176 1 0;0.623529434204102 1 0;0.749019622802734 1
0;0.874509811401367 1 0;1 1 0;1 0.937254905700684 0;1 0.874509811401367
0;1 0.811764717102051 0;1 0.749019622802734 0;1 0.686274528503418 0;1
0.623529434204102 0;1 0.560784339904785 0;1 0.501960813999176 0;1
0.439215689897537 0;1 0.376470595598221 0;1 0.313725501298904 0;1
0.250980406999588 0;1 0.18823529779911 0;1 0.125490203499794 0;1
0.062745101749897 0;1 0 0;0.937254905700684 0 0;0.874509811401367 0
0;0.811764717102051 0 0;0.752941191196442 0 0;0.690196096897125 0
0;0.627451002597809 0 0;0.564705908298492 0 0;0.501960813999176 0 0]);
imagesc(xD_rotate, yD_rotate, eff_flip)

colorbar;
caxis([0 1])

axis image
grid on

ylim([-15 15])
```

```
xlim([-3 35])

set(gca,'XTick',[-5 0 5 10 15 20 25 30 35], 'FontWeight','bold')
set(gca,'YTick',[-15 -10 -5 0 5 10 15],'FontWeight','bold')


xlabel('X / D','FontWeight','bold', 'FontSize',12);
ylabel('Y / D','FontWeight','bold', 'FontSize',12);


%-----------------------------------------------------------------------
---

figure
colormap([1 0 0; 1 0 0; 1 0.0526 0; 1 0.1053 0; 1 0.1579 0; 1 0.2105 0;
1 0.2632 0; 1 0.3158 0; 1 0.3684 0; 1 0.4211 0; 1 0.4737 0; 1 0.5263 0;
1 0.5789 0; 1 0.6316 0; 1 0.6842 0; 1 0.7368 0; 1 0.7895 0; 1 0.8421 0;
1 0.8947 0; 1 0.9474 0; 1 1 0; 0.9545 1 0.0455; 0.9091 1 0.0909;
0.8636 1 0.1364;    0.8182 1 0.1818;    0.7727 1 0.2273; 0.7273 1
0.2727; 0.6818 1 0.3182;    0.6364 1 0.3636;    0.5909 1 0.4091;
0.5455 1 0.4545; 0.5000 1 0.5000; 0.4545 1 0.5455;    0.4091 1 0.5909;
0.3636 1 0.6364;    0.3182 1 0.6818;0.2727 1 0.7273; 0.2273 1 0.7727;
0.1818 1 0.8182;    0.1364 1 0.8636;    0.0909 1 0.9091;  0.0455 1
0.9545; 0 1 1;         0 0.95 1;         0 0.9 1;         0 0.85 1;0
0.8 1; 0 0.75 1;         0 0.7 1;         0 0.65 1;         0 0.6 1; 0
0.55 1; 0 0.5 1;         0 0.45 1;         0 0.4 1;         0 0.35 1;0
0.3 1; 0 0.25 1; 0 0.2 1; 0 0.15 1; 0 0.10 1; 0 0.05 1; 0 0 1; 0 0 1]);
imagesc(xD_rotate, yD_rotate, eff_flip)

colorbar;
caxis([0 .8])

axis image
grid on

ylim([-2 6])
xlim([-3 35])

set(gca,'XTick',[-5 0 5 10 15 20 25 30 35], 'FontWeight','bold')
set(gca,'YTick',[0 2 4],'FontWeight','bold')


xlabel('X / D','FontWeight','bold', 'FontSize',12);
ylabel('Y / D','FontWeight','bold', 'FontSize',12);

%-----------------------------------------------------------------------
---

figure
imagesc(xD_rotate, yD_rotate, eff_flip)

colorbar;
caxis([0 1])
```

```
axis image
grid on

ylim([-2 2])
xlim([-1 16])

set(gca,'XTick',[-2 0 2 4 6 8 10 12 14 16], 'FontWeight','bold')
set(gca,'YTick',[-2 -1 0 1 2],'FontWeight','bold')


xlabel('X / D','FontWeight','bold', 'FontSize',12);
ylabel('Y / D','FontWeight','bold', 'FontSize',12);




%----------------------------------------------------------------------
---
%----------------------------------------------------------------------
---
%----------------------------------------------------------------------
---
%----------------------------------------------------------------------
---




figure
colormap([0 0 1;0 0 1;0 0.05263 1;0 0.1053 1;0 0.1579 1;0 0.2105 1;0
0.2632 1;0 0.3158 1;0 0.3684 1;0 0.4211 1;0 0.4737 1;0 0.5263 1;0
0.5789 1;0 0.6316 1;0 0.6842 1;0 0.7368 1;0 0.7895 1;0 0.8421 1;0
0.8947 1;0 0.9474 1;0 1 1;0.04545 1 0.9545;0.09091 1 0.9091;0.1364 1
0.8636;0.1818 1 0.8182;0.2273 1 0.7727;0.2727 1 0.7273;0.3182 1
0.6818;0.3636 1 0.6364;0.4091 1 0.5909;0.4545 1 0.5455;0.5 1 0.5;0.5455
1 0.4545;0.5909 1 0.4091;0.6364 1 0.3636;0.6818 1 0.3182;0.7273 1
0.2727;0.7727 1 0.2273;0.8182 1 0.1818;0.8636 1 0.1364;0.9091 1
0.09091;0.9545 1 0.04545;1 1 0;1 0.95 0;1 0.9 0;1 0.85 0;1 0.8 0;1 0.75
0;1 0.7 0;1 0.65 0;1 0.6 0;1 0.55 0;1 0.5 0;1 0.45 0;1 0.4 0;1 0.35 0;1
0.3 0;1 0.25 0;1 0.2 0;1 0.15 0;1 0.1 0;1 0.05 0;1 0 0;1 0 0]);
subplot(2,2,1)
imagesc(yD, xD, Pratio_a1)

colorbar
caxis([.25 1.25])
axis image
grid on


xlim([-15 15]);
```

```
ylim([-3 35]);

set(gca,'YTick',[-5 0 5 10 15 20 25 30 35], 'FontWeight','bold')
set(gca,'XTick',[-15 -10 -5 0 5 10 15], 'FontWeight','bold')

xlabel('Y / D','FontWeight','bold', 'FontSize',12);
ylabel('X / D','FontWeight','bold', 'FontSize',12);



subplot(2,2,2)
imagesc(yD, xD, Pratio_data)

colorbar
caxis([.25 1.25])
axis image
grid on


xlim([-15 15]);
ylim([-3 35]);

set(gca,'YTick',[-5 0 5 10 15 20 25 30 35], 'FontWeight','bold')
set(gca,'XTick',[-15 -10 -5 0 5 10 15], 'FontWeight','bold')

xlabel('Y / D','FontWeight','bold', 'FontSize',12);
ylabel('X / D','FontWeight','bold', 'FontSize',12);




%----------------------------------------------------------------------
---
%----------------------------------------------------------------------
---
%----------------------------------------------------------------------
---
%----------------------------------------------------------------------
---

%
% %extract centerline data
%

 CL_0_location = find(yD == 0);
 CL_5_location = find(abs(yD-5) < 0.02, 1);
 %CL_10_location = find(yD == 10);
 CL_n5_location = find(abs(yD+5) < 0.02, 1);
 %CL_n10_location = find(yD == -10);


CL_0 = eff(:,CL_0_location);
save(ofile2, 'xD', 'CL_0');
```

```
figure
subplot(2,2,1)
plot(xD, eff(:,CL_0_location), 'g', ...
    xD, eff(:,CL_5_location), 'r',...
    xD, eff(:,CL_n5_location), 'm',...
    'LineWidth',2)

legend show
legend('Y/D = 0','Y/D = +5', 'Y/D = -5')

set(gca,'YTick',[0 0.1 0.2 0.3 0.4 0.5 0.6 0.7 0.8 0.9], 'YMinorTick',
'on')
set(gca,'XTick',[0 5 10 15 20 25 30 35], 'XMinorTick', 'on')

xlim([0 40]);
ylim([0 0.9]);

grid on

xlabel('X / D','FontWeight','bold');
ylabel('h','FontWeight','bold','FontSize',14,'FontName','Symbol');

set(legend,'Location','NorthEast','FontWeight','bold',...
    'FontSize',8);




%-----------------------------------------------------------------------
---
%-----------------------------------------------------------------------
---
%-----------------------------------------------------------------------
---
%-----------------------------------------------------------------------
---

%
% %extract lateral average data
%


ylow_location = find(yD >= low_yd,  1);
yhigh_location = find(yD >= high_yd, 1);

xlow_location = find(xD >= low_xd,  1);
xhigh_location = find(xD >= high_xd, 1);

eff_lat_avg = eff(:,ylow_location:yhigh_location);
[lat_x, lat_y] = size(eff_lat_avg);
```

```
for jj = 1 : length(xD)
    sum(jj) =  0;

    for ii = ylow_location : yhigh_location
        sum(jj) = sum(jj) + eff(jj,ii);


    end
    lat_avg(jj) = sum(jj) / (yhigh_location - ylow_location + 1);  % 1
is added to
                                                               % ensure
the enpoints are
                                                               %
included in the division
end



save(ofile3, 'xD', 'lat_avg');

figure
subplot(2,2,1)
plot(xD, lat_avg, 'LineWidth',2)


set(gca,'YTick',[0 0.1 0.2 0.3 0.4 0.5 0.6 0.7 0.8 0.9], 'YMinorTick',
'on')
set(gca,'XTick',[0 5 10 15 20 25 30 35], 'XMinorTick', 'on')

xlim([0 40]);
ylim([0 0.6]);

grid on

xlabel('X / D','FontWeight','bold');
ylabel('h','FontWeight','bold','FontSize',14,'FontName','Symbol');


%-----------------------------------------------------------------------
---
%-----------------------------------------------------------------------
---
%-----------------------------------------------------------------------
---
%-----------------------------------------------------------------------
---

%
% overall average
%

eff_overall_avg =
eff(xlow_location:xhigh_location,ylow_location:yhigh_location);
stanford_overall_average = mean(mean(eff_overall_avg))
```

```
toc     % stop internal timer
```

The final step is to extract the data from the pressure effect files to create the XY line plots that are used to generate the laterally averaged effectiveness plots.

```
   close all;
clear all;
clc;


%M = 1.0;  %%  <<<<<<<<<<<<<<------------- CHANGE FOR EACH BLOWING
RATIO


data_cl = load('Dr=2\M=0.5\eff11_cl.mat');
eff_cl = data_cl.CL_0;

data_avg = load('Dr=2\M=0.5\eff11_latavg.mat');
eff_avg = data_avg.lat_avg;
xD = data_avg.xD;

%xMs = xD .* (4 * 15 / 16) / (1.0 * pi * 3 / 16);



fid_cl = fopen('DR_2p0_M0p5_cl_comp.dat', 'w');
fid_avg_xD = fopen('DR_2p0_M0p5_latavg_xD_comp.dat', 'w');
%fid_avg_xMS = fopen('ZPG_DR_4p0_M1p0_latavg_xMs.dat', 'w');


fprintf(fid_cl, 'zone \n');
fprintf(fid_avg_xD, 'zone \n');
%fprintf(fid_avg_xMS, 'zone \n');


for i = 1 : length(eff_cl)
    fprintf(fid_cl, '%6.4f  %6.4f   \n', xD(i), eff_cl(i));
end


for i = 1 : length(eff_avg)
    fprintf(fid_avg_xD, '%6.4f  %6.4f   \n', xD(i), eff_avg(i));
   % fprintf(fid_avg_xMS, '%6.4f  %6.4f   \n', xMs(i), eff_avg(i));
end

fclose all;
```

REFERENCES

[1] Adapted from https://www.cdaviationservices.com/apu/honeywell-tfe731, Accessed on August 4, 2017

[2] Adapted from http://sounak4u.weebly.com/gas-power-cycle.html, Accessed on October 9, 2016

[3] Adapted from https://www.geaviation.com/commercial/engines/ge9x-commercial-aircraft-engine, Accessed on October 9, 2016

[4] Bobzin, K., Bagcivian, N., Broelmann, T., Yildirim, B., 2013, "Influence of temperature on phase and thermal conductivity of single- and double-ceramic-layer EB-PVD TBC Top Coats consisting of 7YSZ, $Gd_2Zr_2O_7$ and $La_2Zr_2O_7$," *Surface and coatings Technology*, 237, pp. 56-64.

[5] Ohnabe, H., Masaki, S., Onozuka, M., Miyahara, K., and Sasa, T., 1999, "Potential application of ceramic matrix composites to aero-engine components," Elsevier, Composites Part A: pp. 489-496.

[6] Cherrared, D., 2017, "Numerical Simulation of Film Cooling a Turbine Blade Through a Row of Holes," *Journal of Thermal Engineering*, 3, pp. 1110-1120.

[7] Adapted from http://aerospaceengineeringblog.com/turbine-cooling/, Accessed on October 10, 2016

[8] Xu, L., Bo, S., Hongde, Y., and Lei, W., 2014, "Evolution of Rolls-Royce air-cooled turbine blades and feature analysis," *Asia-Pacific International Symposium on Aerospace Technology, APISAT2014*

[9] Adapted from http://www.virginia.edu/ms/research/wadley/high-temp.html, Accessed on October 10, 2016

[10] Han, J., 2002, "Recent Studies in Turbine Blade Cooling," *International Journal of Rotating Machinery,* 106, pp. 443-457.

[11] Goldstein, R., J., and Eckert, E.R.G., 1974, "Effects of Hole Geometry and Density on Three-Dimensional Film Cooling," *International Journal of Heat and Mass Transfer,* 17, pp. 595-607.

[12] Saravanamutto, H., Rogers, G., Cohen, H., 2001, "*Gas Turbine Theory*," 5th Edition, pp. 355-365.

[13] Oates, G. C., 1985, "*Aerothermodynamics of Aircraft Engine Components*," AIAA, New York, NY.

[14] Han, J., Dutta, S., and Ekkad, S., 2000, "Gas Turbine Heat Transfer and Cooling Technology," CRC Press, New York, NY.

[15] Bell, C. M., Hamakawa, H., and Ligrani, P. M., 2000, "Film Cooling From Shaped Holes," *Journal of Heat Transfer*, 122, pp. 224-232.

[16] Pedersen, D. R., Eckert, E.R.G., and Goldstein, R. J., 1977, "Film Cooling With Large Density Differences Between the Mainstream and the Secondary Fluid Measured by the Heat-Mass Transfer Analogy," *Journal of Heat Transfer*, 99, pp. 620-627

[17] Ammari, H., D., Hay, N., and Lampard, D., 1989, "The Effect of Ratio on the Heat Transfer Coefficient from a Film Cooled Flat Plate," Gas Turbine and Aeroengine Congress and Exposition, Toronto, Canada, pp. 1-8

[18] Johnson, B., Tian, W., Zhang, K., and Hu, H., 2014, "An Experimental Study of Density Ratio Effects on the Film Cooling Injection from Discrete Holes, Using PIV and PSP Techniques," *International Journal of Heat and Mass Transfer*, 76, pp. 337-349.

[19] Eberly, M. K. and Thole, K. A. 2014, "Time Resolved Film Cooling Flows at High and Low Density Ratios," *Journal of Turbomachinery*, 136, pp. 1-11.

[20] Sinha, A. K., Bogard, D. G., and Crawford, M. E., 1991, "Film Cooling Effectiveness Downstream of a Single Row of Holes With Variable Density Ratio," *Journal of Turbomachinery*, 113, pp. 442-449.

[21] Wright, L. M., McClain, S. T., and Clemenson, M. D., 2011, "Effect of Freestream Turbulence Intensity on film Cooling Jet Structure and Surface Effectiveness Using PIV and PSP," *Journal of Turbomachinery*, 133, pp. 1-12.

[22] Sarkar, S. and Babu, H. 2015, "Large Eddy Simulation on the Interactions of Make and Film Cooling Near a Leading Edge," *Journal of Turbomachinery*, 137, pp. 1-11.

[23] Bons, J. P., MacArther, C. D., and Rivir, R. B., 1989, "The Effect of High Free Stream Turbulence on film Cooling Effectiveness," *Journal of Turbomachinery*, 118, pp. 814-825.

[24] Saumweber, C., Schultz, A., and Wittig, S., 2003, "Free Stream Turbulence Effects on Film Cooling With Shaped Holes," *Journal of Turbomachinery*, 125, pp. 65-73.

[25] Mayhew, J. E., Baughn, J. W., and Byerley, A. R., 2003, "The Effect of Freestream Turbulence on Film Cooling Adiabatic Effectiveness," *International Journal of Heat and Fluid Flow*, 24, pp. 669-679.

[26] Wang, G., Ledezma, G., DeLancey, J., and Wang, A., 2017, "Experimental Study of Effusion Cooling With Pressure Sensitive Paint," *Journal of Engineering for Gas Turbine and Power*, 139, pp. 1-10.

[27] Teekaram, A. J. H., Forth, C. J. P., and Jones, T. V., 1991, "Film Cooling in the Presence of Mainstream Pressure Gradients," *Journal of Turbomachinery*, 113, pp. 484-492.

[28] Ekkad, S. V., Zapata, D., and Han, J. C., 1997, “Film Effectiveness Over a Flat Surface with Air and CO2 Injection Through Compound Angle Holes Using a Transient Liquid Crystal Image Method,” *Journal of Turbomachinery*, 119, pp. 587-593.

[29] Ligrani, P. M., Wigle, J. M., and Jackson, S. W., 1994, “Film Cooling From Holes with Compound Angle Orientations: Part 2 ERsults Downstream of a Single Row of Holes With 6d Spanwise Spacing,” *Journal of Heat Transfer*, 116, pp. 353-362.

[30] Schmidt, D. L., Sen, B., and Bogard, D. G., 1996, “Film Cooling with Compound Angle Holes: Adiabatic Effectiveness,” *Journal of Turbomachinery*, 118, pp. 807-813

[31] Sen, B., Schmidt, D. L., and Bogard, D. G., 1996, “Film Cooling With Compound Angle Holes: Heat Transfer,” *Journal of Turbomachinery*, 118, pp. 800-806.

[32] Thole, K. A., Gritsch, M., and Schulz, A., Wittig, S., 1997, “Effect of a Crossflow at the Entrance to a Film Cooling Hole,” *Journal of Fluids Engineering*, 119, pp. 533-540.

[33] Gritsch, M., Schulz, A., and Wittig, S., 1997, “Adiabatic Wall Effectiveness Measurements of Film Cooling Holes With Expanded Exits,” Presented at the International Gas Turbine & Aeroengine Congress & Exhibition, Orlando, Florida, pp. 1-10.

[34] Bell, C. M., Hamakawa, H., and Ligrani, P. M., 2000, “Film Cooling From Shaped Holes,” *Journal of Heat Transfer*, 122, pp. 224-232.

[35] Brittingham, R. A. and Leylek, J. H., 1997, “A Detailed Analysis of Film Cooling Physics Part IV: Compound Angle Injection With Shaped Holes,” Presented at the International Gas Turbine & Aeroengine Congress & Exhibition, Orlando, Florida, Pg. 1-14.

[36] Lee, H., Park, J. J., and Lee, J. S., 2001, “Flow Visualization and Film Cooling Effectiveness Measurements Around Shaped Holes with Compound Angle Orientations,” *International Journal of Heat and Mass Transfer*, 45, pp. 145-156.

[37] Ramesh, S., Ramirez, D. G., Ekkad, S. V., and Alvin, M. A., 2016, “Analysis of Film Cooling Performance of Advanced Tripod Hole Geometries With and Without Manufacturing Features,” *International Journal of Heat and Mass Transfer*, 94, pp. 9-19.

[38] Meier, S. M. and Gupta, D. K., 1994, “The Evolution of Thermal Barrier Coatings in Gas Turbine Engine Applications,” *Journal of Engineering for Gas Turbine and Power*, 116, pp. 250-257.

[39] Cao, X. Q., Vassen, R., and Stoever, D., 2003, “Ceramic Materials for Thermal Barrier Coatings,” *Journal of the European Ceramic Society*, 24, pp. 1-10.

[40] Sikarwar, B. S., Khandekar, S., Agrawal, S., Kumar, S., and Muralidhar, K., 2013, "Dropwise Condensation Studies on Multiple Scales," *Heat Transfer Engineering*, 33, pp. 301-341.

[41] Critoph, R. E., Holland, M. K., and Fisher, M., 1999, "Comparison of Steady State and Transient Methods for Measurement of Local Heat Transfer in Plate Fin-tube Heat Exchangers Using Liquid Crystal Thermography With Radiant Heating," *International Journal of Heat and Mass Transfer*, 42, pp. 1-12.

[42] Baughn, J. W., Ireland, P. T., and Jones, T. V., 1988, "A Comparison of the Transient and Heat Coated Methods for the Measurement of Local Heat Transfer Coefficients on a Pin Fin," The American Society of Mechanical Engineers, New York, NY, 88-GT-180

[43] Kunze, M., Vogeler, K., Brown, G., Prakash, C., and Landis, K., 2011, "Aerodynamic and Endwall Film-Cooling Investigations of a Gas Turbine Nozzle Guide Vane Appling Temperature-Sensitive Paint," *Journal of Turbomachinery*, 133, pp. 1-9.

[44] Lorenz, M., Horbach, T., Schulz, A., and Bauer, H.-J., 2013, "A Novel Measuring Technique Utilizing Temperature Sensitive Paint – Measurement, Procedure, Validation, Application, and Comparison with Infrared Thermography," *Journal of Turbomachinery*, 135, pp. 1-10.

[45] Fey, U., Engler, R. H., Egami, Y., Iijima, Y., Asai, K., Jansen, U., and Quest, J., 2003, "Transition Detection by Temperature Sensitive Paint at Cryogenic Temperatures in the European Transonic Wind Tunnel (ETW)," Instrumentation in Aerospace Simulation Facilities, Gottingen, Germany

[46] Schulz, A., 2000, "Infrared Thermography as Applied to Film Cooling of Gas Turbine Components," *Measurement Science and Technology*, 11, pp. 948-956.

[47] Pedersen, D. R., Eckert, E. R. G., and Goldstein, R. J., 1977, "Film Cooling With Large Density Differences Between the Mainstream and the Secondary Fluid Measured by the Heat Mass Transfer Analogy," *Journal of Heat Transfer*, 99, pp. 620-627.

[48] Ito, S., GoldStein, R. J., and Eckert, E. R. G., 1978, "Film Cooling of a Gas Turbine Blade," *Journal of Engineering for Power*, 100, pp. 476-481.

[49] Friedrichs, S., Hodson, H. P., and Dawes, W. N., 1995, "Distribution of Film-Cooling Effectiveness on a Turbine Endwall Measured Using the Ammonia and Diazo Technique," *Journal of Turbomachinery*, 118, pp. 613-621.

[50] Goldstein, R. J. and Stone, L. D., 1997, "Row of Holes Film Cooling of Curved Walls at Low Injection Angles," *Journal of Turbomachinery*, 119, pp. 574-579.

[51] Adapted from https://www.nasa.gov/aero/power-of-pink-provides-nasa-with-pressure-pictures, Accessed on March 9, 2017

[52] Morris, M. J., Donovan, J. F., Kegelman, J. T., Schwab, S. D., Levy, R. L., and Crites, R. C., 1993 " Aerodynamic applications of pressure sensitive paint", *AIAA Journal*, 31, pp. 419-425.

[53] Adapted from http://www.psp-tsp.com/index.php?id=115, Accessed on February 27, 2017

[54] Adapted from http://www.aerospaceweb.org/design/psp/characteristics.shtml, Accessed on March 15, 2017

[55] Caciolli, G., Facchini, B., Picchi, A., and Tarchi, L., 2013, "Comparison Between PSP and TLC Steady State Techniques for Adiabatic Effectiveness Measurement on a Multi-perforated Plate," *Experimental Thermal and Fluid Science*, 48, pp. 122-133.

[56] Navarra, K. R., 1997, "*Development of the Pressure Sensitive Paint (PSP) Technique for Advanced Turbomachinery Applications*," M.S. Thesis, Propulsion Directorate, Wright-Paterson Air Force Base

[57] Wright, L. M., Gao, Z., Varvel, T. A., and Han, J., 2005, "Assessment of Steady State PSP, TSP, and IR Measurement Techniques for Flat Plate Film Cooling," Heat Transfer Conference, San Francisco, California, USA, July 17-22

[58] Gao, Z., and Han, J., 2009, "Influence of Film Hole Shape and Angle on Showerhead Film Cooling Using PSP Technique," *Journal of Heat Transfer*, 131, pp. 1-10

[59] Suryanarayanan, A., Ozturk, B., Schobeiri, M. T., and Han, J. C., 2010, "Film Cooling Effectiveness on a Rotating Turbine Platform Using Pressure Sensitive Paint Technique," *Journal of Turbomachinery*, 132, pp. 1-13

[60] Taslim, M. E., Spring, S. D., and Mehlman, B. P., 1992, "Experimental Investigation of film cooling Effectiveness for Slot of Various Exit Geometries," *Journal of Thermophysics and Heat Transfer*, 6, pp. 302-307.

[61] Mendoza, D. R., 1997, "An Analysis of CCD Camera Noise and It's Effect on Pressure Sensitive Paint Instrument System Signal-To-Noise Ratio," Instrumentation in Aerospace Simulation Facilities, Institution of Electrical and Electronics Engineering, Pacific Grove, California, pp. 22-29

[62] Natsui, G., Little, Z., Kapat, J. S., Dees, J. E., and Laskowski, G., 2016, "A detailed Uncertainty Analysis of Adiabatic Film Cooling Effectiveness Measurements Using Pressure Sensitive Paint," *Journal of Turbomachinery*, 138, pp. 1-12.

[63] Liu, T., 2001, "Accuracy of Pressure Sensitive Paint," *American Institute of Aeronautics and Astronautics*, 39, pp. 1-42.

[64] Kline, S. J. and McClintock, F. A., 1953, "Describing Uncertainties in Single Sample Experiments," *Mechanical Engineering*, 75, pp. 3-8.

[65] Vinton, K., 2016, "*Experimental Investigation of Full Coverage Combustor Film Cooling and Airfoil film Cooling for Advanced Gas turbine Engines*," M.S. thesis, Department of Mechanical Engineering, Baylor University